Methods for Generation and Detection of Vorticity in Atomic Bose-Einstein Condensates

by

Samuel L. Nerenberg

A Dissertation Submitted to the Faculty of the

James C. Wyant College of Optical Sciences

In Partial Fulfillment of the Requirements
For the Degree of

Doctor of Philosophy

In the Graduate College

The University of Arizona

2 0 2 0

THE UNIVERSITY OF ARIZONA
GRADUATE COLLEGE

As members of the Dissertation Committee, we certify that we have read the dissertation prepared by **Samuel L. Nerenberg**, titled **Methods for Generation and Detection of Vorticity in Atomic Bose-Einstein Condensates** and recommend that it be accepted as fulfilling the dissertation requirement for the Degree of Doctor of Philosophy.

Professor Brian P. Anderson, Chair Date: 4/13/2020

Professor Ewan M. Wright Date: 4/13/2020

Professor Ronald J. Jones Date: 4/15/2020

Final approval and acceptance of this dissertation is contingent upon the candidate's submission of the final copies of the dissertation to the Graduate College.

I hereby certify that I have read this dissertation prepared under my direction and recommend that it be accepted as fulfilling the dissertation requirement.

Professor Brian P. Anderson Date: 5/8/2020
Dissertation Committee Chair
Wyant College of Optical Sciences

Acknowledgments

It is, of course, impossible to thank everyone who has supported me and taught me and helped bring me to this point. There are so many worthy of thanks and only a few paragraphs in which to thank them. I will try to be brief so if, perchance, you find yourself missing from this woefully inadequate list and feel slighted please know that you are in good company.

First and foremost I must thank my family. My mother and father who home-schooled me, sought out so many unique opportunities for me to learn, allowed me to indulge my various interests and surrounded me with an interesting and diverse group of people who surely shaped me from a young age. My older brother, Max who gave me something to aspire to as well as compete with and who, to this day is a great friend and my favorite adventure-partner. My step-father Russ who has always shared his enthusiasm for knowledge and research as well as a healthy dose of fun. And my partner, Michaela who is my best friend and remains an unwavering support through thick and thin while we chase our goals together.

I would also like to thank my advisor, Professor Brian Anderson. Without Brian's encouragement and support I would have never even considered attempting a PhD. Brian has been the best kind of mentor: one who provides proper guidance while allowing me room to learn from my own mistakes and follow my own interests. I would also like to thank the rest of my committee, Professors Ewan Wright and Jason Jones. I first encountered Ewan as an undergraduate where he taught my sophomore course in Physical Optics. Since then he has always made time for me whenever I have burst unannounced and un-appointment-ed into his office with some burning question or idea. What's more, I don't think he's ever failed to give me an insightful answer. Jason taught the first quantum class I ever took and was an inspiring and effective teacher. Without his clear exposition I doubt I would have become so fascinated by quantum and decided to pursue more of the classes which eventually led me here. In addition, Jason gave me my first research opportunity in graduate school where I learned many of my foundational laboratory skills.

Experimental physics is not a solitary activity and my group mates and colleagues have been some of my most important teachers and collaborators. I want to thank Andrew Schaffer who has run BEC Lab II concurrently with me running Lab I. Andrew has been a great friend during the duration of my PhD. He has been emotional as well as technical support and I owe him a great deal. I'd also like to thank the grad students in my group who came before me: Kali Wilson, Zach Newman, Joe Lowney and Jessica Meyers for all their wisdom and help. I'm also looking forward to watching the career of our undergraduate assistant, Van Butcher who is extremely capable and a lot of fun to have in the lab. In addition, the students in Poul Jessen's group who share the hallway with us have been great help and fantastic company.

I'll miss our semi-regular (possibly too regular from our advisors' perspectives) coffee gatherings. Their diverse interests, wit and taste in fine cheese helped the whole seven years to fly by. So thanks to David Melchior, Nathan Lysne and Dan Hemmer.

I have been lucky to find an amazing network of people during my time in Tucson. One person who continually helped and inspired me to branch out, try new things and meet new people was my (technically former but actually forever) roommate, Lena Wolfe. From introducing me to some of my best friends to teaching me some of my best dance moves it makes me happy to call her one of my closest friends. I want to give a big acknowledgement to Michał Łukowski who was one of my first undergraduate TAs and, over the course of 11 years in the department, became one of my closest friends. His excellent taste in beautifully weird music, film and art, not to mention his genuine warmth and bottomless sass have made him great company during my time in this desert. Cameron Solem and Jason Xu, thanks for taking the wheel during one of the best road trips to ever happen. Thank you Dave DiDonato aka "Hookah Dave" for innumerable great times and great conversations. You're a born engineer and I'm so excited to see how you apply your creativity in the future. I want to thank my very good friends and former roommates, Patrick Wood and Rafael Rojas. We've been through a lot together and I think of you guys as family. You're both brilliant and endless fun and I can't wait to meet up year after year for the rest of our lives and blast Judas Priest and laugh like the complete idiots we really are. I want to thank Dan Glinski whose commitment to rationality and critical thought are an inspiration to me. Dan is one of the best people I know, I'm constantly learning from him and I owe him the deepest of debts for convincing me to start playing music again and bringing me into the world of jazz. I want to thank my childhood friends from New York: Nick Tario, Weston Raab, Eric Rosenberg, Evan Moore, Dan Romanelli, Charles Miller, Renee Bean, Kyle Kleege and Jeff Snyder to name just a few. The impact you have all had on me is immeasurable. Zach Watson I thank as both a friend and collaborator. Without his help with peak detection algorithms and his expertise in Shack-Hartmann wavefront sensors I never would have been able to take my ideas this far. Zach is both a generous friend and a formidably talented scientist.

Finally, I would like to thank the esteemed couple, Dr. Robert Harris and Diane DeBlois. Rob and Diane have fundamentally shaped my idea of what it means to be a scholar as well as a member of a community. Rob took an interest in the education of my brother and I as homeschoolers. He introduced us to physics with weekly sessions we called "Time Lab." His lessons and discourses captured my imagination and he led us through our first experiment which happened to be observations of two-dimensional turbulence in a fast-moving soap film. Now, almost two decades later, because of the encouragement, generosity and mentoring of people like Rob I am able to call myself a physicist.

Dedication

To the numerous people in my life who have encouraged me and taught me the value of curiosity.

Table of Contents

Table of Contents—*Continued*

List of Figures

List of Figures—*Continued*

List of Figures—*Continued*

LIST OF FIGURES—*Continued*

List of Figures—*Continued*

List of Figures—*Continued*

List of Figures—*Continued*

Abstract

Dilute gas Bose-Einstein condensates (BECs) provide unique and powerful experimental platforms to study fluid turbulence. Some aspects of BEC hydrodynamics are specific to atomic quantum fluids such as quantized vortices and flexible trapping geometries. However, there are features of turbulence that are universal and simpler to understand in such systems. BECs are also of interest in fundamental physics in their own right and a rich synthesis of theory and experiment has yielded powerful numerical methods to simulate and study BEC dynamics. In this dissertation I present two experiments, one conducted and one proposed, describing novel aspects of the generation and detection of vorticity in Bose-Einstein condensates.

Models of BEC dynamics at zero temperature are provided by the Gross-Pitaevskii equation. Simple and fast numerical solutions of this equation have yielded a wealth of literature. However, in experimental reality the atomic ensemble exists at a finite temperature and consists of a BEC coexisting with a thermal cloud of non-condensed atoms. The interaction between the condensate and the thermal fraction yields rich and complex physics that require more advanced models. We present an experiment demonstrating the relaxation dynamics of a BEC in a rotating trap perturbed by a repulsive laser barrier. The data provided by this experiment are valuable to further development of theoretical models that incorporate interactions between the BEC and noncondensed atoms.

In the field of quantum fluid dynamics, an experimental method to determine the position and circulation of vortices is a highly sought-after capability. Onsager's point-vortex model of turbulence completely determines the kinetic energy spectrum of an incompressible fluid by these degrees of freedom. We present proof-of-principle simulations that describe a new method of spatially sampling the velocity field of a two-dimensional BEC by using an optical lattice analogously to a Shack-Hartmann

Wavefront Sensor. Extracting vortex information from the appropriately sampled velocity field can be accomplished either qualitatively or with detection algorithms. This method requires minimal experimental infrastructure and is generally applicable across atomic species. The implications of measuring a condensate velocity field are broad and these initial results provide the first step towards realizing a valuable tool in BEC physics.

CHAPTER 1

Introduction

Since the Bose-Einstein condensate (BEC) was first conceived in 1924 by its eponymous theorists [1, 2] and first realized in an atomic gas by the group of Cornell and Wieman [3] in 1995 it has shown immense promise as a tool to investigate a broad range of physical phenomena. The primary property of a BEC that this dissertation is concerned with is superfluidity. Superfluidity, first reported in 1938 by Allen, Misener and Kapitza [4,5] in liquid helium occurs when the fluid is cooled below a critical temperature T_C and undergoes a phase transition characterized by a precipitous drop in viscosity and the onset of other properties not seen in classical fluids. One of these properties is the quantization of circulation of the superfluid. Any circulation in the superfluid must be due to the presence quantum vortices (in increments of h/m where h is Planck's constant and m is the particle mass) as first postulated by Onsager in 1949 [6]. In the same paper, Onsager developed a statistical mechanical theory by which a turbulent flow in a bounded 2D incompressible fluid is characterized by the locations and circulations of point vortices. Quantum vortices, which are realizations of Onsager's point vortex model, are concentrated regions of fluid circulation about a phase singularity; in a condensate they manifest as zero points of the condensate density. Studying large, disordered distributions of these vortices is the basis of the field of quantum turbulence and as such there has been much work put into the generation and detection of these states [7–22]. Turbulence is characterized by a cascade of energy across a spectrum of length scales from the scale at which kinetic energy is injected to the scale at which it is dissipated. The energy spectrum of a turbulent flow displays various power-law behaviors in different regimes [23]. These statistical signatures of turbulence are universal across platforms. The accessible nature

of quantum vortices coupled with the accurate numerical simulations provided by the Gross-Pitaevski equation [24] make BECs a powerful medium in which to study turbulent fluid motion and its relation to statistical measures such as energy spectra. Experimental measurements of a power-law energy spectrum in BEC quantum turbulence have never been realized and remain a major open problem in quantum turbulence. The problem comes down to obtaining the velocity field of a BEC. Previous experimental methods have been difficult to implement as they have requirements like complex timing and control sequences, stable phase references or are specific to atomic species.

A related problem has been solved in astronomical optics through the advent of adaptive optics and the Shack-Hartmann Wavefront Sensor (SHWS) to reconstruct the phase profile of linear optical fields [25, 26]. The SHWS is comprised of a grid of lenslets of identical focal length that sample the wavefront at discrete points. When the wavefront has non-zero slope the focused spot is displaced from the optical axis of the lenslet by a distance proportional to the wavefront slope. By measuring the spot displacements the gradient of the phase of the optical field is determined locally and thus the phase profile of the full wavefront may be approximated. Adapting the experimental techniques and processing algorithms of this field to atom-optical physics may yield powerful and easily implementable tools of investigation for BEC experiments.

The study of BEC dynamics faces many experimental hurdles. Due to their delicate nature, condensates are rapidly degraded by most imaging techniques via heating and other atom loss mechanisms. As a result, the large majority of data regarding the hydrodynamics of BECs is a statistical aggregation of many experimental runs. This information is valuable and, at times, sufficient for cases where the condensate is in equilibrium or where repeatability is not an issue. However, studies of non-equilibrium cases such as turbulence are seriously hampered because dynamics are extremely sensitive to initial conditions. Some “holy grail” measurements for BEC

turbulence which are still being developed are

- Many-frame stroboscopic imaging of vortex distributions or "making movies;"
- Simultaneously determining the charge and location of vortices in a two-dimensional BEC;
- Measuring the kinetic energy spectrum of a BEC, which can be obtained from a phase reconstruction or a velocity field measurement.

Work towards making movies of BEC vortex distributions has been put forth by Wilson et al. [9,10] and the dissertation of Zach Newman [27] details the construction of a BEC device that is suited to this end. Since the Onsager point vortex model completely characterizes the spatial distribution of an incompressible fluid's kinetic energy according to the charge and location of vortices, the measurement of these degrees of freedom is important to the study of superfluid hydrodynamics. Such measurements have been made in three dimensional condensates via matter-wave interference by several groups [20–22] and Seo et al. have used spatially resolved Bragg scattering [19]. However, these measurements do not provide the full velocity field and are specific to atomic species. The measurement of a kinetic energy spectrum in a Bose-Einstein condensate is generally difficult, or inaccessible to normal methods due to the nonlinearity of the condensate. Such a measurement would provide deep insight into the processes of energy transport in fluids. The three measurements listed above are open problems in BEC physics and in this dissertation we propose possible experimental approaches to the latter two. The discussion that follows in the rest of this section describes the concepts and theory which underpin and motivate the experiments and numerical simulations in the rest of this dissertation.

1.1 Format of This Dissertation

In this dissertation I present two studies, one experimental and one numerical, describing novel experiments concerned with the generation and detection of vorticity in Bose-Einstein condensates. The first is an experiment demonstrating the relaxation dynamics of a BEC in a rotating Time-averaged Orbiting Potential (TOP) trap [11, 28] perturbed by a repulsive laser barrier. The data provided by this experiment are valuable to theoretical models as they present insight into the interactions between the condensed and thermal fractions of the atom cloud. The second is a numerical proof-of-principle study of a novel method of measuring the velocity field of a Bose-Einstein condensate using a 2D optical lattice in a manner analogous to a Shack-Hartmann Wavefront Sensor. This, among other applications, allows us to locate and determine the charge of quantum vortices. We call this method the Atom-Optical Shack-Hartmann Wavefront Sensor (AOSHWS).

The following sections of this chapter give an introduction to the history and physics of BECs. This chapter also covers the basics of quantum hydrodynamics as well as classical and quantum turbulence. Chapter 2 details important aspects of our experimental instrumentation. This includes diagrams of the magnetic coil assembly, mathematical descriptions of the relevant trapping fields and various other pieces of infrastructure. Chapter 3 details our experimental findings studying the relaxation of a BEC in a spinning TOP trap. It begins with a discussion of our optimization method for producing and imaging vortex lattices in-situ. We then discuss the free parameters of the experiment and present our results and conclusions. Chapter 4 details the theoretical underpinnings of the AOSHWS. We begin with a discussion of the classical Shack-Hartmann Wavefront Sensor from both the geometric and wave-optical perspectives. We then mathematically treat the AOSHWS to draw direct analogy between the two and discuss an algorithm for vortex identification. Chapter 5 presents the results of our numerical model of the AOSHWS and discusses its

performance for various configurations of parameters. Finally, Chapter 6 covers our conclusions and thoughts for future work to develop both of these subjects.

1.2 Background

1.2.1 Bose-Einstein Condensation

In 1924 Satyendra Nath Bose wrote a paper presenting a novel method to derive Plank's radiation law without relying on results derived from classical electromagnetism [1]. His method used a new method of counting the microscopic states of light quanta (photons) that preserved their indistinguishable nature and accounted for the limit on phase space volume dictated by the quantization of momentum and energy. In the same year Einstein, recognizing the importance of Bose's insight, demonstrated that the same method could be used for matter and presented a theory of a monoatomic ideal gas based on what is now called Bose-Einstein statistics [2]. The next year, Einstein returned to this theory to remark on an unusual property. He noted:

> According to the developed equation of state of the ideal gas there is for every temperature a maximum density of molecules being in agitation. If this density is exceeded, the excess molecules fall out into an unmoving state (they "condense" without attractive forces) [29].

This population of the lowest energy state by constituent particles above a critical density in an atomic gas is the first postulation of the state of matter known as a Bose-Einstein condensate. A BEC occurs when a macroscopic portion of an ensemble of bosons occupy the same quantum state in thermal equilibrium with the rest of the particles. Einstein's condensate would not be experimentally realized in an atomic gas (though not for lack of effort) until 1995 [3].

Modern physicists have developed a more detailed picture of the BEC phenomenon. The critical density Einstein postulated corresponds to the limit when the average inter-atomic spacing approximately matches the thermal DeBroglie wavelength of the atoms. When this occurs we may describe the dynamics of the resulting condensate with a single macroscopic wave function that describes all N particles

$$\Psi_N(\boldsymbol{r},t) = \sqrt{n(\boldsymbol{r},t)}e^{i\phi(\boldsymbol{r},t)} = \sqrt{N}\Psi_s(\boldsymbol{r},t). \tag{1.2.1}$$

Here, $n(\boldsymbol{r},t)$ and $\phi(\boldsymbol{r},t)$ are the atomic density and phase functions respectively at position $\boldsymbol{r}$ and time t. $\Psi_s(\boldsymbol{r},t)$ is a single-particle wave function that denotes the quantum state occupied by a given particle in the system. The wave function $\Psi_N(\boldsymbol{r},t)$ obeys the normalization relation:

$$\int dV|\Psi_N(\boldsymbol{r},t)|^2 = N. \tag{1.2.2}$$

where N is the number of atoms and dV is the R^3 volume element. The single-particle wave function $\Psi_s(\boldsymbol{r},t)$ is normalized to unity. Equation 1.2.2 demonstrates that probability densities of the entire ensemble of N particles are described by the field $\Psi_N(\boldsymbol{r},t)$ and thus, they are all in the same quantum state.

The wave function $\Psi_N(\boldsymbol{r},t)$ will be used extensively in following sections to describe the condensate. However, for the remainder of this section through 1.2.2 we will use the single-particle wave function $\Psi_s(\boldsymbol{r},t)$ for illustrative purposes and drop the subscript s. The dynamics of these wave functions are well-described at zero temperature by the Gross-Pitaevskii Equation (GPE) [24]. We obtain the GPE by minimizing the action associated with the many-particle Hamiltonian

$$H = \sum_{j=1}^{N}\left[-\frac{\hbar^2}{2m}\nabla_j^2 + V_1(\boldsymbol{r}_j)\right] + \frac{4\pi\hbar^2 a_s}{m}\sum_{i>j=1}^{N}\delta(\boldsymbol{r}_i - \boldsymbol{r}_j). \tag{1.2.3}$$

Where r_i is the location of the i^{th} particle, i and j are integers defined over the range $1, 2, ..., N$, a_s is the atomic s-wave scattering length, ∇^2 is the Laplacian operator,

$V_1(\mathbf{r})$ is the single-particle potential and the right-most term is a two particle pseudo-potential. We arrive at the simplified form of the pseudo-potential by assuming a gas of low temperature and dilute density and may now write the action

$$S = \int dt \int d\boldsymbol{r_1} ... \int d\boldsymbol{r_n} \Phi^* \left[i\hbar \frac{\partial}{\partial t} + \frac{\hbar^2}{2m} \sum_{j=1}^{N} \nabla_j^2 - \sum_{j=1}^{N} V_1(\boldsymbol{r}_j) \; ... \right. \\ \left. ... - \frac{4\pi\hbar^2 a_s}{m} \sum_{i>j=1}^{N} \delta(\boldsymbol{r}_i - \boldsymbol{r}_j) \right] \Phi. \tag{1.2.4}$$

The utility of the action is that by using variational methods we may use it to derive equations of motion for our system in terms of the multiparticle wave function $\Phi(\mathbf{r}_1, \mathbf{r}_2, ...\mathbf{r}_N, t)$. However, it would be of even greater utility if we could formulate our equations of motion in terms of the single-particle wave functions $\Psi(\mathbf{r}_j, t)$ in a manner that allows us to link their form to the two-particle interaction. To do this we use the Hartree approximation that assumes all particles occupy the same state, and has the form

$$\Phi(\mathbf{r}_1, \mathbf{r}_2, ...\mathbf{r}_N, t) = \prod_{j=1}^{N} \Psi(\boldsymbol{r_j}, t) \tag{1.2.5}$$

where each single-particle wave function is normalized to unity. Substituting this into the action we then evaluate the Euler-Lagrange equation for Ψ^*

$$\frac{\partial}{\partial t} \frac{\partial \mathcal{L}}{\partial \dot{\Psi}^*} = \frac{\partial \mathcal{L}}{\partial \Psi^*} - \sum_j \partial_j \frac{\partial \mathcal{L}}{\partial(\partial_j \Psi^*)} \tag{1.2.6}$$

where $\dot{\Psi}^*$ denotes the time derivative of Ψ^* and $\mathcal{L}$ is the Lagrangian density

$$\mathcal{L} = \Psi^* \left[i\hbar \frac{\partial}{\partial t} + \frac{\hbar^2}{2m} \sum_{j=1}^{N} \nabla_j^2 - \sum_{j=1}^{N} V_1(\boldsymbol{r}_j) - \frac{4\pi\hbar^2 a_s}{m} \sum_{i>j=1}^{N} \delta(\boldsymbol{r}_i - \boldsymbol{r}_j) \right] \Psi. \tag{1.2.7}$$

This yields the three-dimensional Gross-Pitaevskii Equation

$$i\hbar \frac{\partial \Psi}{\partial t} = -\frac{\hbar^2}{2m} \nabla^2 \Psi + V_1(\boldsymbol{r}) \Psi + \frac{4\pi\hbar^2 a_s}{m} (N-1) |\Psi|^2 \Psi, \tag{1.2.8}$$

a nonlinear Schrödinger equation that describes the behavior of the single-particle wave function when modified by the presence of multiple interacting particles or, in

our case, a BEC at T = 0K. The right-most term describes the nonlinearity of the system that depends entirely on two-particle interactions. $V_1(\mathbf{r})$ is the single-particle potential experienced equally by every particle in the system. The linear Schrödinger equation is recovered in the limits $a_s \to 0$ or $N \to 1$. For most of the following discussion we will make our treatment more compact by defining $g_{3D} \equiv \frac{4\pi\hbar^2 a_s}{m}$ and noting that for large ensembles of atoms $(N-1) \approx N$. The strength and sign of the nonlinearity depend on this constant coefficient.

Dimensional Reduction of the GPE to 2D form: Many of the turbulence experiments performed in BEC are done in a 2D geometry. This places fundamental constraints on the phase space of the system and simplifies the detection of vortices as the cores are aligned to the same axis and cannot form tangles. It therefore seems pertinent to include the process by which we modify the three-dimensional GPE to describe a BEC in this limit. Though the following treatment is suitable for a variety of potentials we will use a radially symmetric cylindrical harmonic oscillator potential

$$V_1(\boldsymbol{r}) = \frac{1}{2}m\omega_z^2 z^2 + \tilde{V}_1(\boldsymbol{\rho}) = \frac{1}{2}m\omega_z^2 z^2 + \frac{1}{2}m\omega_\rho^2|\boldsymbol{\rho}|^2 \tag{1.2.9}$$

where m is the mass of the atom, z is the axial coordinate, $\boldsymbol{\rho}$ is the transverse coordinate vector and ω_z and ω_ρ are the associated oscillator frequencies. In the 2D limit the atoms are tightly bound in the z-direction relative to the transverse dimensions such that $\omega_z >> \omega_\rho$. The tight confinement allows us to assume that for any level of excitation we may reasonably expect the system will remain in its ground state along z. This allows us to perform a dimensional reduction via separation of variables into axial and transverse components. The relevant relations that stem from these assumptions are

$$\begin{aligned} \Psi(\boldsymbol{r},t) &= \Psi_t(\boldsymbol{\rho},t)\chi_g(z)e^{-\frac{i}{\hbar}E_{g_z}t} \\ \nabla^2 &= \frac{\partial^2}{\partial z^2} + \nabla_{\boldsymbol{\rho}}^2 \end{aligned} \tag{1.2.10}$$

where $\Psi_t(\boldsymbol{\rho},t)$ and $\chi_g(z)$ are separately normalized and E_{g_z} is the single-particle ground state energy of the trap along the z direction. Substituting these relations into the 3D GPE, multiplying through by $\chi_g^*(z)$ and integrating over z we separate the GPE into two independent equations.

$$-\frac{\hbar^2}{2m}\nabla_{\boldsymbol{\rho}}^2\Psi_t(\boldsymbol{\rho},t)+\tilde{V_1}(\boldsymbol{\rho})\Psi_t(\boldsymbol{\rho},t)+\frac{Ng_{3D}}{l_{eff}}|\Psi_t(\boldsymbol{\rho},t)|^2\Psi_t(\boldsymbol{\rho},t) = i\hbar\frac{\partial\Psi_t(\boldsymbol{\rho},t)}{\partial t} \quad (1.2.11)$$

$$-\frac{\hbar^2}{2m}\frac{\partial^2}{\partial z^2}\chi_g(z)+\frac{1}{2}m\omega_z^2z^2\chi_g(z) = E_{g_z}\chi_g(z) \quad (1.2.12)$$

where $\frac{1}{l_{eff}}=\int_{-\infty}^{+\infty}dz|\chi_g(z,t)|^4$ has units of inverse length. Thus we find that when we reduce dimensions the energy per particle is reduced by a factor of l_{eff} such that we can write $g_{2D}=\frac{g_{3D}}{l_{eff}}=g_{3D}\int_{-\infty}^{+\infty}dz|\chi_g(z,t)|^4$. We may then conclude that Equation 1.2.11 can be used to describe the dynamics of a flat,"pancake shaped" BEC. Our final step is to produce the time-independent 2D GPE by introducing the following form of the transverse wave function:

$$\Psi_t(\boldsymbol{\rho},t)=\psi(\boldsymbol{\rho})e^{-\frac{i}{\hbar}\mu t} \quad (1.2.13)$$

where μ is the chemical potential of the condensate and is a measure of the energy due to interactions. Substituting and simplifying yields the time independent 2D GPE:

$$-\frac{\hbar^2}{2m}\nabla_{\boldsymbol{\rho}}^2\psi(\boldsymbol{\rho})+\tilde{V_1}(\boldsymbol{\rho}))\psi(\boldsymbol{\rho})+Ng_{2D}|\psi(\boldsymbol{\rho})|^2\psi(\boldsymbol{\rho})=\mu\psi(\boldsymbol{\rho}). \quad (1.2.14)$$

The majority of the simulations presented in this thesis are accomplished by a split-step numerical solving of Equation 1.2.11 [30].

1.2.2 The Condensate Wave Function

Now that we have developed a model for a 2D condensate we would like use it to determine an appropriate wave function. As the GPE is a nonlinear partial differential equation there are few cases where an analytical solution is possible. We will discuss two different methods to determine an approximate solution for the ground state and

from them develop expressions for important properties of the condensate. These methods are well-known [24] and so we will be brief. Further, we will assume a cylindrically symmetric, harmonic trapping potential and restrict analysis to two dimensions.

The Variational Gaussian Method: We will start from the following trial solution in the loosely bound direction:

$$\psi(\boldsymbol{\rho}) = \frac{1}{\sqrt{2\pi}(\pi W_\rho^2)^{\frac{1}{4}}} e^{\frac{-\rho^2}{2W_\rho^2}} \tag{1.2.15}$$

where $\rho = |\boldsymbol{\rho}|$ and W_ρ is a real constant to be varied. This function is then substituted into the energy functional that corresponds to our 2D GPE that may be derived as follows: *Multiply both sides of the 2D GPE by ψ^* and integrate over all space. The former step gives an expression for the chemical potential, $\mu = \frac{\partial E}{\partial N}$. Integrate the chemical potential over N to obtain the total energy, yielding*

$$E = N \int d\boldsymbol{\rho} \left[\frac{\hbar^2}{2m} |\nabla_{\boldsymbol{\rho}} \psi(\boldsymbol{\rho})|^2 + \tilde{V}_1(\boldsymbol{\rho}) |\psi(\boldsymbol{\rho})|^2 + \frac{N g_{2D}}{2} |\psi(\boldsymbol{\rho})|^4 \right]. \tag{1.2.16}$$

The method then follows standard variational principles allowing the widths to vary such that the energy is extremized assuming the condensate is tightly bound in the z-direction.

The Thomas-Fermi Approximation: The Thomas-Fermi solution to the GPE is one of the most common and important in the BEC literature. Valid for repulsive interaction and large atom number, the approximation is to assume that the non-linearity and potential energy dominate the kinetic energy term. We can then ignore the spatial derivatives in the GPE which allows us to solve for the wave function algebraically:

$$\psi(\boldsymbol{\rho}) = \begin{cases} (\frac{\mu - \frac{1}{2} m \omega_\rho^2 \rho^2)}{gN})^{\frac{1}{2}} & \rho \leq \sqrt{\frac{2\mu}{m\omega_\rho^2}} \\ 0 & \text{Otherwise.} \end{cases} \tag{1.2.17}$$

This wave function represents the spatial distribution of particles that occurs at equilibrium between the potential and the inter-particle repulsion. We compare the

magnitudes of the two energy terms numerically by expressing the nonlinear amplitude Ng_{2D} in units of the natural harmonic oscillator energy $E_0 = \hbar\omega_\rho$. Figure 1.1 compares the Thomas-Fermi distribution with the single-particle ground state versus multiples of the natural harmonic oscillator length $\sigma_0 = \sqrt{\hbar/m\omega_\rho}$.

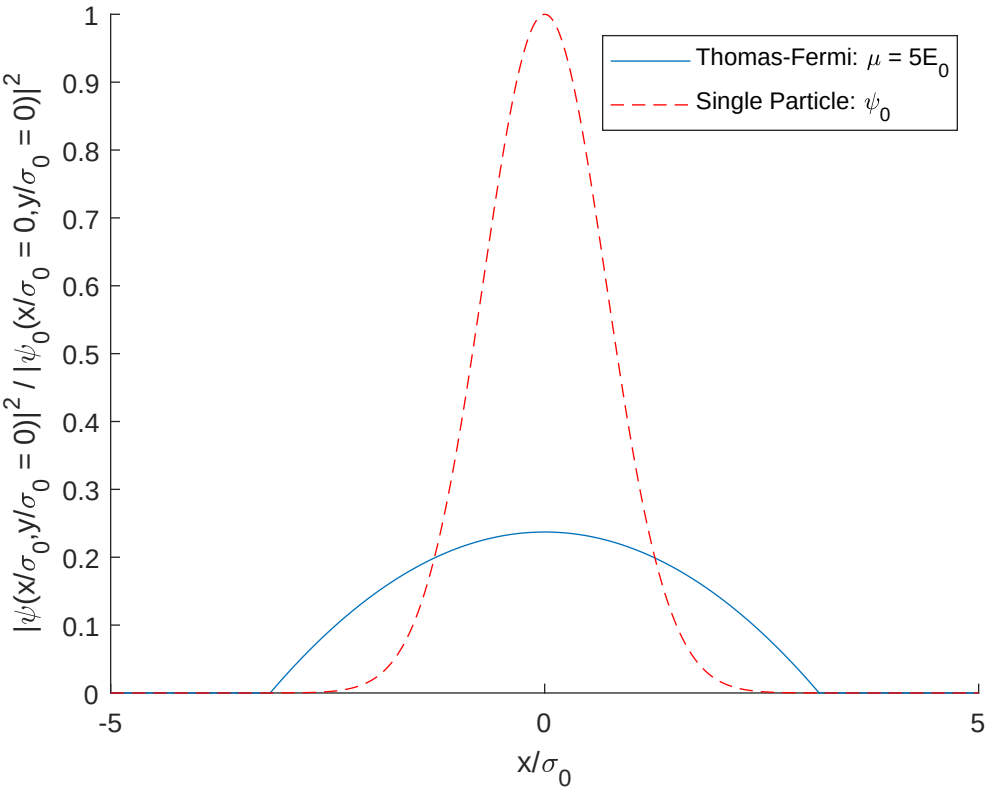

FIGURE 1.1. The Thomas-Fermi ground state and single-particle ground state square amplitudes divided by the single-particle ground state maximum for comparison.

From Figure 1.1 we can see that the Thomas-Fermi wave function abruptly vanishes at some maximum condensate radius. This is important to note as the approximation breaks down since the wave function derivative is discontinuous at this boundary. This can be dealt with numerically, however, for our purposes this detail should not pose a problem. Finding the zeroes of the wave function yields an

expression for the condensate radius

$$R_{max} = \left(\frac{2\mu}{m\omega_\rho^2}\right)^{\frac{1}{2}}. \tag{1.2.18}$$

We can derive an expression for the chemical potential from this model by enforcing the normalization of the wave function over its domain and rearranging the resulting expression. We may then calculate the total energy by integrating over particle number. In two dimensions we find the following:

$$\mu = 2\hbar\omega_\rho \left(\frac{Na_s}{l_{eff}}\right)^{1/2} \tag{1.2.19}$$

$$E = \int dN\mu = \frac{2}{3}N\mu. \tag{1.2.20}$$

These results allow us to completely characterize the wave function with the trapping frequencies and Thomas-Fermi radii which are easily accessible to experimental measurement.

1.2.3 Vortices in Bose-Einstein Condensates

Though the Hartree approximation in Equation 1.2.5 assumes the condensate consists of a collection of atoms occupying the same single-particle ground state of a confining potential there can be perturbative excitations of atoms above the ground state. These excitation modes are dealt with via Bogoliubov theory which we consider here in 3D. The wave function is broken into bulk and perturbative components like

$$\psi(\boldsymbol{r}, t) = e^{-i\mu t}\left[\psi(\boldsymbol{r}) + \delta\psi(\boldsymbol{r}, t)\right] \tag{1.2.21}$$

By subbing this form of the wave function into the GPE and truncating the $\delta\psi$ terms at second order we can develop equations of motion and solve for the various possible modes of excitation [24]. An important figure of merit that characterizes the BEC with respect to perturbation is the healing length

$$\xi(\boldsymbol{r}) = 1/\sqrt{8\pi a_s n(\boldsymbol{r})}. \tag{1.2.22}$$

The healing length is the distance over which the BEC density returns to the bulk value from zero due to a delta function repulsive perturbation. It can be intuited as a measure of the width of the condensate's spatial impulse response or the matter wave coherence length and establishes a natural scale that we will use to quantify disturbances to the condensate. We can see that it depends inversely on the local density and so, in general, the dynamics of various excitations will be affected by the BEC density profile. For a sense of scale, most BECs created in this experiment have a trapped diameter on the order of 100 microns for atom numbers $N \sim 10^6$, the corresponding healing length in the bulk fluid is about half a micron.

Hydrodynamic Picture of Superfluidity: As we stated previously we are particularly interested in the superfluid properties of BEC. In the following we will show how quantized vortices follow from the basic properties of superfluidity and discuss their qualities. Much of this treatment will follow Pethick and Smith [24]. Though much of the following is general to three dimensions we will restrict our discussion to 2D and define $\boldsymbol{r}$ as the R^2 coordinate vector.

The BEC is described by the N-particle wave function $\Psi_N(\boldsymbol{r}, t)$ and we will drop the subscript for the rest of our treatment.

$$\Psi(\boldsymbol{r}, t) \equiv \Psi_N(\boldsymbol{r}, t) = \sqrt{n(\boldsymbol{r}, t)} e^{i\phi(\boldsymbol{r}, t)} \tag{1.2.23}$$

From a hydrodynamic perspective a BEC can be thought of as a small droplet of superfluid characterized by a velocity field

$$\boldsymbol{v}(\boldsymbol{r}, t) = \frac{\hbar}{m} \nabla \phi(\boldsymbol{r}, t) \tag{1.2.24}$$

where $\phi(\boldsymbol{r}, t)$ is the phase profile of the condensate order parameter defined in Equation 1.2.23 which must everywhere have a single value. From Equation 1.2.24 we can see that a superfluid must be irrotational since the curl of a gradient field must be zero.

$$\boldsymbol{\nabla} \times \boldsymbol{v}(\boldsymbol{r}, t) = \boldsymbol{\Upsilon}(\boldsymbol{r}, t) = 0 \tag{1.2.25}$$

However, this condition is lifted at a phase singularity where the curl becomes infinite and the density necessarily drops to zero so that the wave function stays single-valued and energy is conserved. Since there is no fluid in the region of the singularity a contour through the superfluid may not contain it and thus remains irrotational. The region near the singularity is referred to as the *vortex core* and has a radius on the order of the healing length. From the single-valued condition it also follows that the change of the phase around a closed loop anywhere in the condensate must equal an integer multiple of 2π. This constrains the circulation of the condensate like

$$\Gamma = \oint \boldsymbol{v} \cdot d\boldsymbol{l} = \frac{\hbar}{m} 2\pi\gamma \tag{1.2.26}$$

Where $\boldsymbol{l}$ is a closed loop and $\gamma = ...-1, 0, 1...$ is an integer called the *winding number* or *charge*. The winding number is non-zero only if the contour $\boldsymbol{l}$ encloses the axis of a vortex. Thus we see that Onsager's intuition was correct and that any vortex in a superfluid must have circulation quantized in units of $\frac{h}{m}$. From Equation 1.2.25 we conclude that *a superfluid can fluid circulating only due to the presence of one or more quantized vortices.*

Assuming a cylindrically symmetric condensate and a single, centrally placed vortex, single-valuedness also necessitates that the wave function must vary like $e^{i\gamma\phi}$ where ϕ is the azimuthal angle. We may therefore derive from Equation 1.2.24 that the rotational velocity of a quantized vortex must vary like

$$v_\phi = \frac{\gamma\hbar}{mr} \tag{1.2.27}$$

where r is the radial distance from the vortex core. Since the velocity diverges in the limit where r approaches zero the condensate density function $n(\boldsymbol{r}, t)$ must vanish at the axis of the vortex in order to conserve energy. To calculate the energy required to excite a condensate of the lowest energy state to a single vortex state of charge $|\gamma| = 1$ under these assumed conditions we write the wave function for the condensate as

$$\psi(\boldsymbol{r}) = f(r)e^{i\gamma\phi}. \tag{1.2.28}$$

We can evaluate the energy functional for this wave function using the Hamiltonian from Equation 1.2.3

$$E = \int d\boldsymbol{r}\psi^* H\psi \tag{1.2.29}$$

In doing so we find the same form of the energy as the uniform state plus an extra term

$$\int d\boldsymbol{r}\frac{\hbar^2\gamma^2 f^2}{2mr^2}. \tag{1.2.30}$$

This is just the contribution from the kinetic energy density of the vortex $\frac{1}{2}mv_\phi^2 f^2$ and by evaluating the integral we may calculate the excited state energy of the condensate under these conditions.

We have so far assumed a single vortex placed at the center of a cylindrically symmetric trap oriented along the z-axis. We can generalize our treatment to include multiple vortices with arbitrary placements in the x-y plane by modifying Equation 1.2.25 like

$$\boldsymbol{\nabla}\times\boldsymbol{v} = \hat{z}\frac{h}{m}\sum_{i=1}^{M}\gamma_i\delta^2(\boldsymbol{r_i}) \tag{1.2.31}$$

where $\delta^2(\boldsymbol{r})$ is a two-dimensional delta function in the x-y plane, M is the number of vortices and γ_i and r_i are the charge and location of the i^{th} vortex respectively. The addition of multiple vortices at various locations introduces a rich variety of dynamics into the system as vortex cores move due to each other's velocity fields. In addition a vortex located off of the point of symmetry of a superfluid of finite extent will experience forces due to to boundary. These forces may be accounted for using a method of image vortices similar to that used in electrodynamics for charges.

Structure of a Quantum Vortex: We have, in a somewhat hand-waving manner, said that the superfluid density vanishes at the location of the vortex phase singularity. We have not discussed the manner in which the density decreases to zero or how the shapes of the cores effect the properties of the superfluid flow. There are a number

of methods to treat this problem and its ramifications are too numerous to be fully within the scope of this document but we will now present a brief overview.

The problem comes down to determining a solution for the function $f(r)$ which first appeared in Equation 1.2.28. We will consider the problem in two dimensions by assuming tight confinement in the z-direction and integrating the density along this axis. We consider only a single vortex placed at $\boldsymbol{r} = 0$ so that $r = |\boldsymbol{r}|$ is the distance from the vortex core. Defining the scaled amplitude $A_{vort}(r) = f(r)/f_0$ where f_0 is the bulk amplitude of the condensate we can separate the wave function amplitude into the product

$$\sqrt{n(r)} = g(r)A_{vort}(r) \tag{1.2.32}$$

where $g(r)$ is the density of the condensate and $A_{vort}(r)$ is the vortex density envelope function. This envelope function may be calculated by minimizing the total energy per unit length associated with the vortex for a strategically chosen ansatz. The resulting form is

$$A_{vort}(r) = \frac{r}{\sqrt{(\xi/\Lambda)^2 + r^2}} \tag{1.2.33}$$

where Λ is the variational constant that determines the slope of the vortex core at a chosen location.

1.2.4 Basic Concepts of Turbulence

Turbulence in fluids is classified as flow that displays chaotic changes in pressure and velocity [31]. Spectra of length scales l and associated spatial frequencies $k = \frac{2\pi}{l}$ are associated with the modes of fluid motion. A forcing mechanism injects kinetic energy into modes associated with the corresponding length scales. This energy is then transferred to modes of different length scales in an energy cascade. In idealized 3D classical turbulence the energy cascade conserves and carries kinetic energy from the scale of the forcing mechanism to smaller scales, eventually to the scale of viscous damping where energy is dissipated. When forcing is not present the fluid will

come to rest after the kinetic energy is depleted by the damping. In contrast, in 2D turbulence forcing at small length scales results in an inverse energy that transports energy to larger length scales up to the size of the system. The region of the spectrum over which an energy cascade occurs is called the *inertial range*. Since the spatial structures of turbulent flows are irregular they are quantified statistically by measures such as energy spectra. Classical 3D turbulence is characterized by a spectrum that is proportional to $k^{-5/3}$ in the inertial range as shown in 1941 by Kolmogorov [32,33]. Also characteristic of 3D turbulence is a cascade of vorticity from large to small rotating patches known as a *Richardson cascade* [34]. Classical turbulence in an unforced, undamped, 2D fluid conserves a statistical quantity called enstrophy. Enstrophy is related to the square average vorticity according to

$$Z = \frac{1}{2}\langle \Upsilon^2 \rangle. \tag{1.2.34}$$

Due to this inviscid invariant 2D turbulence displays an inverse energy cascade from the scale of forcing to that of the system and, as a result, an inverse Richardson cascade. This establishes an inertial range over a different region of the spectrum. The enstrophy, however, cascades from the forcing scale to smaller scales. Thus, there are several distinct trends present over the spectrum [35].

Onsager developed a statistical theory for 2D turbulence based on a Hamiltonian model for *point vortices* [36]. Point-vortices are an idealization of two-dimensional rotational flow where a velocity field circulates about a highly localized source. In Onsager's model, the equations of motion for N such vortices in an infinite plane are

$$\kappa_i \frac{dx_i}{dt} = \frac{\partial H}{\partial y_i} \tag{1.2.35}$$

$$\kappa_i \frac{dy_i}{dt} = \frac{\partial H}{\partial x_i} \tag{1.2.36}$$

where κ_i is the circulation of the i^{th} vortex, (x_i, y_i) is its location and H is the kinetic energy of the fluid. In this model H is completely determined by the two degrees of

freedom of each vortex:

$$H = -\frac{1}{2\pi}\sum_{i<j}\kappa_i\kappa_j \ln(r_{ij}/L) \tag{1.2.37}$$

where r_{ij} is the spatial separation between the i^{th} and j^{th} vortex and L is an arbitrary length scale. For a more general, bound system the natural logarithm may be replaced with a Green's function for the Laplacian that takes boundary conditions into account. Based on our previous description of quantum vortices and superfluid hydrodynamics this model seems like a good starting point for a description of 2D quantum turbulence.

1.2.5 Quantum Turbulence

Superfluid motion has distinct characteristics from classical fluid motion including quantized vorticity and lack of viscosity. The implications of these properties with respect to superfluid turbulence are discussed by Barenghi et al. [37]. As previously stated, the work in this dissertation is primarily motivated by 2D quantum turbulence (2DQT). The compressible nature of atomic BECs along with the ability to create highly oblate trapping geometries allow us to experimentally access a quasi-2D regime of superfluid motion. The characteristics of compressible quantum turbulence in two dimensions are discussed by Neely et al. [38].

Since a BEC is compressible we can split the fluid motion into incompressible and compressible components [23]:

$$\boldsymbol{v}(\boldsymbol{r}) = \boldsymbol{v}_i(\boldsymbol{r}) + \boldsymbol{v}_c(\boldsymbol{r}). \tag{1.2.38}$$

The incompressible portion must follow the relation

$$\nabla \cdot [\sqrt{n(\boldsymbol{r})}\boldsymbol{v}_i(\boldsymbol{r})] = 0. \tag{1.2.39}$$

A velocity field satisfying this relation must contain no sound waves. This relation holds to good approximation in the presence of multiple vortices so long as the cores

are separated by a few healing lengths. The kinetic energy spectra are given by

$$\begin{aligned} E &= \frac{m}{2} \sum_{j=x,y} |\boldsymbol{F}_j(\boldsymbol{k})|^2 \\ &= \frac{m}{2} \sum_{j=x,y} | \int d^2\boldsymbol{r} e^{-i\boldsymbol{k}\cdot\boldsymbol{r}} \boldsymbol{v}_j(\boldsymbol{r})|^2 \end{aligned} \tag{1.2.40}$$

where $\boldsymbol{F}_j(\boldsymbol{k})$ is the Fourier transform of the velocity field. The incompressible spectrum corresponds to quantum vortices while the compressible portion is contributed by acoustic waves. The dynamics of the system and therefore the spectrum will vary greatly in different regimes due to coupling between these two components. For instance, oppositely charged vortices may recombine to release a sound wave coupling kinetic energy from the incompressible spectrum directly into the acoustic field. In a regime where this process dominates, it can suppress an inverse energy cascade since enstrophy is not conserved. However, in a regime where like-charged vortex clustering dominates (due to an inverse Richardson cascade) recombination is suppressed since the oppositely charged populations are kept separate. Under these conditions an inverse cascade may be observed. These two scenarios are determined by how enstrophy is introduced into the system that, in turn, depends on the nature of the forcing. Neely et al. and Helmerson et al. produced experimental results in 2019 that suggest the observation of large scale clustering of quantized vortices in 2D BECs [12, 39].

For a single quantum vortex and no other excitations of the condensate the kinetic energy spectrum is purely incompressible. Defining the unit of enstrophy as

$$\Omega \equiv \frac{2\pi\hbar^2 n_0}{m\xi^2} \tag{1.2.41}$$

where n_0 is the bulk density of the superfluid, the spectrum for this vortex can be expressed for two limiting cases as

$$E_i^1(k)|_{k\xi\ll 1} = \Omega\xi^3\Lambda^{-1}\left(\frac{1}{k\xi}\right) \text{ and } E_i^1(k)|_{k\xi\gg 1} = \Omega\xi^3\Lambda^{-1}\left[\frac{\Lambda^2}{(k\xi)^3}\right], \tag{1.2.42}$$

where we have used the vortex density profile from Equation 1.2.33. The regimes $k\xi \ll 1$ and $k\xi \gg 1$ are known as the infrared and ultraviolet, respectively. There is

a crossover region in the vicinity of $k\xi \sim 1$ that corresponds to a length scale on the order of the vortex core. This analysis can be extended to an N-vortex arrangement and yields the kinetic-energy spectrum

$$E_i^N(k) = \frac{\Omega\xi^3}{\Lambda} F(k\xi) \sum_{p=1,q=1}^{N} \kappa_p \kappa_q J_0(k|\boldsymbol{r_p} - \boldsymbol{r_q}|) \tag{1.2.43}$$

where $J_n(x)$ is an nth order Bessel function of the first kind. We note that Equation 1.2.43 is analogous to the Green's function generalization of Onsager's point vortex Hamiltonian in Equation 1.2.37. Equation 1.2.43 gives us the incompressible energy spectra over various length scale ranges for arbitrary configurations of vortices. One main goals of this dissertation is to present a realistic experimental method to measure the velocity field of a BEC. This allows determination of the kinetic energy spectrum in two ways. The first way is by direct Fourier transform of the velocity field as in Equation 1.2.40 which is valid for both compressible and incompressible velocity fields. The second way is to analyze the velocity field spatially to determine the location and charge of every vortex and determine the incompressible kinetic energy spectrum via Equation 1.2.43. Comparing the results from the two methods would allow us to determine the accuracy and regimes of validity of the Onsager point vortex model.

1.2.6 A Review of Vortex Lattices

We have, for several sections, discussed aspects of vortices in a condensate. We have not, however, presented an experimental method by which to induce rotation. There are numerous methods to generate vorticity in a BEC, the first of which was realized by Matthews et al. in 1999 [16] following a proposal by Williams and Holland the same year [17]. Some other methods have been demonstrated by Leanhardt et al. in 2002 where vortices were imprinted into a BEC via a quadrupole magnetic field [15], Scherer et al. in 2007 where vortices were generated by merging three

separated condensates [13] and vortex dipoles were generated by Neely et al. in 2010 by swiping a repulsive barrier through a BEC [7], along with many others. A method of generating vortices by rotating the confining potential was demonstrated by Hodby et al. in 2001 [11]. In this dissertation we propose a new method of generating vorticity in BECs trapped in potentials rotating far from surface wave resonances. We provide new data regarding the relaxation of an out-of-equilibrium, finite temperature BEC in a rotating TOP trap. We hope that the techniques and data presented here will serve theoretical interests to develop finite-temperature GPE models of these dynamics.

A superfluid in a trap cannot be induced to rotate by spinning the trap about any axis of symmetry. This is because angular momentum is conserved about such an axis and there are no frictional interactions with the container walls. In order to couple angular momentum into a condensate by spinning its trap we must induce anisotropy about the rotation axis. A detailed explanation of the experimental methods that we use in our lab to achieve BEC rotation are discussed in Chapter 3. The energy of a cloud of atoms in a rotating frame is given by

$$E' = E - \boldsymbol{L} \cdot \boldsymbol{\omega}_s \tag{1.2.44}$$

where E is the energy of the cloud in the stationary frame, $\boldsymbol{L}$ is the angular momentum vector of the atom cloud and $\boldsymbol{\omega}_s$ is the angular velocity vector of the rotating trap anisotropy. In the rotating frame we can see that the ground state wave function of the non-rotating trap is no longer energetically favorable so long as the angular velocity exceeds a value corresponding to the energy gap between the ground state E_L and the lowest excited state of the stationary frame E_0. If a state has angular momentum magnitude L along the rotation axis its critical angular velocity is given by

$$\omega_c = \frac{E_L - E_0}{L}. \tag{1.2.45}$$

This value will depend on the specific excitation. The *lower critical angular velocity*,

ω_{c1} is that below which the non-rotating state is favorable. It can be shown that the lower critical angular velocities correspond to various vortex states while surface waves can be excited at higher angular velocities. As $|\boldsymbol{\omega_s}|$ becomes large compared to ω_{c1} the lowest energy state for a condensate is one consisting of N_v regularly spaced vortices where

$$N_v = \frac{mR|\boldsymbol{\omega_s}|}{\hbar} \tag{1.2.46}$$

and R is the radius of the BEC [24]. In 1965 Tkachenko showed that this spacing corresponds to the vortex cores being arranged at the verticies of a triangular lattice [40]. Thus, to generate a many vortex state in a rotating BEC one may rotate the trap at a high angular velocity resonant with a surface wave. If the trap remains rotating, the higher energy excitation will decay into the equilibrium state: a triangular vortex lattice. A vortex lattice in an atomic gas BEC was first observed in BEC by Madison et al. in 2000 and for larger numbers of vortices by Abo-Shareer et al. in 2001 [14, 41]. The vortex lattice is an important state as it is the equilibrium of a rotating condensate towards which any unstable state must evolve in a rotating trap. An example of a vortex lattice generated by spinning a TOP trap is shown in Figure 1.2.

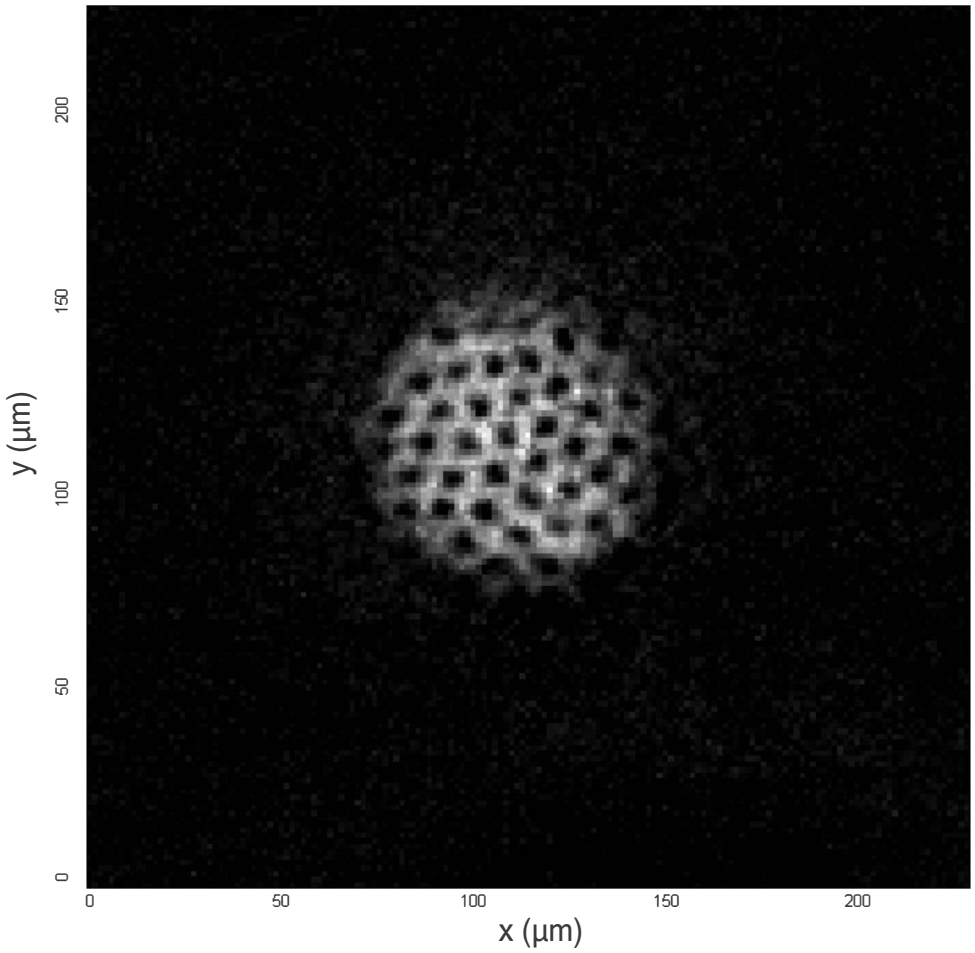

FIGURE 1.2. In-situ image of a vortex lattice in a BEC.

CHAPTER 2

Experimental Instrumentation

The large majority of the experimental apparatus used in this dissertation is described in the theses of David Scherer and Kali Wilson [10, 13]. However, certain methods regarding the TOP trap are important to this work and we will review them in the following sections. We also made significant changes to the process of evaporation which will be detailed.

2.1 TOP Trap

Magnetic field traps may generally be separated into two varieties: those that have a potential minimum at zero-field and those that have their minimum at a finite value. Our cooling process begins with a sample of atoms in a spherical quadrupole magnetic trap, generated by an anti-Helmholtz coil pair, which allows for efficient cooling due to a high elastic collision rate. However, once the ensemble reaches a low enough temperature, Majorana losses start to kick in due to the zero-point in the field. To continue cooling we must transfer the atom cloud to the latter variety of trap [24].

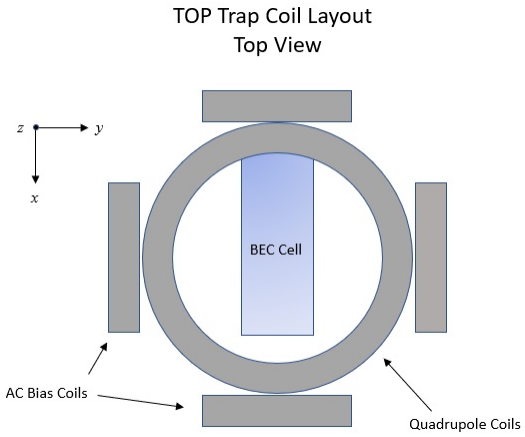

FIGURE 2.1. A top view of the layout of the coils used to magnetically confine the atoms in the BEC vacuum chamber. Distances are not to scale.

We use a variety known as a Time-averaged Orbiting Potential (TOP) trap [42]. Our TOP trap consists of a spherical quadrupole field with gradient B' and an AC bias of strength B_0 and direction that is modulated at frequency $\omega_{TOP} = 2\pi \times 4$ KHz. These fields are generated by two pairs of Helmholtz coils in a plane defined by their axes of symmetry, mutually orthogonal with the axis of a pair of anti-Helmoholtz coils as shown in Figure 2.1. Adding a bias field to the spherical quadrupole gradient shifts the zero point of the field by an amount $r_d = B_0/B'$, known as the "Circle of Death" radius. If we vary their field like

$$\boldsymbol{B_b}(t) = B_0 \left[\cos(\omega_{TOP}t)\hat{\boldsymbol{e}}_x + \sin(\omega_{TOP}t)\hat{\boldsymbol{e}}_y\right] \tag{2.1.1}$$

then the zero-point of the field will rotate in a circle in the plane. If the bias field is large enough or the gradient small enough the radius of the circle will be larger than the radius of the atom cloud and the resulting time-averaged potential for an atom with magnetic moment μ will be

$$\begin{aligned} U_{TOP}(r) &= \frac{\mu}{2}(B''_{\boldsymbol{r}}r^2 + B''_z z^2), \\ B''_r \equiv \frac{B'^2}{2B_0}, B''_z &\equiv \frac{4B'^2}{B_0} \end{aligned} \tag{2.1.2}$$

which is a harmonic trap [28] with circular symmetry in the x-y plane and the potential at the center of the trap is $U_{TOP}(r = 0) = \mu_m B_0$. The resulting trapping frequencies are

$$\begin{aligned} \omega_x = \omega_y &= \left[\frac{\mu B_z'^2}{8mB_0}(1+\eta^2)\sqrt{1-\eta^2}\right]^{1/2} \\ \omega_z &= \left[\frac{\mu B_z'^2}{mB_0}(1-\eta^2)^{3/2}\right]^{1/2} \end{aligned} \tag{2.1.3}$$

where m is the atomic mass of ^{87}Rb and $\eta = mg/\mu B_z'$ is a factor that accounts for sag due to gravity measured relative to a quadrupole trap minimum [43]. Our BECs are formed in a trap with frequencies $\omega_{r,z} = 2\pi \times (8.9, 17.8)$ Hz.

The condensates in this dissertation are in the $5^2S_{1/2}$ F = 1 ground state manifold of ^{87}Rb that has one magnetically trappable Zeeman spin state $|F = 1, m_f = -1\rangle$ and two untrapped states $|F = 1, m_f = 0\rangle$ and $|F = 1, m_f = 1\rangle$. The atoms start as a thermal cloud at ∼300 μK of around 10^9 atoms transferred from a 3D MOT to a quadrupole field of $B_z' = 133.3$ G/cm which is ramped to 221.6 G/cm over 3 s when evaporative cooling begins. The details of this process are as follows. Evaporative cooling of the thermal cloud occurs by inducing a transition from the trapped state to the untrapped states driven by an RF field swept linearly in frequency from high to low in segments called *cuts*. Between each cut is a period of rethermalization where elastic collisions distribute the kinetic energy of the remaining atoms. Evaporative cooling begins with a high frequency cut from $\nu_{HF} = 100$ MHz to 80 MHz over 2 s to remove the most energetic atoms in the sample. The *quadrupole cut* begins at $\nu_{QC} = 80$ MHz and ends at 12.7 MHz over 12 s yielding a thermal cloud with a temperature of ∼100 μK. This cut rapidly cools the cloud to a point just before the Majorana loss rate begins to dominate evaporative phase-space gains. We then ramp the field gradient to a value of $B_z' = 75$ G/cm over 500 ms before snapping it back to 221.6 G/cm while simultaneously turning on the AC bias field at $B_0 = 27.3$ G. This process approximately mode-matches the cooled cloud in the quadrupole trap with

the harmonic TOP trap and is called the *TOP catch*. The cloud is held in the TOP trap for 2 s with no RF to rethermalize. The bias field strength is then ramped from its catch value to $B_0 = 5$ G over 25 s while the RF follows this ramp at a frequency equal to 98 percent of the Zeeman splitting at the circle of death. This magnetic trap configuration with fields $B_0 = 5$ G, $B'_z = 221.6$ G/cm is called the *tight trap*. The cloud in the tight trap has a temperature on the order of ~ 1 μK. In the tight cut we sweep the RF frequency down to $\nu_{TC} = 4.535$ MHz over 10 s and then hold the cloud for 4s. This cut is designed to bring the cloud to a temperature approximately twice that of the critical temperature ($\sim$ 50 nK) for condensation with an atom number $N \approx 5 \times 10^6$. We then ramp the gradient to $B'_z = 47$ G/cm, a condition called the *sagged trap*. During this time we also ramp the RF to 71 % of the sagged trap circle of death and subsequently sweep it down to approximately $\nu_{SC} = 4.85$ MHz in a ramp called the *sag cut*. After a final 4s hold this results in a condensate of $1.5 \times 10^6 - 3 \times 10^6$ atoms.

2.2 Rotating the TOP Trap

To create a rotating trap we follow the work of Hodby et al. [11] and add a modulating signal to the AC TOP trap coils at frequency ω_s. This stretches the potential in the x-y plane into an ellipse whose major axis rotates in the plane at a frequency $\omega_{spin} = \frac{|\omega_s - \omega_{TOP}|}{2}$. The magnetic field then is

$$\boldsymbol{B}_b(t) = [B_0 \cos(\omega_{TOP} t) + B_\epsilon \cos(\omega_s t)]\, \hat{\boldsymbol{e}}_x + [B_0 \sin(\omega_{TOP} t) - B_\epsilon \sin(\omega_s t)]\, \hat{\boldsymbol{e}}_y \quad (2.2.1)$$

where B_ϵ is the strength of the modulating magnetic field which induces trap rotation. Increasing B_ϵ increases the ellipticity of the trap that is defined as $E = \frac{B_\epsilon}{B_0}$. The ellipticity of the trap is also characterized by the *deformation parameter*

$$\epsilon = \frac{\omega_0^2 - \omega_\epsilon^2}{\omega_0^2 + \omega_\epsilon^2}. \quad (2.2.2)$$

Our AC TOP field is generated by a DS345 SRS function generator which outputs a $\omega_{TOP} = 2\pi \times 4$ KHz sine wave with a peak-to-peak voltage of 1.24 V. The TOP is ramped by modulating this amplitude with a second SRS that outputs an arbitrary waveform written to it from the computer via GPIB. This signal goes through a phase-shifter circuit described in the thesis of David Scherer [13] that splits the signal into two channels for the x and y coil pairs and allows adjustment of their relative amplitude and phase. The output of this pair then goes directly into an audio power amplifier that provides the necessary current in each channel to drive the bias coils. The ellipse is generated by another DS345 SRS that provides amplitude modulation and an Agilent 3312A function generator providing the sinusoid. The ellipse function generators are triggered separately from the TOP trap generators and have an independently variable frequency ω_s and amplitude V_ϵ. The output of the ellipse function generator pair goes to a second input to the phase-shifter circuit where it is processed by a circuit identical to that which handles the TOP trap signal. The ellipse signal is split into two copies with variable relative phase and amplitude. These two voltages are then added to the respective channels of the main TOP signal as shown in Figure 2.2.

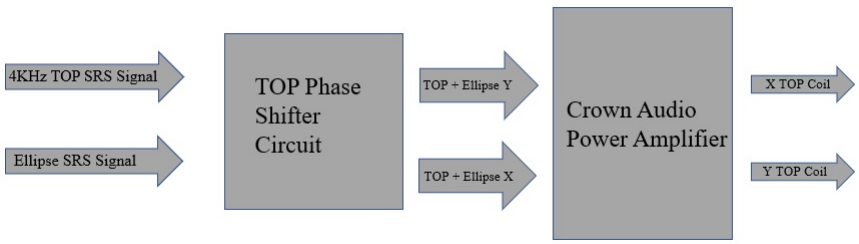

FIGURE 2.2. Block diagram showing the TOP and ellipser electrical system flow.

There is a surface wave resonance at $\omega_{spin} = 0.7 \times \omega_{trap} = 2\pi \times 6.25$ Hz which excites a quadrupole mode of the condensate that will decay into a large number of co-circulating vortices [11]. This is the primary method by which we have generated

large vortex distributions in the past. However, if we spin the trap at a frequency away from this resonance the condensate will remain stationary in a rotating trap. Since the minimum energy state of a BEC in rotating frame is a vortex lattice at discussed previously, the uniform, Thomas-Fermi state must be metastable. Studying the dynamics during relaxation of the uniform state to the rotating state will be the basis for the experiment described in Chapter 3.

2.3 Optical and Magnetic Trap

In order to achieve the trap geometry necessary to realize the 2D dynamics we have previously discussed we employ a hybrid optical and magnetic trap. We do not use this trap for the experimental work in this dissertation. However, since the simulations that follow in Chapter 6 are all in a 2D BEC we will give a short description of the experimental system that has been used to create highly oblate BECs. A more complete description of the system may be found in the thesis of Tyler Neely [8].

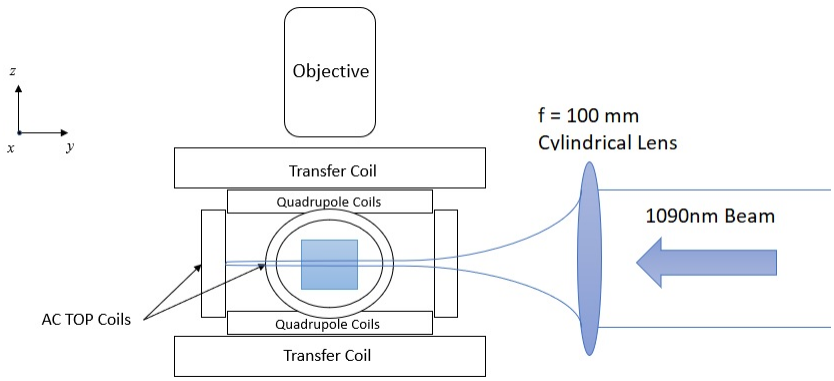

FIGURE 2.3. Hybrid trap layout.

To reach a 2D limit we create a trap that has a harmonic trapping frequency $\omega_z \approx 10\omega_{x,y}$. This is achieved with a red-detuned 1090 nm laser propagating in the negative y direction, cylindrically focused in the z-direction and incident on the BEC

held in the TOP trap. As shown in the layout of the optical trap system in Figure 2.3 the 1090 nm beam propagates along the y axis through an $f = 100$ mm cylindrical lens. The beam is focused to $1/e^2$ radii of $w_x \sim 2$ mm and $w_z \sim 20$ μm at the location of the BEC. For a laser power $P_{1090} \sim 300$ mW the trap frequency in the confining direction has been measured at $\omega_z = 2\pi \times 70$ Hz [10]. For sagged trap radial frequencies measured at $\omega_\rho = 2\pi \times 8.9$ Hz we can easily reach the 10:1 ratio with slightly higher laser powers.

2.4 TOP Trap Interlock Circuit

To protect the AC TOP coils from current surges or other failure modes we created a current interlock system. The circuit diagram is shown in Figure 2.4. An F.W. Bell CLN-200 Hall probe monitors the 4 KHz AC current from both channels of the audio power amplifier. The Hall probe signal is fed into the interlock circuit that begins with two half-wave rectifiers with a 180-degree phase difference and their outputs are then summed and inverted. This provides a fully positive signal that we then feed into an integrator circuit. The integrator circuit includes a MOSFET in parallel with the feedback capacitor with a gate voltage supplied by a 4KHz sine wave. This periodically resets the integrator so that we can sample the current level over a set time interval. We feed the inverted output from the integrator into a comparator with a variable reference voltage. By adjusting the potentiometer voltage divider that sets the reference level we can determine the threshold current that will trip the interlock. The comparator output is fed to a latch so that the interlock state will hold once it is tripped. The latch can be reset with a manual switch on the interlock box. The latch output then goes to a Xantech AC1 DC controlled AC outlet that provides the power to the audio amplifier. This outlet has a fast on/off switch that depends on the digital input from the interlock circuit. Thus, if the AC TOP coils enter a failure mode which could cause damage, the interlock outputs a logical low and the Xantech controlled

outlet cuts power to the audio power amplifier that provides current. Power can be restored by flipping the manual reset switch on the interlock box up and down.

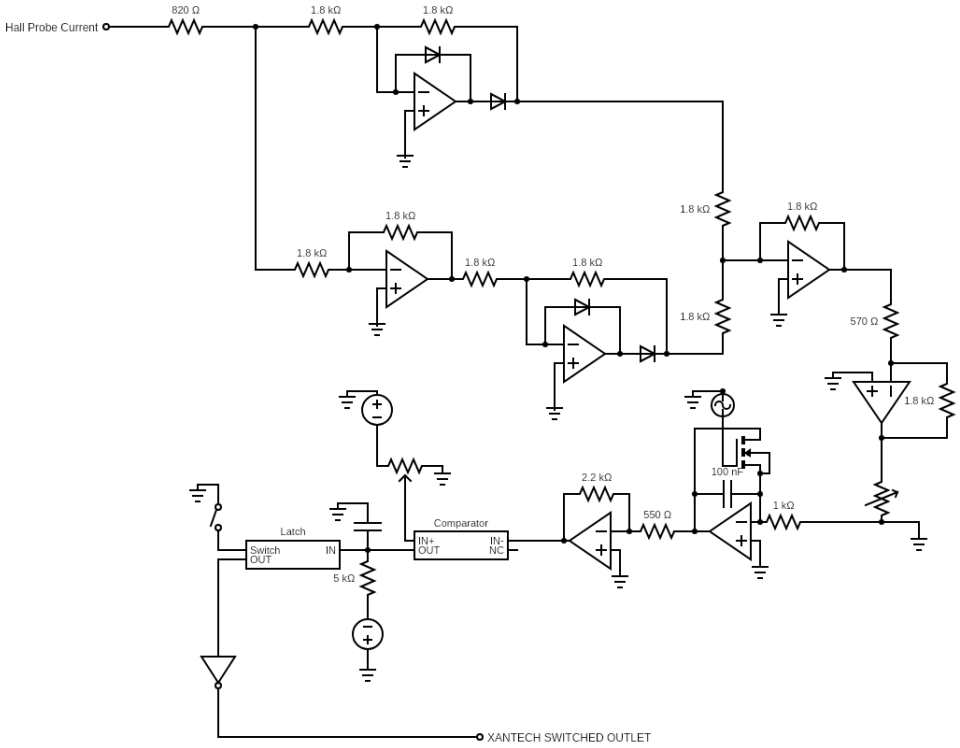

FIGURE 2.4. Circuit diagram for TOP current interlock.

2.5 660 nm Poking Beam

Our experiment in Chapter 3 requires a tuneable and repeatable perturbation of the condensate. To this end we use a 660 nm laser beam as a blue-detuned, repulsive barrier called the *poking beam*. This beam was generated with a Thorlabs L660P120 diode and driven with an Arroyo Instruments 4200DR laser driver. The power of the beam was varied by externally modulating the driver current with an analog ramp provided by the computer. The beam is collimated with a Thorlabs ALT230P-B collimating tube to a $1/e^2$ radius of 2.5 mm and subsequently expanded with a 4:1

Keplerian telescope before being focused onto the BEC with an $f = 500$ mm lens to a $1/e^2$ radius of 22.2 μm. We used this system to achieve a range of irradiances at the BEC from 1.14 $\frac{\text{mW}}{\text{mm}^2}$ to 155.7 $\frac{\text{mW}}{\text{mm}^2}$ for our experiments. As shown in Figure 2.5 the expanded beam is folded along the y axis, propagates through an $f = 500$ mm lens and through a beamsplitter below the magnetic coil assembly to be reflected upwards along the positive z axis and onto the condensate. The poking beam is blocked from the camera by a notch filter with a pass band centered at 780 nm and a full-width-half-max of 2 nm. Ramping this beam on and off allows us to perturb the density of the condensate and couple energy into it. In Figure 2.6 we can see both the beam in the plane of the BEC and an example of a BEC perturbed by the beam.

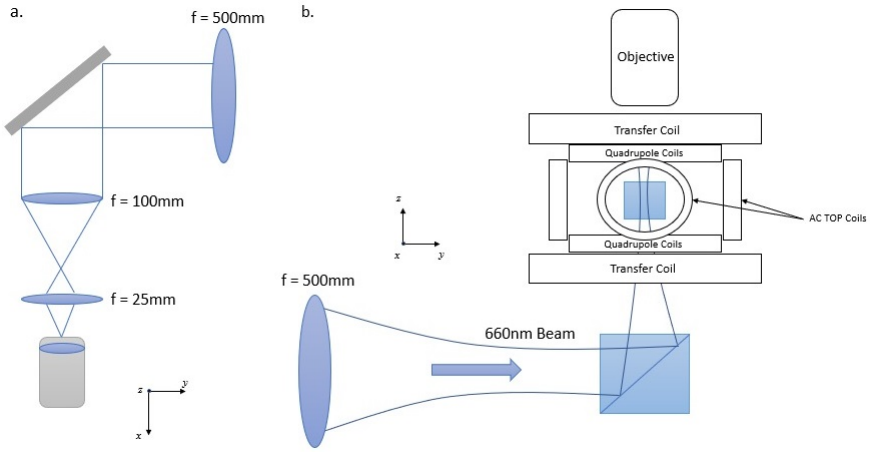

FIGURE 2.5. Optical layout for the 660nm poking beam. a. x-y plane view of the beam optics for collimation, expansion and focusing. b. z-y plane view of the poking beam path into the BEC cell and magnetic coil assembly.

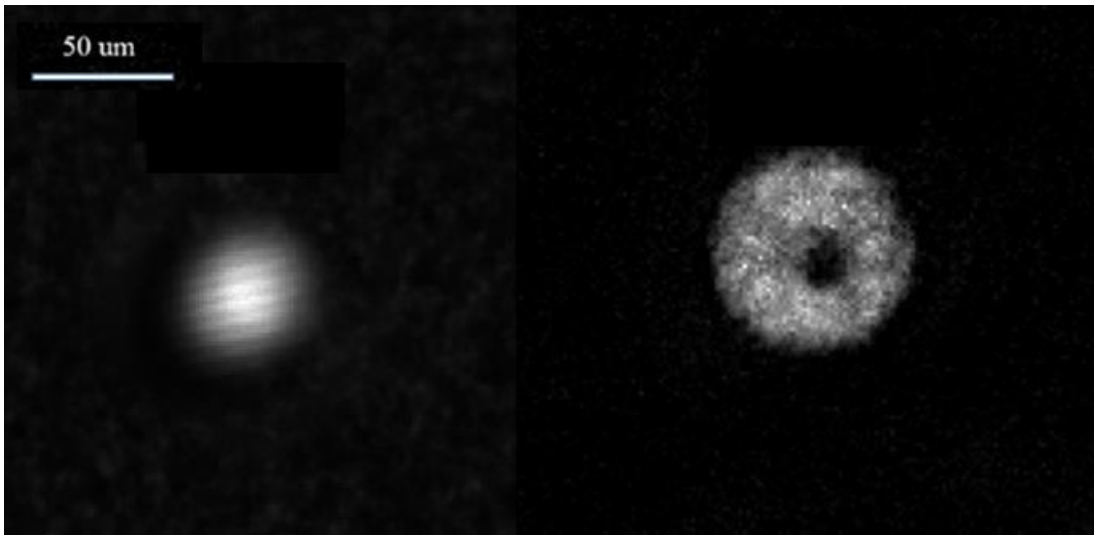

FIGURE 2.6. a. Image of the 660 nm poking beam in the BEC plane with $1/e^2$ radius $w_0 = 22.2$ μm. b. Image of beam on BEC with a peak irradiance of 64 $\frac{\text{mW}}{\text{mm}^2}$.

CHAPTER 3

Relaxation of a BEC in a Spinning TOP Trap

In this section we provide a description of an experimental system in which to study out-of-equilibrium BEC physics as well as a summary of the resulting data. The general idea of the experiment is to examine the relaxation dynamics of a condensate in a rotating trap. We start with a BEC in a TOP trap and ramp on a modulating field as described in Section 2 in order to rotate the trap. If the trap is rotated at a frequency far from any surface wave resonance then no vorticity will be introduced into the BEC and therefore it will remain stationary. However, as also previously discussed in Subsection 1.2.6 the ground state of a condensate in a rotating frame is a vortex lattice containing a number of vortices related to the angular velocity of the trap. Thus, the uniform Thomas-Fermi state is no longer the ground state and must be, at most, metastable. Once the BEC is in the rotating frame we quickly flash on a 660 nm laser beam to form a repulsive barrier. This disturbance introduces energy into the condensate highly exciting it out of its metastable state. After a holding period in the rotating frame the condensate is found to be in a rotating state with a number of quantized vortices. The number of vortices and their arrangement depends on the specific experimental conditions and is a measure of the condensate's equilibration with the trap.

3.1 In-situ Imaging of Vortices

All data in this experiment come from images of condensates without expansion from the trap. The 10X magnification imaging optics we used are detailed by Wilson et al. [9, 10]. We used an absorption imaging modality on the $|F = 2\rangle \rightarrow |F' = 3\rangle$ transition. During the imaging process all trapping fields were snapped off 0.5 ms

before interrogation to avoid spatially dependant Zeeman splitting. The atoms were pumped into the $|F = 2\rangle$ state from $|F = 1\rangle$ with a 30 μs pulse of on-resonance laser light propagating in the negative z-direction. The imaging pulse lasted for another 30 μs during which the repump light was left on so that the atoms would cycle on the $|F = 2\rangle \rightarrow |F' = 3\rangle$ transition to improve the signal. The image pulse detuning ranged over the interval $\Delta = 2\pi \times [-7.38, -10.33]$ MHz.

In order to obtain the resolution needed to image single vortex cores in-situ the system had to be carefully focused. To do so we used generated large vortex lattices using the method of Hodby et al. [11]. Vortex lattices provide excellent targets for focusing as they are highly repeatable, they deform the boundary of the cloud into a hexagonal shape making it easy to detect their presence even outside of the focal plane and they create a highly recognizable, periodic pattern that can be used to qualitatively identify imaging artifacts, and finally they contain vortex cores which are the smallest objects we need to resolve. The timing procedure we used to generate vortex lattices, as seen in Figure 3.1 is almost identical to that we use for the spin and poke experiment in Figure 3.3. The differences are that, in the case where we only spin, imaging is done after the modulating bias field ramps down and there is, of course, no laser pulse.

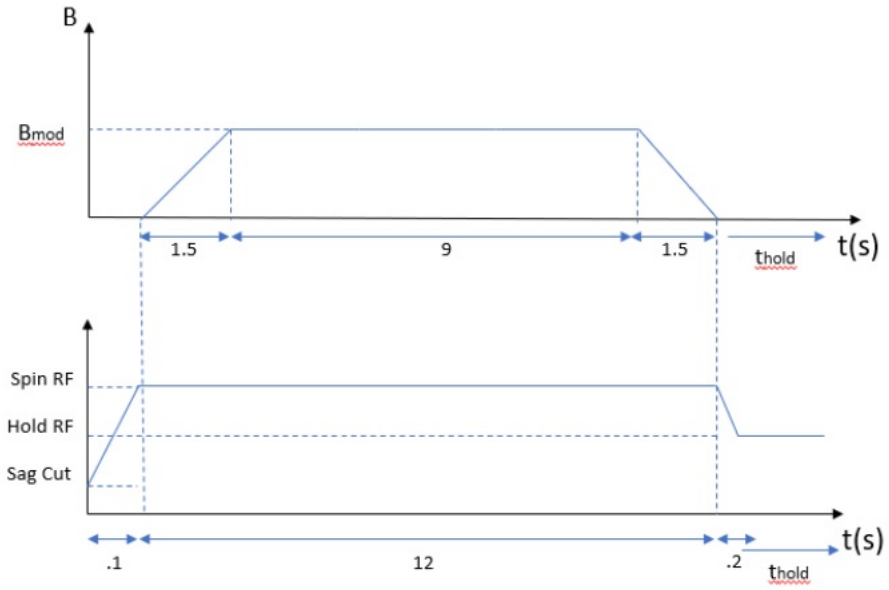

FIGURE 3.1. Timing sequence to generate vortex lattices by rotating the TOP trap. We ramp the modulating bias from zero to its peak over 1.5 s, hold at its peak for 9 s and then ramp off over 1.5 s. The trap is rotated at the surface wave resonance of $\nu_s = 6.25$ Hz. The RF ramps up from the sag cut value of 4.85MHz to 7.5-7.8 MHz before the modulating bias ramps up. It holds at this value for the duration of the spin cycle and quickly ramps down to the holding value (6.55 MHz) after the modulating bias is ramped off. The imaging time is arbitrary but happens after a hold time 6 s.

Using this technique to generate lattices we then manually adjusted the height of the microscope objective until we were able to clearly resolve the constituent vortex cores. Once we found approximate best focus we measured the system magnification to be 9.18. As a final optimization step we made fine adjustments to the relative phase and amplitude of the TOP rotating bias and modulation bias channels to maximize the number of vortices produced by a spin cycle. This served as a highly sensitive measure of the circular symmetry of the TOP trap and the modulating bias. Representative in-situ images of vortex lattices generated using this technique are shown in Figure 3.2.

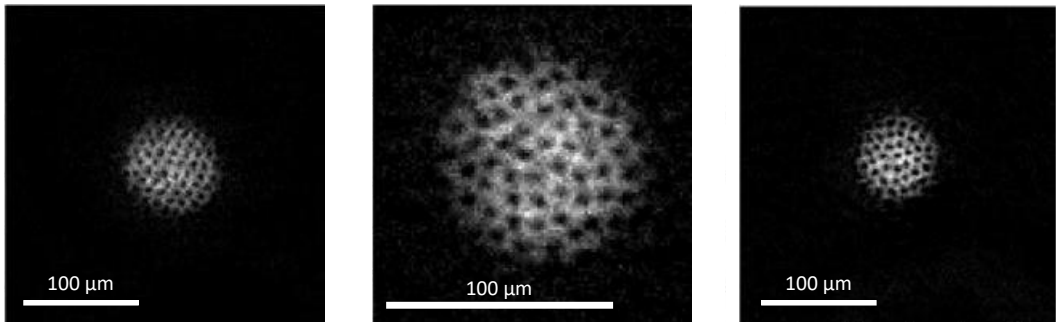

FIGURE 3.2. Some representative in-situ images of vortex lattices generated using the procedure described above.

3.2 Exciting the BEC

The primary experiment performed in the following has three basic parts. All experiments start with a Bose-Einstein condensate with $N \approx 2 \times 10^6$ atoms in a sagged TOP trap with rotating bias $B_0 = 5$ G with rotational frequency $\nu_{TOP} = 4$ KHz and gradient $B'_z = 46.98$ G/cm. This yields trapping frequencies $\omega_{\rho,z} = 2\pi \times (8.9, 17.8)$ Hz where ρ is the transverse coordinate. We then ramp up a second bias waveform, added to the TOP signal rotating at cycle frequency ν_s. This causes the TOP trap to become elliptical and spin about the z-axis with cycle frequency $\nu_{spin} = \frac{|\nu_s - \nu_{TOP}|}{2}$. At peak modulation the magnetic fields along the major and minor ellipse axes are $B_\epsilon = 6.25$ G and $B_0 = 3.5$ G respectively. This yields trapping frequencies $\omega_\epsilon = 2\pi \times 7.96$ Hz and $\omega_0 = 2\pi \times 10.64$ Hz which gives a deformation parameter of $\epsilon = 0.28$. After the modulating bias has fully ramped up we hold for one second before ramping on a 660 nm laser focused on the center of the BEC to a $1/e^2$ radius ≈ 22.2 μm with an 85 mm focal length achromat. This beam is held on for a variable amount of time and then ramped off again. The potential depth of the poking beam varied over the range $U_0 = 2 \times 10^{-33}$ J to 2.7×10^{-31} J. The condensate is held in the rotating trap for several seconds. Before the modulating field is ramped down all magnetic fields are snapped off to avoid detuning due to spatially dependent Zeeman shifts and the BEC

is immediately imaged along the z-axis. A typical experimental sequence is shown in Figure 3.3. Clearly this system creates a large parameter space. In the following we explore this space by adjusting the poke hold time the poke amplitude and the trap rotation frequency and observing the subsequent number of generated vortices. We also study the dynamics of the system during the poking process and relaxation.

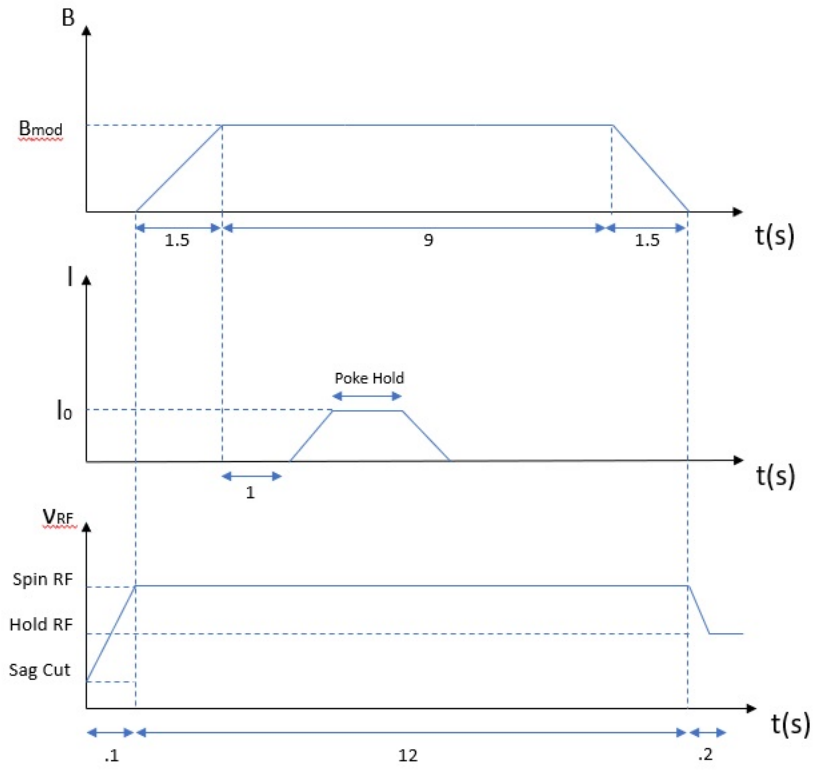

FIGURE 3.3. Timing sequence for the basic experimental template. We ramp the modulating bias from zero to its peak over 1.5 s, hold at its peak for 9 s and then ramp off over 1.5 s. The laser intensity begins to ramp up 2.5 s after the spinning starts. Unless otherwise stated, the ramps are equal in length and generally 0.1 s long while the typical value of the poke hold $\sim$ 0.5 s. The RF ramps up from the sag cut value 4.85 MHz to 7.5-7.8 MHz before the modulating bias is ramped on. It holds at this value for the duration of the spin cycle and quickly ramps down to the holding value 6.55 MHz after the modulating bias is ramped off. The imaging time is arbitrary but happens before ramp down so that the condensate remains in the rotating frame.

3.3 Experimental Results

We performed a variety of experiments to characterize the behaviour of the condensate subject to the previously described conditions. Once we were certain our sequence was generating vortices we obtained a series of images examining the cloud dynamics through the poking process both with and without a rotating trap. In the case where the trap was spinning we observed a distortion of the cloud where it expanded, became asymmetric and appeared to rotate. A series of images demonstrating poking dynamics is shown in Figure 3.4.

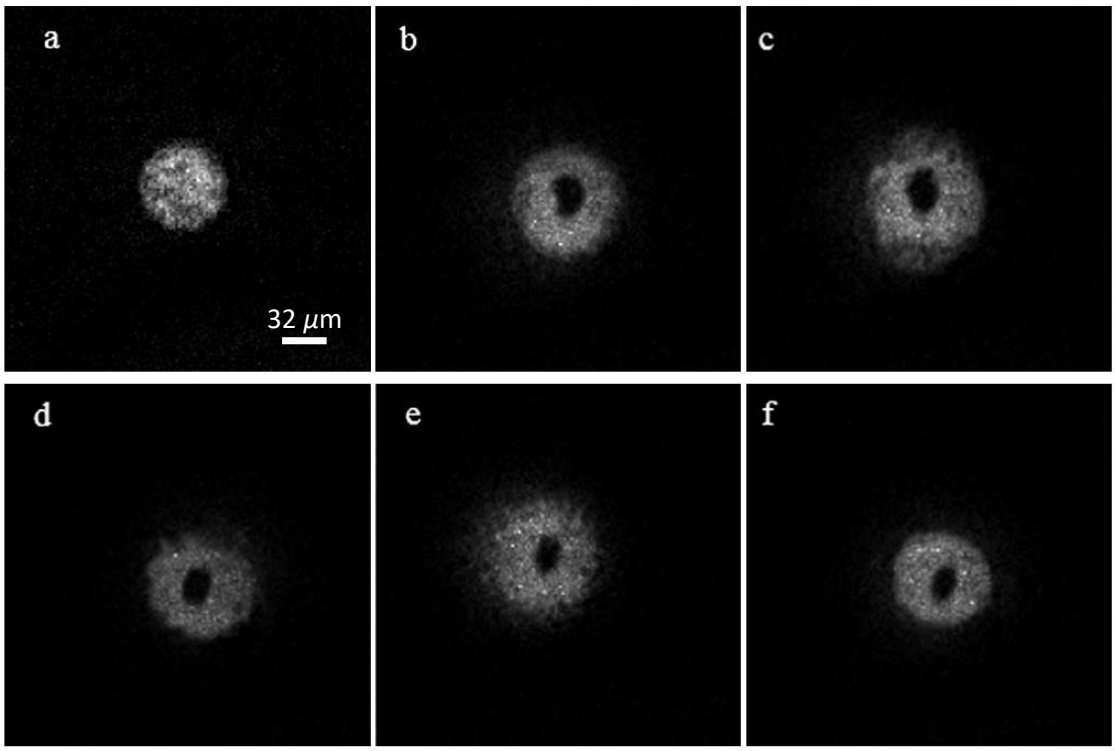

FIGURE 3.4. Images of different condensates at various times during the poke without the trap spinning. There is a 100 ms ramp up process and then each image corresponds to a time during the poke hold which lasted a total of 500 ms. **a.** The condensate before poking **b.** 50 ms of poke hold **c.** 100 ms into poke hold **d.** 150 ms of poke hold **e.** 250 ms of poke hold **f.** 500 ms of poke hold. All images were taken for a peak irradiance of 41 $\frac{\text{mW}}{\text{mm}^2}$.

During the poking process the initial distribution expands about the beam and contracts in a damped, periodic manner. The period of this oscillation calculated from these images $T_{osc} \approx 100$ ms is approximately equal to the radial trap period $T_{trap} = 1/8.9 = 112$ ms as expected. The cloud maintains a generally circular symmetry and no vortices or solitons are observed. The periodic expansion of the cloud then is due to the coupling of acoustic energy from to poking beam into the condensate. In contrast, Figure 3.5 shows the condensate dynamics during the poking process in a rotating trap.

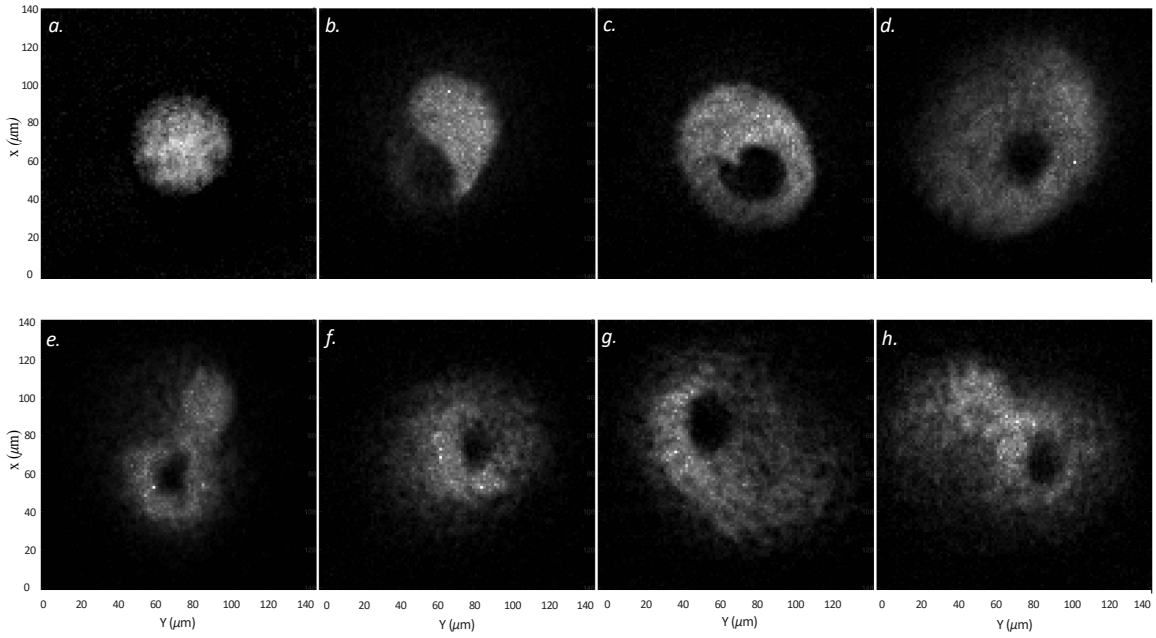

FIGURE 3.5. Images of the condensate at different times during the poke and spin process. There is a 100 ms ramp up process and then each image corresponds to a time during the poke hold which lasted a total of 500 ms. **a.** The condensate before poking **b.** 20 ms of poke hold **c.** 50 ms into poke hold **d.** 150 ms of poke hold **e.** 300 ms of poke hold **f.** 350 ms of poke hold **g.** 400 ms of poke hold **h.** 500 ms of poke hold. All images were taken for a peak irradiance of 41 $\frac{\text{mW}}{\text{mm}^2}$ and $\nu_{spin} = 12$ Hz.

The initial condensate distribution in the rotating trap is an approximately uniform Thomas-Fermi distribution. Under the influence of the poking beam the cloud

again, expands and contracts but as it expands it loses its circular symmetry and appears to rotate. There are no vortices evident in this series of images. We performed a similar set of measurements to capture the dynamics of the condensate after the poke. The conditions under which this experiment was performed produce few vortices $N_{vort} \sim 2 - 4$.

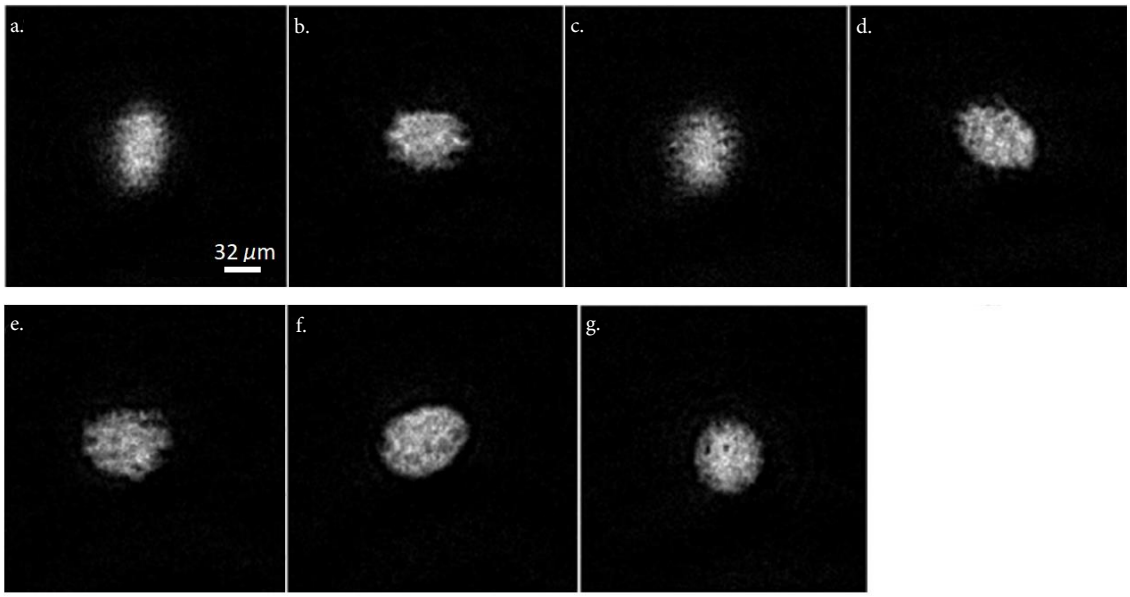

FIGURE 3.6. Images of the condensate at different times after the poke with the trap spinning. **a.** .1s of hold **b.** .25 s of hold **c.** .5 s of hold **d.** 1 s of hold **e.** 2 s of hold **f.** 4 s of hold **g.** 6 s of hold. All images were taken for a peak irradiance of 18 $\frac{\text{mW}}{\text{mm}^2}$ and $\nu_{spin} = 4.5$ Hz.

In Figure 3.6 the condensate is spinning in the rotating trap with an elliptical symmetry. In the absence of a poking perturbation the cloud would remain stationary with a circular symmetry as shown in Figure 3.5a. Small numbers of vortices can be seen forming at the boundary of the cloud and after six seconds of relaxation we see a circular condensate with two vortices.

A variety of different vortex distributions from vortex pairs to larger lattices can

be obtained by varying the experimental parameters. Figure 3.7 displays a range of vortex distributions generated using this method.

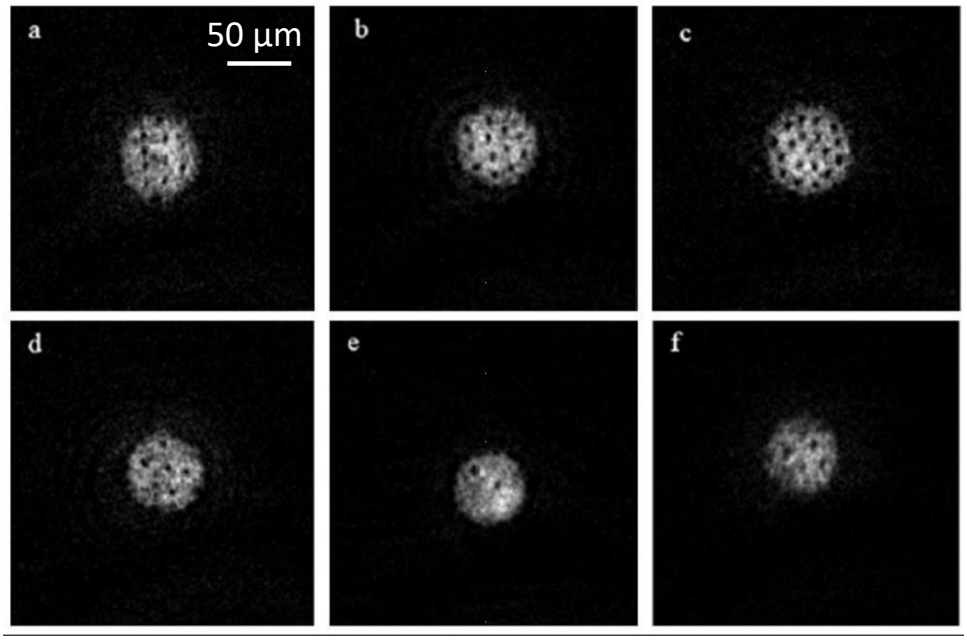

FIGURE 3.7. Images of different vortex distributions. **a.** ν_{spin} = 5Hz, Sag Cut = 4.85 MHz, Spin RF = 7.72 MHz, Peak Irradiance = 29.5 $\frac{\text{mW}}{\text{mm}^2}$ **b.** ν_{spin} = 11.5Hz, Sag Cut = 4.86 MHz, Spin RF = 7.5 MHz, Peak Irradiance = $18mW/mm^2$ **c.** ν_{spin} = 22.5Hz, Sag Cut = 4.85 MHz, Spin RF = 7.72 MHz, Peak Irradiance = 29.5 $\frac{\text{mW}}{\text{mm}^2}$ **d.** ν_{spin} = 10Hz, Sag Cut = 4.85 MHz, Spin RF = 7.72 MHz, Peak Irradiance = 29.5 $\frac{\text{mW}}{\text{mm}^2}$ **e.** ν_{spin} = 4.5Hz, Sag Cut = 4.86 MHz, Spin RF = 7.5 MHz, Peak Irradiance = 18 $\frac{\text{mW}}{\text{mm}^2}$ **f.** ν_{spin} = 5Hz, Sag Cut = 4.86 MHz, Spin RF = 7.5 MHz, Peak Irradiance = 18 $\frac{\text{mW}}{\text{mm}^2}$.

To understand how our experimental parameter space effects the dynamics of the system we aggregated a number of experimental runs with different settings and recorded the number of vortices generated. We estimated the error of each data point as the Poissonian mean of the average number of vortices observed divided by the square-root of the number of measurements averaged:

$$Error = \pm \frac{\sqrt{\langle N_{Vortices} \rangle}}{\sqrt{N_{measurements}}}. \tag{3.3.1}$$

Figure 3.8 displays data gathered from a set of experimental runs in which the peak irradiance of the poking beam was varied while the other experimental parameters remained fixed.

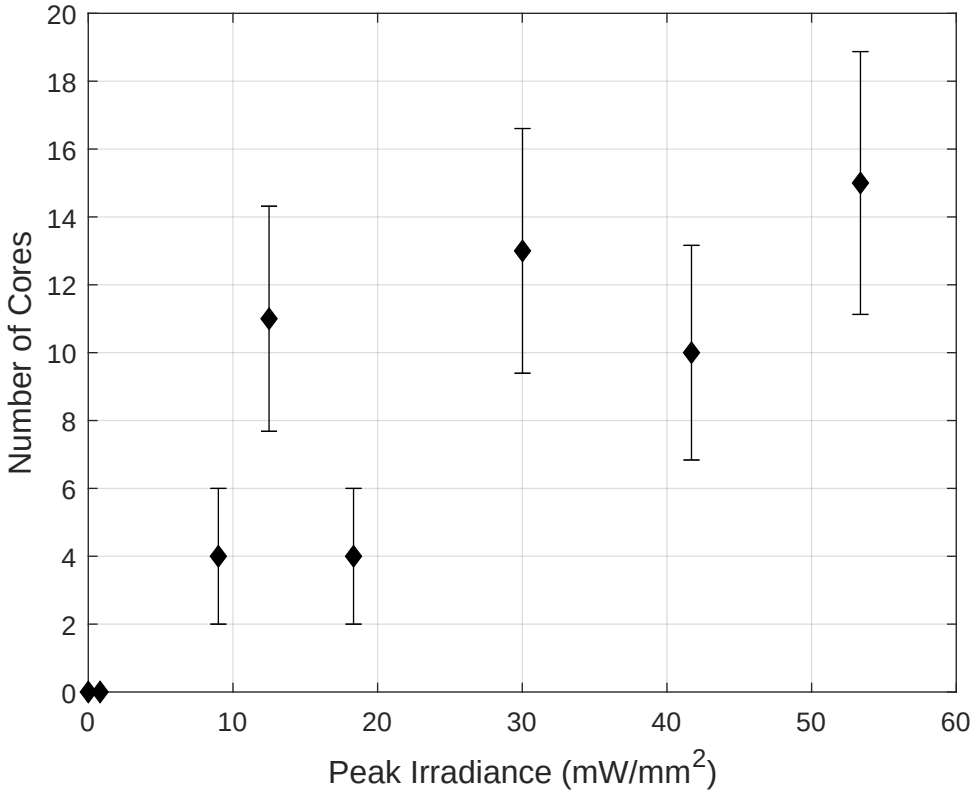

FIGURE 3.8. Average number of vortex cores observed versus the peak irradiance of the poking beam. For these measurements we fixed ν_{spin} = 12 Hz, Poke Hold = 500 ms, Sag Cut = 4.85 MHz and Spin RF = 7.55 MHz.

We found that for fixed conditions, there was a definite upward trend in the number of vortices with increasing peak poking irradiance. This makes intuitive sense as a high poking power would couple the condensate to more highly excited trap modes, making it more likely to relax from its metastable, non-rotating state

to a many-vortex state. We also found that an off-center poking beam behaved identically to a centered one.

A possible false-positive vortex generation mechanism would be the BEC rotating about an elliptical obstacle and we wanted to determine whether the vorticity was generated in this manner as opposed to a perturbation of the fluid decaying in the rotating frame. We hypothesized the if the vortices were generated due to flow then the number of cores should increase with the amount of time the obstacle remains in the rotating trap. To test this we varied the poke hold time from 0.01 ms - 800 ms as displayed in Figure 3.9.

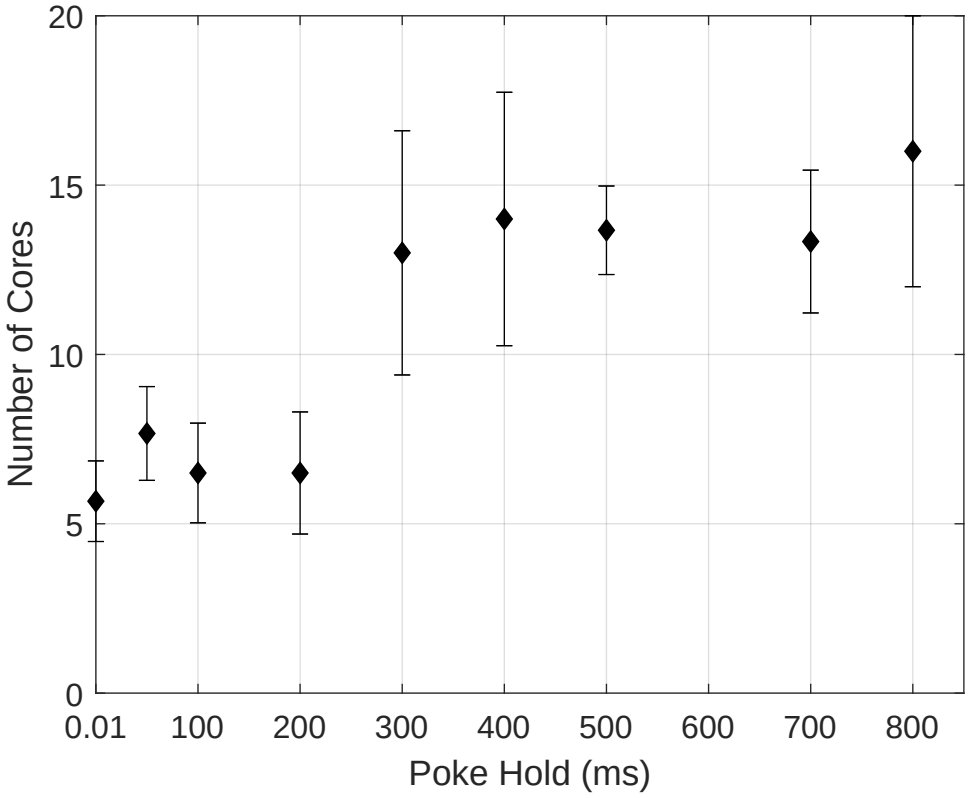

FIGURE 3.9. Average number of vortex cores observed versus the time we hold the 660 nm beam at peak irradiance with ramp up and down times of 100 ms. The trap spinning frequency for all points was $\nu_{spin} = 22.5$ Hz, the number of vortex cores is averaged over Spin RF frequencies ranging from 7.6 - 7.72 MHz and Peak Irradiances from 18.3 - 158.5 $\frac{\text{mW}}{\text{mm}^2}$.

We found that there was little, if any, dependence of the number of cores observed on the poke hold time over the range investigated. There seemed to be a lower bound at which the number of observed cores decreased that we expect corresponds to a time scale at which the fluid has not fully responded to the perturbing potential.

Generally we found that the dependence of vortex number on ν_{spin} was weak. There were two regions that were exceptions, below $\nu_{spin} \approx 4.5$ Hz where we did not observe any generated vortices (we suspect this corresponds to a critical angular

velocity below which vortices are not favorable) and in the vicinity of $\nu_{spin} = 8$ Hz $\approx \frac{\omega_\rho}{2\pi}$, where the condensate is destroyed due to a resonance with the TOP trap. We also avoid the vicinity of the surface wave resonance at $\nu_{spin} = 6.25$ Hz since we can not differentiate between vortices generated via the different excitation methods. Except near the regions addressed previously, the number of vortex cores does not seem to follow a strictly upwards trend with the trap spinning frequency nor does it seem to exhibit signs of a resonance.

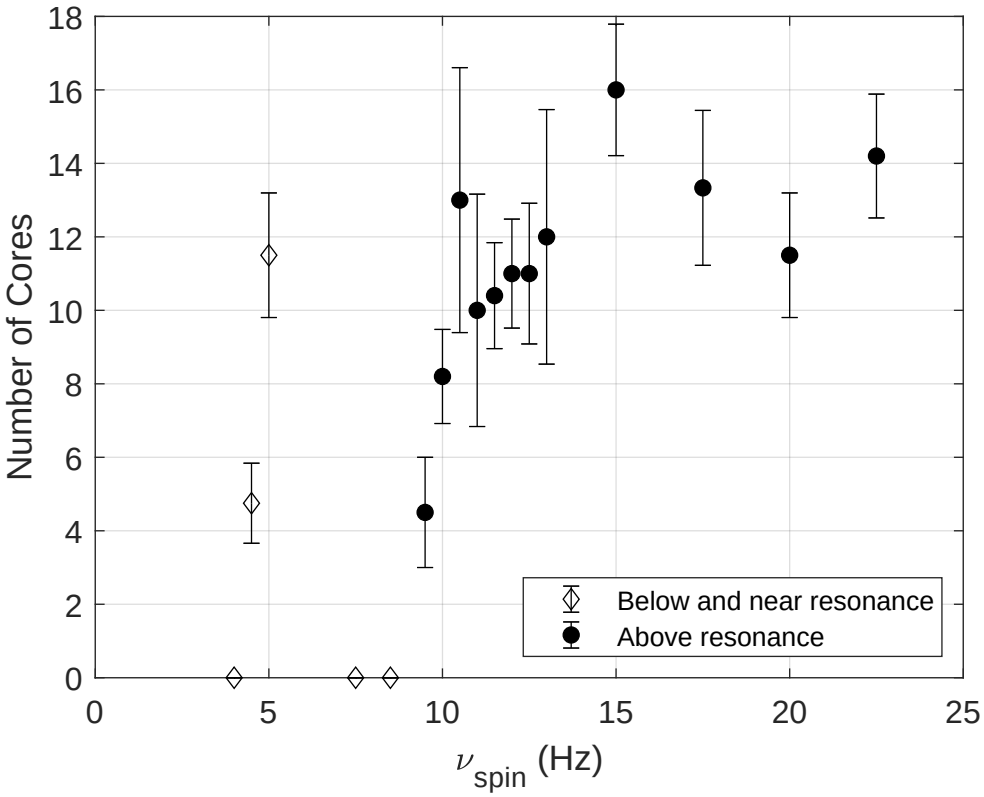

FIGURE 3.10. Average number of vortex cores observed versus the trap spinning frequency. The open diamonds represent data points below or near the trap resonance while the filled circles represent points above resonance. Data points are averaged over many different experimental conditions. The number of averaged points varies from one to five.

3.4 Conclusions and Future Measurements

We have presented the first set of experimental data describing the relaxation of a BEC perturbed by a laser pulse in an elliptical TOP trap rotating at frequencies higher than the trapping frequencies. From the data in the previous section it appears that vortices are indeed generated by the relaxation of the BEC in the rotating trap. Since we did not find an increase in the number of vortices generated with increased poking time we can rule out vortex generation due to fluid flow about a boundary. Because we observed that vortices were nucleated at the boundary of the cloud rather than inside the condensate we can also determine that vortex generation is not due to the poke itself. In addition, we found that the condensate would relax into a vortex-state regardless of the trap rotational frequency so long as it was greater than $\nu_{spin} = 4.5$ Hz. This lower bound could be interpreted as the lower critical angular velocity discussed in Sub-Section 1.2.6. The only strong trend in vortex number that we found was with increasing peak poking irradiance which determined the perturbation amplitude. We suspect that the relaxation dynamics are temperature dependent. That is, the condensate reaches the ground state of the rotating trap via interactions with the presumably rotating thermal atoms. Future measurements might probe the effects of varying the Spin RF as well as the temperature of the initial atom cloud which is controlled by the Sag Cut. In addition, it would be worthwhile to explore how the number of vortices generated varies with the trap deformation parameter as all data presented here was collected for a single trap ellipticity. We hope that the data provided by this experimental platform will seed theoretical interests. Namely that it will provide insight into stochastic GPE models for finite-temperature matter waves that include interactions with the thermal fraction.

CHAPTER 4

The Classical Shack-Hartmann Wavefront Sensor

As we have discussed in previous sections, a major hurdle to overcome in BEC 2D quantum turbulence is the measurement of a kinetic energy spectrum and detection of vorticity, particularly the in-situ positions and dynamics of vortices and their directions of circulation. In this dissertation we present an atom-optical analogue to the Shack-Hartmann Wavefront Sensor (SHWS), a device commonly used in astronomical and ophthalmic optics to reconstruct the phase distribution of an optical field at the plane of the sensor, called the *phase map*, from discrete measurements of the local phase gradient, called the *wavefront slope*. We propose our Atom-Optical Shack-Hartmann Wavefront Sensor (AOSHWS) as a realistic technique that will facilitate these valuable measurements. To motivate this and provide intuition for the simulations in Chapter 6 we give a brief overview here of the theory of Shack-Hartman Wavefront Sensors and extraction of slope information.

4.1 Introduction to the SHWS

The classical Shack-Hartmann Wavefront Sensor (SHWS) was first described in a conference abstract by Platt and Shack in 1971 [44, 45] as a device to characterize aberrations in optical imaging systems for low-light environments. Since its inception it has become a workhorse in the field of wavefront sensing. It consists of a square, 2D grid of small lenslets of focal length f, center-to-center separation p. Other geometries, such as hexagonal, are sometimes used but we will not consider them here. As shown in Figure 4.1, a plane wave propagating parallel to the SHWS optical axis will be focused to a grid of spots observed one focal length from the plane of the lenslets,

the position of each spot lying on the optical axis of the lenslet. If a patch of the wave front is distorted then the spot corresponding to the lenslet in this region will be shifted perpendicular to its optical axis by a distance *d*. we define the center locations of the lenses to be at (x_i, y_j), where i and j are integers defined over the ranges $1, 2..., N$ and $1, 2..., M$ respectively. By measuring the displacements of the spots yielded by a distorted wavefront from their neutral position in the plane of detection we may calculate the local wavefront slope at each lenslet as

$$s_{i,j}^{x,y} = d_{i,j}^{x,y}/f. \tag{4.1.1}$$

Here, $s_{i,j}^{x,y}$ is a 2 by 1 column vector that contains the spot displacements in the x and y directions for the lenslet located at point (x_i, y_j). The wave front slope is equivalent to what is called the *transverse ray error* in optical aberration theory and is related to the *wavefront error* according to

$$s_x(x_i, y_j) = -\frac{2f}{D}\frac{\partial}{\partial x}W(x_i, y_j) \tag{4.1.2}$$

$$s_y(x_i, y_j) = -\frac{2f}{D}\frac{\partial}{\partial y}W(x_i, y_j) \tag{4.1.3}$$

where D is the illuminated diameter of the grid and W is the wavefront error defined as the optical path difference between the incident wave and an ideal reference wave [46].

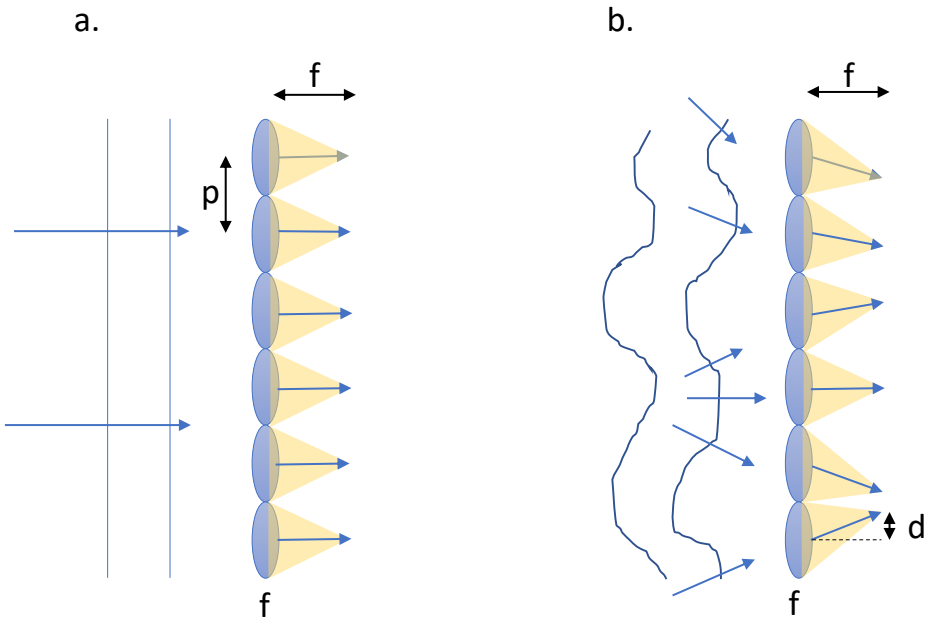

FIGURE 4.1. Visual representation of the operation of a classical Shack-Hartmann Wavefront Sensor. a. Incident plane wave propagating along optical axis. b. Distorted wavefront.

The spatial arrangement of these points of irradiance in the detection plane is called the *Hartmanngram*. Once the slope data have been calculated from the Hartmanngram the phase may be estimated by solving the fundamental equation of the SHWS:

$$s = A\phi \tag{4.1.4}$$

where A is a continuous to discrete operator called the *geometry matrix* that relates the phase map ϕ to the $N \times M \times 2$ slope data matrix s composed of the elements $s_{i,j}^{x,y}$. There are a number of methods to invert the geometry matrix to reconstruct the phase [47]. Here we will only consider the common case of calculating a least-squares fit by the pseudo-inverse of A, called the *reconstructor*, and decomposing the data onto a basis of Zernike polynomials. However, for the purposes of the measurement we wish to propose, these methods are unnecessary as we only need the slope data.

4.2 Wave Optical Theory of the SHWS

The previous description of the SHWS is the most common and intuitive model based on geometrical optics. The corresponding wave optics picture is one where the incident wavefront is broken up by the SHWS and the area covered by each lenslet sub-aperture is sufficiently small so that the wavefront is approximately plane. The Hartmanngram is then the sum of $N \times M$ tilted plane waves. However, it assumes that the sub-wavefront from each lenslet is independent from another which is valid only in the case of low F/#. For many operating conditions this may be unrealistic so we develop a short wave optical treatment of the SHWS following Primot [48].

Since we are observing the field at the back focal plane of the lenslets we may treat the propagation with Fraunhoffer diffraction theory. The phase grating of the SHWS is given by the function

$$\begin{aligned}\Gamma(x,y) &= \left[\exp i\pi\frac{(x^2+y^2)}{\lambda f}\mathrm{rect}_{p,p}(x,y)\right] * \mathrm{comb}_{p,p}(x,y) \\ &= \gamma(x,y) * \mathrm{comb}_{p,p}(x,y).\end{aligned} \tag{4.2.1}$$

The function $\gamma(x,y)$ is the spatial phase shift imprinted by a single lenslet, $\mathrm{rect}_{p,p}(x,y)$ is a function defined as unity over the support $-p/2 < x < p/2, -p/2 < y < p/2$ and zero elsewhere, $\mathrm{comb}_{p,p}(x,y) = \sum_{n=0}^{N}\sum_{m=0}^{M}\delta(x-np, y-mp)$ where $\delta(x,y)$ is the 2D Dirac delta function and $*$ denotes convolution. Since $\Gamma(x,y)$ is periodic in both arguments we can write it as a Fourier series:

$$\Gamma(x,y) = \frac{1}{p^2}\sum_{n=-\infty}^{\infty}\sum_{m=-\infty}^{\infty} c_{n,m}\exp\left[\frac{2i\pi}{p}(nx+my)\right]. \tag{4.2.2}$$

The $c_{n,m}$ characterize the SHWS and may be calculated in the usual way.

$$\begin{aligned}c_{n,m} &= \langle e^{\frac{2i\pi}{p}(nx+my)}|\gamma(x,y)\rangle \\ &= FT\left[\gamma(x,y)\right]_{u=n/p,v=m/p} \\ &\equiv \Xi(u=\frac{n}{p},\, v=\frac{m}{p})\end{aligned} \tag{4.2.3}$$

where FT denotes the Fourier transform operator. Evaluating the Fourier transform in Equation 4.2.3 for an arbitrary point we get the relation:

$$\Xi(u,v) = [\mathrm{sinc}(\pi p u)\mathrm{sinc}(\pi p v)] * \exp\left[i\pi\lambda f(u^2+v^2)\right] \tag{4.2.4}$$

which is the point spread function for a thin lens with square edges. The character of the irradiance distribution in the observation plane will then depend on the width and rate of variation of this function which is determined by variables p, f and the dimensions of the SHWS grid. Having determined the Fourier properties of the phase grating, the amplitude of the electric field at the focal plane may be calculated using standard, integral methods. Primot identifies two regimes associated with this treatment: the *independence regime* and the *cross-talk regime* [48]. The independence regime occurs in the limit of small F-numbers and yields an irradiance distribution which is the sum of tilted replicas of the input wavefront. This regime mimics the behavior described in Platt and Shack's original paper; laterally translated spots independent from neighboring sub-wavefronts. The cross-talk regime occurs at larger F-numbers and can display a variety of behaviors depending on the specific conditions.

4.3 Detecting Vorticity from Linear Wavefront Slope Data

Once wavefront slope or vorticity data has been collected we are particularly interested in locating vortices and identifying their circulation. There are several methods to do so as discussed by Murphy and Dainty [49] however, we will only discuss one. The vortex potential method of E.O. Le Bigot and W.J. Wild [50, 51] is straightforward in implementation, robust to noise and computationally fast. The approach of this method is to convert the discrete velocity field, s into a continuous scalar field, h, called the *vortex potential field*, whose amplitude corresponds to the local circulation and diverges logarithmically at the location of vortex singularities. These extrema are positive or negative depending on vortex circulation direction and have high con-

trast with the background potential. This contrast can increased by raising h to an arbitrary power. We provide a derivation for h in the remainder of this section.

The conceptual core of the problem is to rotate the components of s to turn a calculation of curl into one of divergence as shown in Figure 4.2 .

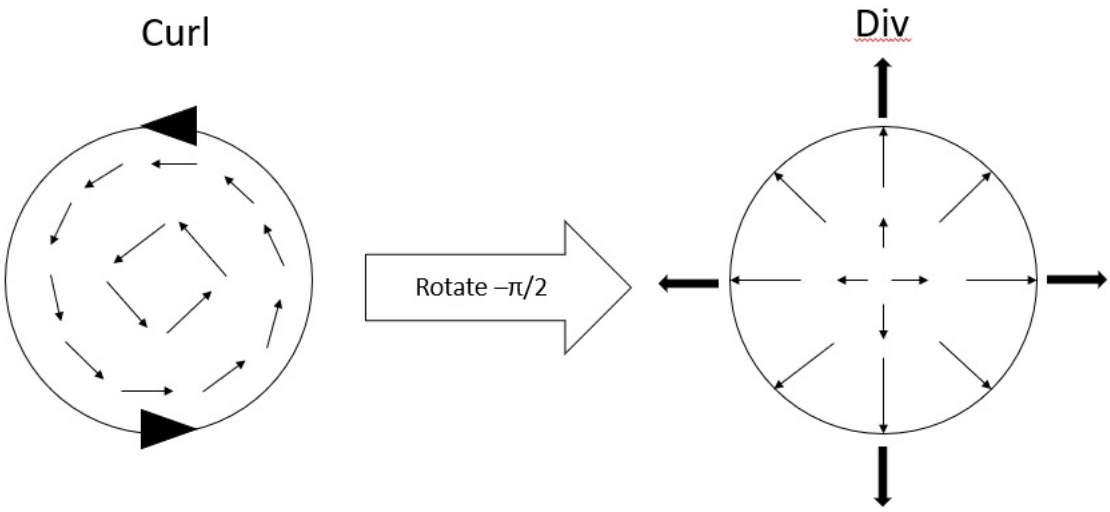

FIGURE 4.2. In 2D the problem of calculating the curl of a vector field becomes equivalent to calculating its divergence if each component is rotated by $-\pi/2$.

This comes from the fact that in 2D

$$\boldsymbol{\nabla} \cdot (R_{-\pi/2}\boldsymbol{s}) = (\boldsymbol{\nabla} \times \boldsymbol{s}) \cdot \hat{z} \tag{4.3.1}$$

where R_θ is a rotation by angle θ and we define $s' = R_{\pi/2}s$ as the gradient of a scalar potential function h like

$$\nabla h \equiv \boldsymbol{s'}. \tag{4.3.2}$$

Thus, regions of non-zero divergence in s' will yield extrema in h. Since this equation has no exact solution we construct a pseudo inverse by finding a solution that minimizes the L2 norm.

$$\int_S d^2\boldsymbol{x} |\nabla h(\boldsymbol{x}) - \boldsymbol{s'}(\boldsymbol{x})|^2 \tag{4.3.3}$$

To do this use switch to the Fourier domain using Parseval's theorem and the minimizing solution turns out to be the projection of the Fourier transform of s' along each of its Fourier components

$$\tilde{h}^{sol}_{\boldsymbol{k}} = -i\frac{\boldsymbol{k}\cdot\tilde{\boldsymbol{s}'}_{\boldsymbol{k}}}{|\boldsymbol{k}|^2} \tag{4.3.4}$$

where a tilde denotes the Fourier transform of the corresponding field and h^{sol} is optimal solution for the vortex potential field. We set $\tilde{\boldsymbol{s}'}_{\boldsymbol{k}=0} = 0$, this is essentially the gradient pseudo inverse. Branch points in phase then show up in the vortex potential as $h(\boldsymbol{r}) = \pm 2\pi \log(|\boldsymbol{r}|)$.

To implement this in a matrix form we introduce the *geometry matrix* A. The geometry matrix relates the wave front phase to the slope data and is determined through analysis of the system. We calculate the pseudo inverse like

$$A^{+} = \lim_{m\to 0}(A^{\dagger}A + m^2 I)^{-1}A^{\dagger}. \tag{4.3.5}$$

Here m is a small number that prevents the inverted matrix from being singular and I is the identity matrix. We can then calculate the vortex potential matrix

$$h = A^{+}R_{\pi/2}\boldsymbol{s}. \tag{4.3.6}$$

Thus, once the slope data has been acquired we can completely characterize the vorticity of the condensate with a single matrix multiplication.

It is important to clarify that the method of Le Bigot and Wild, as described here, does not work for a non-linear field. Finding the pseudo-inverse of the geometry matrix assumes that the phase can be reconstructed as a linear combination of components of the singular vector basis. Since the condensate is non-linear this is not feasible. For the purposes of this thesis it is not necessary to reconstruct the phase as we only require the wavefront slope to locate vortices and determine their handedness. We provide this discussion only for comparison with the method of vortex identification we will describe later for a non-linear field.

CHAPTER 5

The Atom-Optical Shack-Hartmann Wavefront Sensor

Since the velocity field of a BEC is proportional to the gradient of its phase, a measurement analogous to the SHWS seems of great interest. The problem then is how to create the equivalent of a grid of lenslets for a matter wave. This problem is straight forward experimentally as a large body of work on the center-of-mass manipulation of neutral atoms with off-resonance lasers via the dipole force has been developed over the past few decades. In particular there is preceding body of work in the focusing of atomic beams in this manner. In 1978 Bjorkholm et al. focused a beam of neutral sodium atoms using a co-propagating red-detuned $TEM_{0,0}$ laser beam [52]. The limitations of this technique due to spontaneous emission were discussed in a 1980 paper [53] and they were able to achieve an atomic beam spot size of 28 μm. Balykin and Letokhov in 1988 proposed using a blue-detuned $TEM_{0,1}$ Laguerre-Gaussian laser beam as a thin lens focusing potential to guide the atoms through a low-irradiance region so that the effects of spontaneous emission would be reduced and Angstrom-scale spot sizes would be achievable [54]. Gould and Gallatin expanded on this concept in 1991 by developing a matter wave diffraction integral that allowed a thick lens treatment of the problem [55]. Though this kind of focusing was not achieved, Sleator et al. demonstrated focusing of Helium atomic beams experimentally using a large period standing wave of light in 1992 [56]. Standing wave atom focusing was further demonstrated in following experiments by Timp et al. in Sodium [57] and by McClelland et al. in Chromium [58]. McClelland provided a theoretical treatment of this technique in 1995 [59]. These works are limited to atomic beams, not BECs and use lattice periods that are large compared to the thermal de Broglie wavelength of the

atoms. They therefore make an assumption not appropriate to this work: that the potential varies in space slowly compared to the DeBroglie wavelength of the atoms. In addition, much of the aforementioned work uses a thick-lens treatment in which timescales of atomic motion are comparable to the length of the laser pulse. Cohen et al. theoretically studied standing wave thin lens fields for cold atoms in 1999 and were able to extract approximate analytic formulas for lens parameters such as focal length and the influence of aberrations [60]. It is on this body of work that we base our proposed Atom-Optical Shack-Hartmann Wavefront Sensor.

The AOSHWS consists of a far-detuned laser beam periodic in two dimensions in the plane of a trapped, quasi-2D BEC as shown in Figure 5.1. This potential is flashed on for a time τ short in comparison with the timescale of BEC fluid dynamics and the two-photon recoil time $t_q = 4\pi m/\hbar^2 q^2 = 2\pi\omega_q^{-1}$ where $k = q/2$ is the lattice wave number. This ensures that the condensate is not modulated during the interaction and that the matter wave is subject purely to phase modulation. The phase curvature imprinted on the atom cloud by the potential causes the BEC to split into contracting sub-condensates. During a given focus time t_f the sub-condensates follow a center-of-mass trajectory that depends on the slope of phase of the bulk condensate at the time of measurement. After this focus time, the atomic distribution is imaged, the location of the sub-condensate peaks are recorded and the slope data are calculated. This measurement gives the gradient of the condensate phase and thus an approximated velocity field of the bulk condensate. For a given sub-condensate we can calculate the velocity like

$$s_{i,j}^{x,y} = \boldsymbol{v}(x_i, y_j) = \left(\frac{\Delta x_i}{t_f}, \frac{\Delta y_i}{t_f}\right) \tag{5.0.1}$$

where (x_i, y_j) are the locations of the lattice sites and i and j are integers defined over the ranges $1, 2, ..., N$ and $1, 2..., M$ respectively. From this we can possibly determine the kinetic energy spectrum, use processing algorithms discussed later to locate and characterize vorticity or even reconstruct the full phase and density profile of the

condensate.

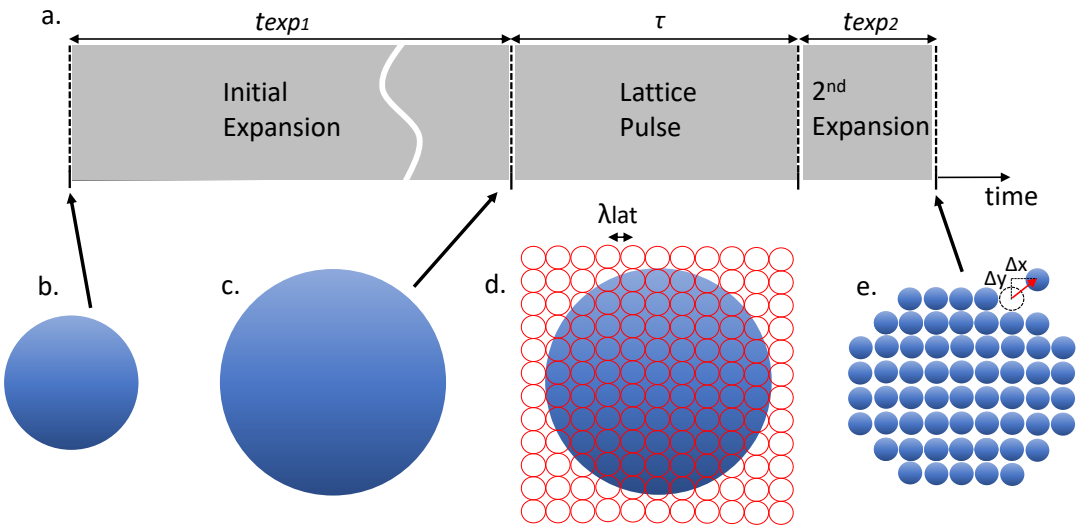

FIGURE 5.1. Visual representation of the AOSHWS measurement process at different times. **a.** Timing sequence. **b.** Initial BEC density distribution. **c.** BEC density distribution after initial expansion period. **d.** Lattice field superimposed onto expanded BEC density distribution. **e.** Focused BEC density distribution after 2nd expansion time demonstrating peak displacement.

Ideally the irradiance gradient would have quadratic curvature similar to the lenses in the SHWS. In principle such fields could be generated using holographic methods like computer generated holograms or spatial light modulators but these methods are expensive, not readily accessible and possibly subject to errors that a lattice is not. Instead we propose to use a 2D optical lattice to break up the BEC at the nodes or anti-nodes of potential depending on whether the laser is red or blue detuned, respectively. This technique has the advantage of requiring only a laser, an acousto-optic modulator and a few focusing optics and mirrors to implement. In addition, by tuning the angle of the interfering beams we can continuously tune the sampling resolution to a lower bound of half of the laser wavelength. This allows us to easily attain a sampling rate on the order of the Nyquist frequency where $f_{Nyquist} \approx \xi/2 \sim 0.5\ \mu$m for quantum vortex cores in BECs.

The main difference between the focusing properties of the standing-wave and quadratic potentials is in aberration of the spots. Since a quadratic lens is free of spherical aberration using a sinusoidal curvature will have a larger spot size at focus. However, we are not concerned with imaging so this does not pose a serious issue to us. It would be useful to calculate an approximate focusing timescale and other imaging parameters for a given set of experimental conditions. To do so we follow the treatment of Cohen et al. [60] and consider the problem in one spatial dimensional. We consider the *thin lens* regime in which the atomic motion will be negligible during the interaction. With this in mind as well as the fact that the sub-condensates will have small numbers of atoms we will neglect non-linearity in our dynamics. Since the condensate will remain axially trapped during the process dynamics are considered in the time domain.

Consider a standing wave laser field along the x direction

$$\boldsymbol{E}(x,t) = \boldsymbol{E}e^{-i\Omega t}g(t)\cos(kx) + c.c. \tag{5.0.2}$$

where $g(t)$ is an envelope function centered at t = 0 with a peak value of unity and width τ and $k = q/2 = 2\pi/\lambda$ is the propagation wave number. All of the simulations in Chapter 6 use a square pulse envelope, however, the treatment here is general. The optical field interacts with a two-level atom with mass m and transition frequency ω. We assume a large detuning Δ and a short interaction time relative to the Rabi frequency χ and spontaneous emission times such that $\Delta = \Omega - \omega \gg 2|\chi|$ and $2\Gamma\tau|\chi|^2/\Delta^2 \ll 1$. This give a pure phase modulation and after adiabatic elimination of the excited state yields a Hamiltonian of the form

$$H = \frac{p_x^2}{2m} + \frac{2\hbar|\chi|^2}{\Delta}g^2(t)\cos(qx). \tag{5.0.3}$$

Integrating the Shrödinger equation $i\hbar\partial_t\psi(x,t) = H\psi(x,t)$ we get the following ex-

pression for the field immediately after interaction

$$\begin{aligned}(x, t = 0^+) &= e^{i\frac{\theta}{2}\cos(qx)}\psi(x, t = 0^-) \\ &= \sum_{n=-\infty}^{\infty} i^n J_n(\theta/2) e^{inqx}\psi(x, t = 0^-)\end{aligned} \tag{5.0.4}$$

where $\theta \equiv -\frac{4|\chi|^2}{\Delta}\int_{-\infty}^{\infty} dt g^2(t)$ is the area of the pulse envelope function squared and $J_n(x)$ is an n$^t h$ order Bessel function of the first kind. We have employed the Jacobi-Anger expansion in Equation 5.0.4 to expand our wave function onto a basis of momentum eigenstates. The assumption of pure phase modulation is justified in the Raman-Nath regime that allows us to ignore the kinetic energy term in the Hamiltonian so Equation 5.0.4 is valid under the condition

$$|\theta|\omega_q\tau/3 \ll 1. \tag{5.0.5}$$

If we assume $\psi(x, t = 0^-)$ is a plane wave and evolve the system under the free particle Hamiltonian then each plane wave component is a stationary state and we can propagate Equation 5.0.4 in time by multiplying by the corresponding phase factor

$$\begin{aligned}\psi(x, t) &= e^{-i\frac{p_x^2}{2m\hbar}t}\psi(x, t = 0^+) \\ &= \sum_{n=-\infty}^{\infty} i^n J_n(\theta/2) e^{inqx - n^2\omega_q t}\end{aligned} \tag{5.0.6}$$

where $\omega_q \equiv \hbar^2 q^2/2m$. This gives us the wave function of the atoms at any time after the lattice pulse for the given set of assumptions. However, it is difficult to calculate the dynamics of any given section of the wavefront from this form. To extract a focal time we take a different approach and use a standard diffraction integral:

$$\psi(x, t) = \int_{-\infty}^{\infty} dx' G(x - x', t - t')\psi(x', t'). \tag{5.0.7}$$

We use the free-atom propagator $G(x, t) = (4\pi i\omega_q t)^{-1/2}\exp\left[i(qx)^2/4\omega_q t\right]$ and the initial wave function $\psi(x', t' = 0) = \exp[i(\theta/2)\cos(qx')]$. By considering a single

lattice site and expanding the wave function about a node/antinode we can make a parabolic approximation $\cos(qx') \approx 1 - (qx')^2/2$ to calculate an ideal focal time. Deviations from ideal behavior come from small contributions from higher order terms (aberrations) and non-linear defocusing. Since the wave function is periodic we can choose the simplest case for x = 0. Evaluating the integral we find the density

$$\rho(x = 0, t) = |\psi(x = 0, t)|^2 \propto (1 - \omega_q t\theta)^{-1}. \tag{5.0.8}$$

Examining Equation 5.0.8 we see a singularity in the density that corresponds to the quadratic focal time

$$t_f = (\omega_q \theta)^{-1}. \tag{5.0.9}$$

Note that the curvature of the lattice is accounted for in ω_q. So now we have established constraints for experimental parameters that allow us to ensure our measurement remains in the thin lens regime as well as a focal time that allows us to characterize our AOSHWS measurement in analogy to the ideal SHWS.

5.1 Vortex Identification with the AOSHWS

Once the velocity field of the condensate has been measured our goal is to determine the location and handedness of all vortices. Many algorithms already exist for this purpose in the study of classical fluid turbulence so we do not need to develop a new one here. We do have a few constraints regarding the type of method we choose. The first is that our vortex detection method must not depend on a linear interpolation between discrete measurement points since the condensate is non-linear. Rather, we should choose one that relies only on the instantaneous velocity data provided by the AOSHWS at discrete spatial points. Second, that it does not require and aggregation of multiple measurement sets since we can only measure the condensate once. Such a method is described by Grafiteaux et al. [61]. Originally developed to analyze Particle Image Velocimetry (PIV) data sets, this method uses two scalar functions Γ_1 and Γ_2 to locally characterize the circulation of the velocity field.

The dimensionless, scalar function Γ_1 is used to determine the location of the vortex core. We define it in the measurement domain as

$$\Gamma_1(P) = \frac{1}{S}\int_{M\in S} \frac{(\boldsymbol{PM}\times\boldsymbol{V_M})\cdot\hat{z}}{||\boldsymbol{PM}||\cdot||\boldsymbol{V_M}||}dS = \frac{1}{S}\int_S \sin(\theta_M)dS \tag{5.1.1}$$

where P and M are points contained in the two dimensional area S and $\hat{z}$ is the unit vector orthogonal to the measurement plane. S is centered about P and $\boldsymbol{PM}$ is a radius vector defined between these two points. $\boldsymbol{V_M}$ is the velocity field component vector at M. It is clear then that θ_M is the angle between the radius vector and the velocity field component it intersects at point M. At the location of an ideal, axisymmetric vortex core the magnitude of this angle, and therefore the magnitude of $\Gamma_1(P)$ will be extremized. To locate vortex cores we evaluate $\Gamma_1(P)$ for every point in the measurement domain and then search for peaks above an empirically determined threshold. Since $|\Gamma_1| \leq 1$ this number is between 0 and 1. Grafiteaux et al. cite the optimal threshold to be 0.9 though we have found it to lie between 0.5 and 0.6 [61]. To adapt Equation 5.1.1 to discretely sampled points we simply demand that S be a fixed rectangular region centered on P, we then replace the integral with a sum over all the points in S and replace the term $1/S$ with $1/N$, where N is the number of points contained in S.

To determine the vortex boundary Grafiteaux et al. make use of the Γ_2 function defined similarly to before.

$$\Gamma_2(P) = \frac{1}{S}\int_{M\in S} \frac{\{\boldsymbol{PM}\times(\boldsymbol{V}_M - \tilde{\boldsymbol{V}}_P)\}\cdot\hat{z}}{||\boldsymbol{PM}||\cdot||\boldsymbol{V}_M - \tilde{\boldsymbol{V}}_P||}dS. \tag{5.1.2}$$

Here $\tilde{\boldsymbol{V}}_P$ is the convection velocity of the fluid in the region S defined as: $\tilde{\boldsymbol{V}}_P = (1/S)\int_S \boldsymbol{V}dS$. The Γ_2 function creates a field exhibiting "plateaus" centered at the vortex location that fall off rapidly after the radial distance at which the vortex velocity reaches a maximum. The vortex boundary is then determined by searching for regions in the Γ_2 field above a threshold which Grafiteaux et al. cite to be $2/\pi$. However, we find the optimal value to be closer to 0.4 [61]. The differences in optimal

thresholds is likely due to differences in the vortex core-geometries considered. Once the boundary of the vortex core is established, the circulation of the vortex may be calculated by integrating the velocity field around it. These expressions may be adapted to discrete measurements in the same manner as Γ_1.

In the case of a Bose-Einstein condensate vorticity is quantized. Thus, for cases of well-separated (on the order of a few healing lengths), singly charged vortices it is sufficient to know their handedness rather than their circulation. For this purpose it is unnecessary to calculate $\Gamma_2(P)$ as the sign of Γ_1 depends on vortex handedness. However if vortices of like sign are closely grouped or multiply charged vortices are present, the Γ_2 function allows us to handle these cases. Of course, in the worst case scenarios it is always possible to rely on qualitative analysis of the velocity field to identify vortices.

5.1.1 Experimental Implementation of Peak Subtraction

Since the AOSHWS method relies on comparison with a flat phase Hartmanngram and we can only measure a single BEC once it seems natural to ask how this could be implemented in experimental reality. To answer this we must state that the only piece of raw data we can obtain from this process is the Hartmanngram of the state of arbitrary phase. However, it is assumed that before we make this measurement we have some initial pieces of information from the characterization of the measurement apparatus. Namely it is assumed that we know the period and irradiance of the optical lattice at the location of the BEC. In addition, we should know the duration of the initial expansion time, the lattice pulse and the second expansion time. Having obtained the Hartmanngram and determining its width we can back-propagate the cloud using a numerical GPE solver to approximate the initial Thomas-Fermi radius and atom number. We can then synthetically generate our truth measurement by forward propagating the approximated initial state with a flat phase.

CHAPTER 6

Measurements of Vorticity in Bose-Einstein Condensates

In this chapter we discuss numerical studies of two methods to determine the vorticity in 2D Bose-Einstein condensates. Both methods make use of optical lattices in order to break up the condensate and allow the subsequent distribution to evolve according to the local velocity field. Both methods determine the location and handedness of vortices providing information about the bulk fluid motion according to the Onsager point vortex model [6]. The first method, which uses a 1D lattice, provides this information using qualitative analysis of the dislocation of the fringes at the location of vortex cores. The second method, which was discussed in Chapter 4, uses a 2D lattice and a peak detection algorithm to extract the velocity field of the BEC. The second measurement provides a wealth of information but we are specifically interested in using it to locate vortex cores and determine their handedness. This can be done in two ways: qualitatively by examining the velocity vectors superimposed onto the density distribution or by using one of any number of existing algorithms to identify vortices in velocity fields. In this dissertation we use the algorithm developed by Grafiteaux et al. [61] implemented in the code written by Sebastian Endrikat [62]. The purpose of this analysis is not to provide an exhaustive optimization of the method but, rather, to give proof-of-principle and demonstrate its feasibility and application.

6.1 Details of the Simulations

The simulations presented in this chapter are written in MATLAB code. They are performed using a split-step method to solve the 2D Gross-Pitaevskii equation on a

512x512 grid of spatial extent 150 μm x 150 μm. The ground state is determined by propagation of a trial wave function according to the damped complex Gross-Pitaevskii equation (cGPE) [63] for a harmonic trap with frequencies $(\omega_x, \omega_y, \omega_z) = 2\pi \times (10, 10, 100)$ Hz and a cloud of $N = 10^6$ ^{87}Rb atoms. Once the ground state is determined, arbitrary phase and density modulations may be introduced into the BEC. For instance, vortices may be introduced into the condensate at location $\boldsymbol{r'}$ by multiplying by the term

$$A_{vort}(\boldsymbol{r}, \boldsymbol{r'}) = \frac{|\boldsymbol{r} - \boldsymbol{r'}|}{\sqrt{(\boldsymbol{r} - \boldsymbol{r'})^2 + \xi^2}} \exp\left[\pm i \tan^{-1} \frac{(\boldsymbol{r} - \boldsymbol{r'})}{l_{arb}}\right] \tag{6.1.1}$$

where the sign on the exponent determines the vortex handedness and l_{arb} is an arbitrary length scale. We define clockwise rotation to be *negative handedness* and counter clockwise rotation to be *positive handedness*. Using this method we can create arbitrary distributions of vortices.

Once the initial state has been created, the measurement process consists of three independently adjustable steps. The first step is a free evolution where the condensate is released from its radial confinement. The condensate is allowed to expand for a time t_{exp_1}. This serves a few purposes, one is to increase the interatomic distance and therefore decrease the density so that the vortex cores increase in size and the velocity field may be sampled at a lower spatial frequency. The other purpose for the initial expansion time is to reduce the strength of the repulsive non-linearity that can blur the final density distribution. The second phase applies a $\lambda = 532$nm optical lattice pulse. The variable parameters of the lattice are the length of the pulse t_{lat}, its amplitude U_{lat} (quantified in terms of the BEC chemical potential μ) and its period λ_{lat}. After the lattice pulse, the third step step is another period of free expansion where we allow the BEC to break up into sub-condensates and come to focus. Though the time over which this happens, t_{exp_2} is a degree of freedom, the quadratic focal time t_{Focus} is determined for a linear atom cloud by the lattice pulse properties as discussed in Chapter 4.

6.2 Previous Methods

To date, measurement of a kinetic energy spectrum of quantum turbulence in a BEC reamins a challenge. There have been several experiments that detected a vortex and measured its associated phase winding [20–22]. Most experiments have attempted to determine the phase through interfereometric methods while one measured vortex handedness and location via spatially resolved Bragg scattering [19]. Though these methods are effective for determining vortex location and handedness they do not measure the velocity field of the condensate and in the case of the interfereometric measurements require a complex and delicate timing sequence and have not been demonstrated for complex vortex distributions. In addition, the efficacy of these methods depends on the species of atom while the method presented here is completely general.

6.3 Determining Vortex Handedness Using a 1D Optical Lattice

In this method a BEC is subjected to a fast, off-resonant pulse of light patterned as a 1D lattice in the plane of the condensate. The lattice pulse creates a wave function with fringe-like regions of high and low density. Since these fringes are the product of phase modulation versus amplitude modulation the atoms are not trapped by the optical potential and travel with trajectories determined by their velocities in the initial state. After a period of free evolution the fringes will display a characteristic dislocation at the location of the vortex cores. As shown in Figure 6.1 the orientation of this dislocation is determined by the vortex handedness.

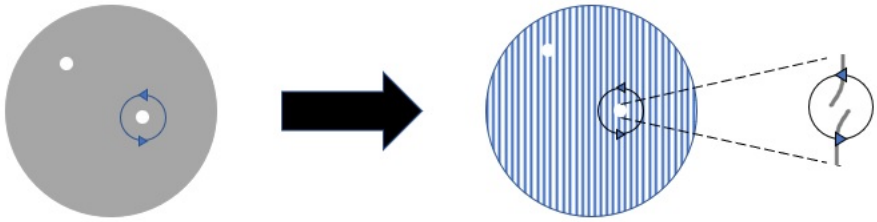

FIGURE 6.1. In the 1D lattice measurement the BEC density is broken into periodic fringes. These fringes are dislocated near the vortex cores in a direction determined by the vortex handedness.

The nature of this fringe dislocation is different than that considered in the previous section. Previous investigations [20–22] considered fringes generated from the interference of two condensates held at different locations in the trap populated by different Zeeman sublevels. At the location of a vortex core these fringes displayed a forking geometry or *screw dislocation*. In contrast, our measurement creates fringes non-interfereometrically and the dislocations are simply caused by the opposing signs of the velocity vectors on either side of the vortex core. By using a standing wave of light to impose periodicity onto the wave function we greatly simplify the experimental setup and the geometry of the fringes is determined only by the characteristics of the laser field. In addition, with proper measurement parameters multiple fringes display dislocation as opposed to the single dislocation displayed in interfereometric measurements. This makes it easier to resolve optically though closely spaced vortices can be more difficult to distinguish.

6.4 Numerical Results for 1D Lattice

We performed a short numerical analysis of the 1D lattice system on a 1024x1024 grid of spatial extent 150 μm x 150 μm. We proceeded by varying the experimental parameters in order to maximize the visual distortion of the fringes at the location of

vortex cores. We found a good set of parameters to be lattice period $\lambda_{lat} = 1.3$ μm, lattice amplitude $U_{lat} = 1\mu$, lattice pulse duration $t_{lat} = 220$ μs and final expansion time $t_{exp_2} = 1$ ms. Figure 6.2 displays our results for a singly charged, centered vortex of each handedness. Examining this figure it is clear that the orientation of the fringe dislocation is determined by the vortex charge.

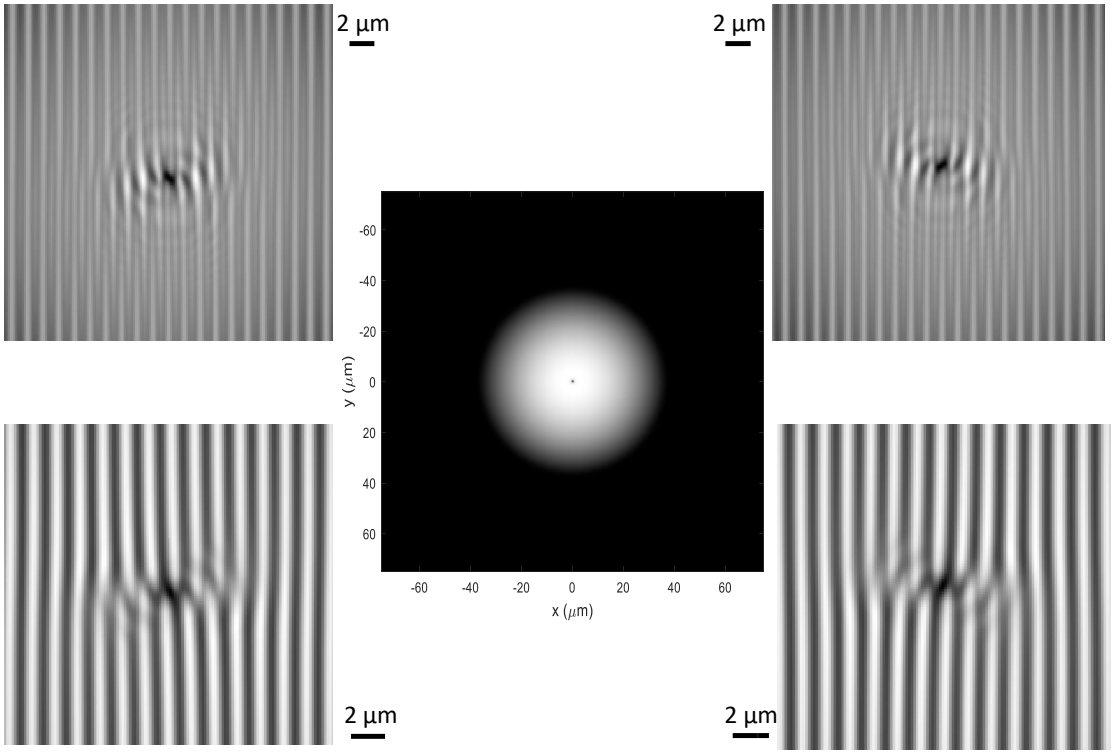

FIGURE 6.2. Wave function density distributions for the 1D lattice measurement with a singly charged centered vortex. **Middle:** Initial distribution. **Top Left:** Positive handedness, $t_{exp_1} = 0$ ms. **Top Right:** Negative handedness $t_{exp_1} = 0$ ms. **Bottom Left:** Positive handedness $t_{exp_1} = 10$ ms. **Bottom Right:** Negative handedness $t_{exp_1} = 10$ ms. Simulations performed on 1024x1024 grid with fixed parameters $\lambda_{lat} = 1.3$ μ m, $U_{lat} = 1\mu$, $t_{lat} = 220$ μs, and $t_{exp_2} = 1$ ms.

We can see that for $t_{exp_1} = 0$ ms the density fringes are extremely blurred. This is likely due to the non-linear component of the Hamiltonian which is more prominent for higher density condensates.

To test how the method would perform with larger vortex distributions and more closely spaced vortices we performed the same measurement for a distribution of five singly charged vortices that contained several isolated cores and a cluster of three. We varied the initial expansion time to see how it would affect our ability to resolve individual vortices in a cluster.

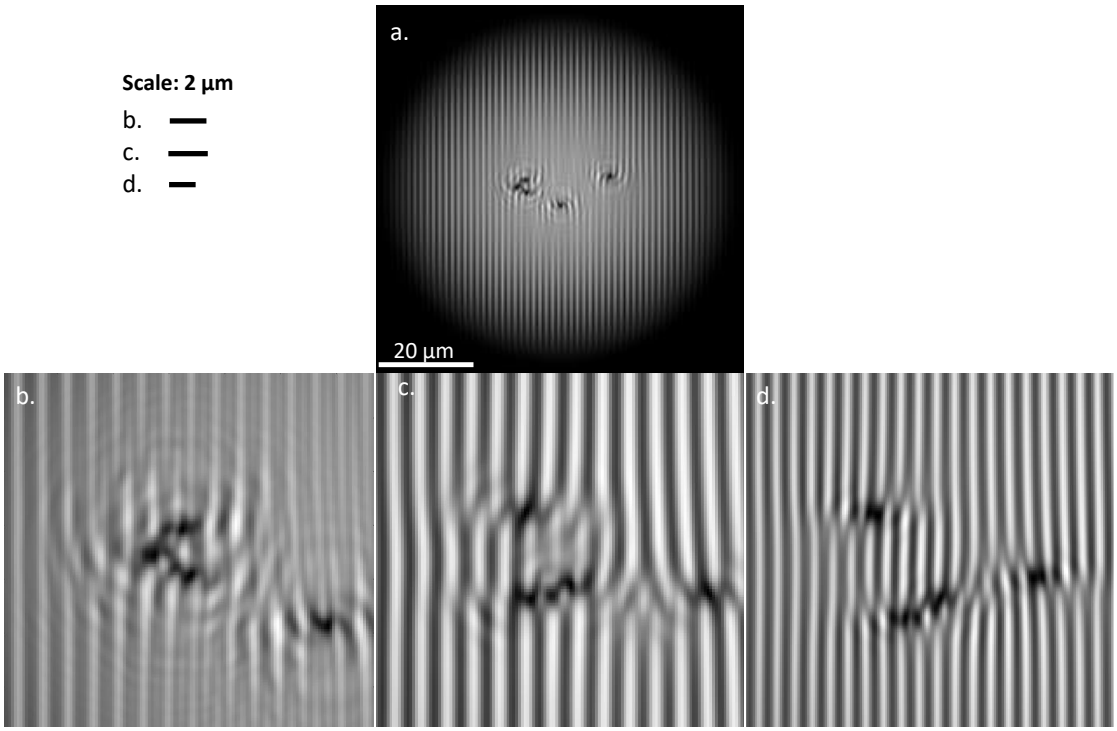

FIGURE 6.3. Wave function density distributions for the 1D lattice measurement with a distribution of five singly charged vortices. **a.** Full cloud density post measurement displaying vortex arrangement for $t_{exp_1} = 0$ ms. **b.** Detail of the three-vortex cluster for, $t_{exp_1} = 0$ ms **c.** Detail of the three-vortex cluster for, $t_{exp_1} = 10$ ms **d.** Detail of the three-vortex cluster for, $t_{exp_1} = 20$ ms. Simulations performed on 1024x1024 grid with fixed parameters $\lambda_{lat} = 1.3$ μm, $U_{lat} = 1\mu$, $t_{lat} = 220$ μ s $t_{exp_2} = 1$ ms. Scales of the zoomed panels may be referenced to the lattice period.

It seems clear that while the measurement is effective for well-separated vortices, more complicated distributions render it impractical. Longer expansion times are essential to be able to mitigate the nonlinear fringe-blurring. Furthermore it cannot

measure compressible velocity components and is only sensitive along one direction. It may be possible to determine the magnitude of a vortex's charge by measuring the width of the fringe dislocation but we did not investigate this. Though its applications are limited, the 1D lattice measurement is an easily implementable method that can allow characterization of quantized vorticity fields and provides an intuitive step towards the measurement of a BEC velocity field with a 2D lattice.

6.5 Measuring the Velocity Spectrum of a BEC with a 2D Optical Potential

In Section 5 we argued that, under the right conditions, an off-resonance 2D optical lattice should behave similarly to a conventional Shack-Hartmann Wavefront sensor for a matter wave. To test the feasibility of this measurement we performed simulations using the method described in the beginning of this chapter. Examples images of the atom density throughout the measurement process are shown in Figure 6.4.

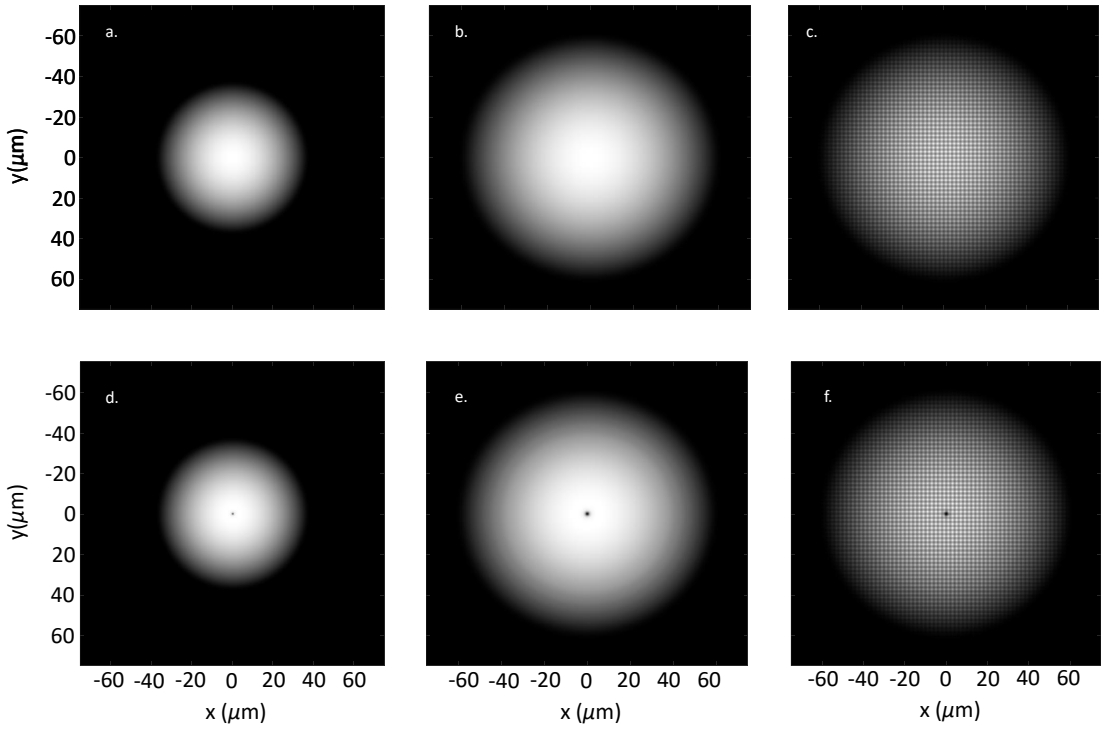

FIGURE 6.4. Wave function density distributions at various points in measurement process with and without vortex. Top row: No vortex, **a.** Uniform ground state before expansion, **b.** Density after expansion, **c.** Density after lattice pulse and second expansion. Bottom Row: Single, centered, vortex, **e.** Vortex imprinted state before expansion, **f.** Density after expansion, **g.** Density after lattice pulse and second expansion. Both rows use settings $t_{exp_1} = 20$ ms, $t_{lat} = 220$ μ s, $U_{lat} = 1\mu$, $\lambda_{lat} = 2$ μ m, and $t_{exp_2} = t_{Focus}$.

All simulations used a square lattice and again, the variable parameters are initial expansion time t_{exp_1}, lattice period λ_{lat}, lattice amplitude U_{lat} and pulse duration t_{lat}. Final expansion time t_{exp_2} is fixed at t_{Focus} unless otherwise specified. Once the Hartmanngram is obtained the peak locations are measured using a matched-filter algorithm. To find slopes we generated Hartmanngrams for both the uniform ground state and the state of arbitrary phase to be measured. The peak locations are subtracted and converted into column vectors of velocity measurements that are then mapped to the locations of the lattice nodes as shown in Figures: 6.5 and 6.6.

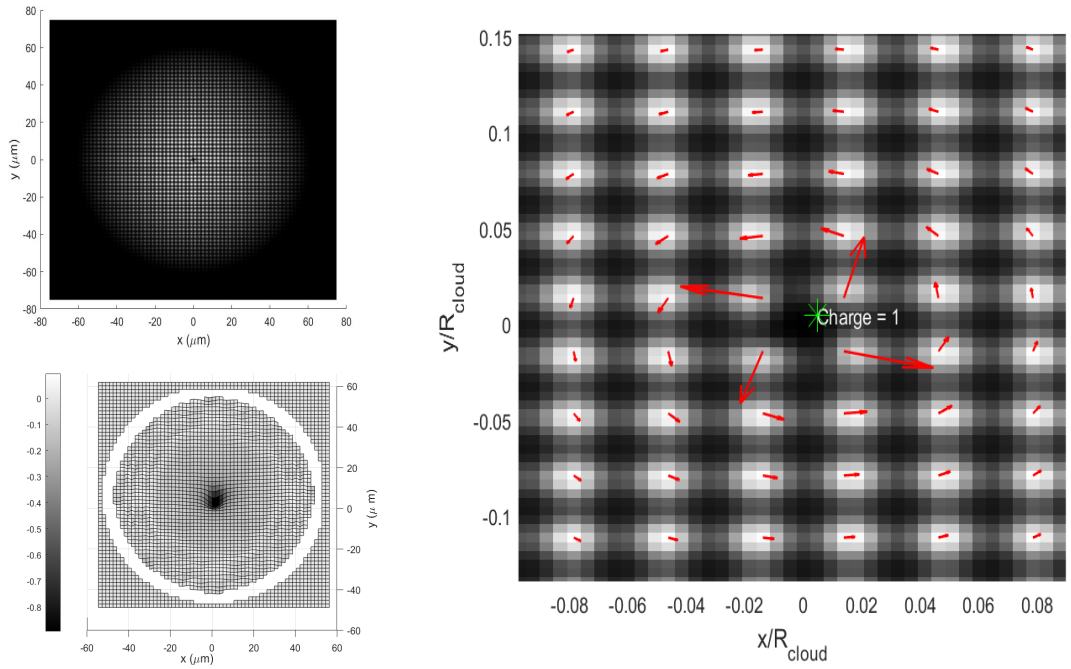

FIGURE 6.5. Example of measurement outcomes for single, centered vortex of charge +1. **Top Left:** Full post-measurement density. **Bottom Left**: Γ_1 function evaluated for every point in measurement domain. **Right:** Magnified detail of post-measurement density with velocity vectors mapped to unperturbed density peak locations and vortex location and charge information tag. Experimental settings were $t_{exp_1} = 20ms$, $t_{lat} = 500$ μs, $U_{lat} = 1\mu$, $\lambda_{lat} = 1.4$ μm, $t_{exp_2} = t_{Focus} = 10$ μs.

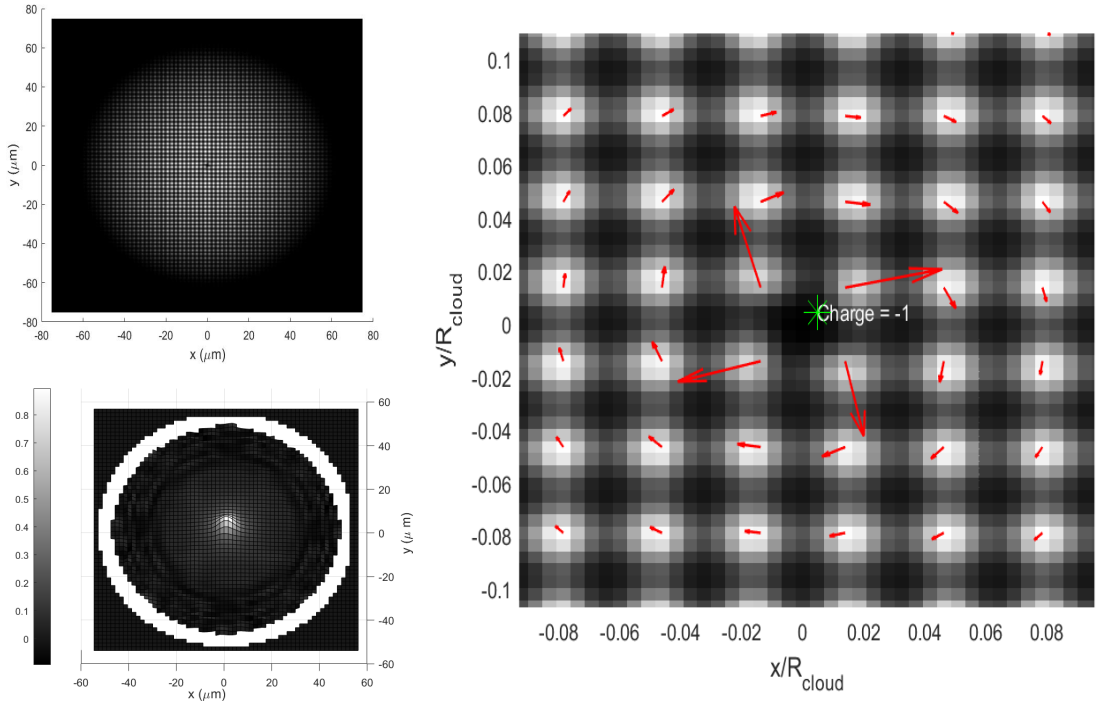

FIGURE 6.6. Example of measurement outcomes for single, centered vortex of charge -1. **Top Left:** Full post-measurement density. **Bottom Left**: Γ_1 function evaluated for every point in measurement domain. **Right:** Magnified detail of post-measurement density with velocity vectors mapped to unperturbed density peak locations and vortex location and charge information tag. Experimental settings were $t_{exp_1} = 20ms$, $t_{lat} = 500$ μs, $U_{lat} = 1\mu$, $\lambda_{lat} = 1.4$ μm, $t_{exp_2} = t_{Focus} = 10$ μs.

This measurement technique returns faithful values of the fluid velocity, however, these values are defined only at the peaks of the Hartmanngram. In the classical SHWS these measurements are decomposed on a basis of Zernike polynomials that map the discrete points back to a continuous field. In this case the condensate phase is non-linear and we cannot linearly interpolate between these values to map the measurements to every point on the continuous fluid density. Instead, in any case where interpolation is necessary we take each lattice site and set the value of the field at the points contained within it equal to the value of the measurement at the corresponding Hartmanngram peak. Thus we are directly sampling the gradient

of the phase across the condensate at a period equal to that of the lattice. This is evident in the plots of the Γ_1 and Γ_2 fields in Figures 6.5 and 6.6. When the lattice period is too large we cannot resolve the spatial features of the velocity field necessary to detect vortices as is expected from standard sampling considerations. However, if the lattice period becomes too small we run into several other issues. Each Hartmanngram peak must span a diameter covering enough pixels to be able to resolve displacements accurately. In this simulation we are limited by our grid size while in a real experiment we would be limited by the pixel pitch of the camera and the magnification of the imaging system. In addition, the sub-condensates must not contact each other before imaging. A smaller lattice period means t_{Focus} must reduce accordingly and we may reach experimental limits. On a more fundamental level: a smaller lattice site corresponds to a smaller atom number. The Hartmanngram spots must contain enough atoms to provide a detectable signal to noise ratio for the imaging system. The consequences of sampling frequency within the limits of simulation coupled with the vortex identification algorithm in its current form are a major part of the analysis we perform in the following section.

6.6 Numerical Results for the AOSHWS

To investigate how the lattice period effects our ability to resolve vorticity in a condensate we performed a series of simulations in which we varied λ_{lat} for several values of t_{exp_1} on a 512x512 grid of spatial extent 150 μm x 150 μm. These simulations all used the same initial 10 vortex distribution shown in Figure 6.7. We used this distribution because it contains several classes of commonly studied vortex structures including single vortices at various radial positions, a vortex dipole and a cluster of three vortices. We can see in the left-most panes of the figure that the annihilating pair produce a large sound wave that propagates through the condensate as it expands. This adds an irrotational component to the velocity field that the AOSHWS

method is also able to identify. As a bonus it allows us to demonstrate that the AOSHWS can detect vorticity in the presence of acoustic disturbances which might be present in a real BEC experiment.

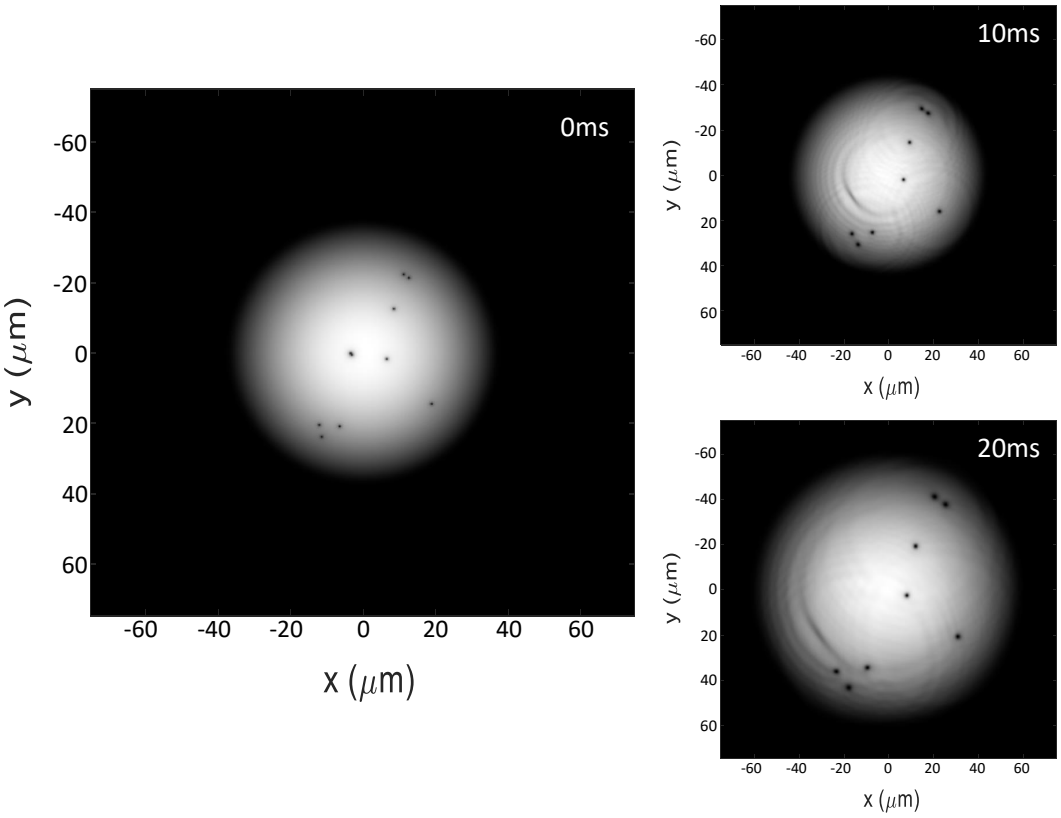

FIGURE 6.7. Initial vortex distribution used to determine optimal range of λ_{lat} for several values of t_{exp_1}. **Left:** $t_{exp_1} = 0$ ms, **Top Right:** $t_{exp_1} = 10$ ms, **Bottom Right:** $t_{exp_1} = 20$ ms. Vortex distribution contains several isolated vortices at various radial positions, a vortex dipole, a three-vortex cluster and an annihilating vortex pair.

We varied λ_{lat} over the range $1.0 - 3.4$ μm for values of $t_{exp_1} = 0, 10, 20$ ms. We picked three sampling conditions for each expansion time to demonstrate measurement performance for under-sampled, over-sampled and ideally-sampled lattices. From the plots in Figures 6.8, 6.9 and 6.10 we can see that there are no values of λ_{lat} over the range examined that allowed the vortex identification algorithm to identify all

present vortices with no initial expansion. It was expected that the annihilating pair would not be identified as the velocity fields of the closely spaced, oppositely charged vortices cancel each other out for distances greater than a few healing lengths.

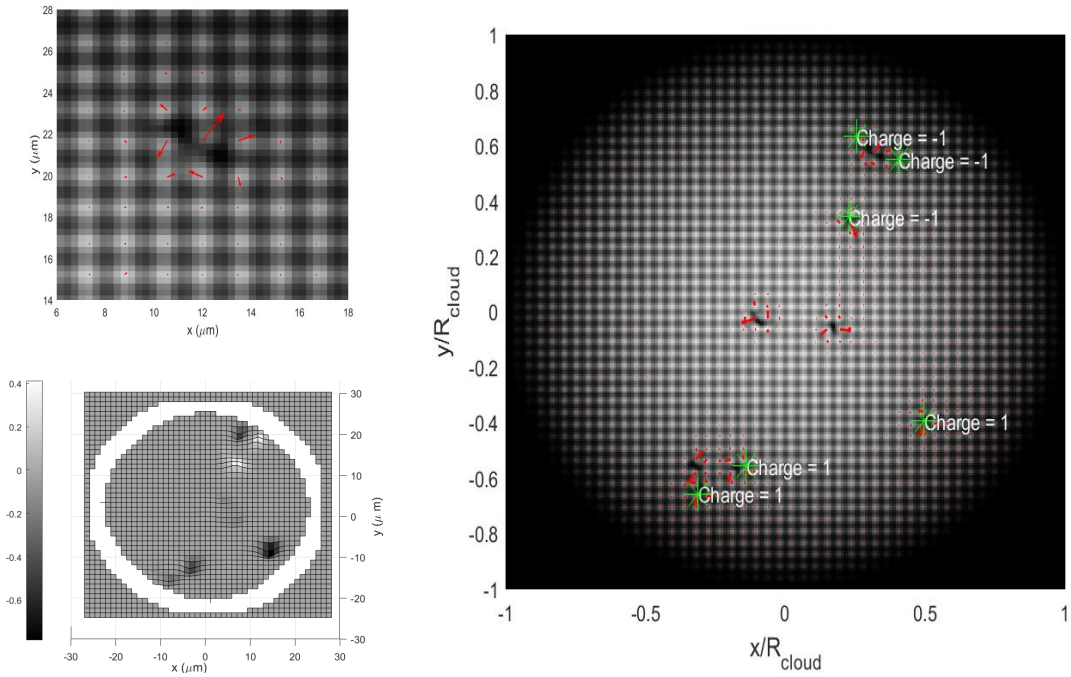

FIGURE 6.8. Initial vortex distribution expanded $t_{exp_1} = 0$ ms sampled at $\lambda_{lat} = 1.6$ μm. **Right:**Full post-measurement density with velocity vectors mapped to unperturbed density peak locations and vortex location and charge information tag. **Top Left:** Magnified detail of upper right vortex dipole with velocity vectors mapped to unperturbed density peak locations. **Bottom Left**: $(\Gamma_1)^3$ function evaluated for every point in measurement domain. Fixed settings: $t_{lat} = 500$ μs, $U_{lat} = 1\mu$, $t_{exp_2} = t_{Focus}$.

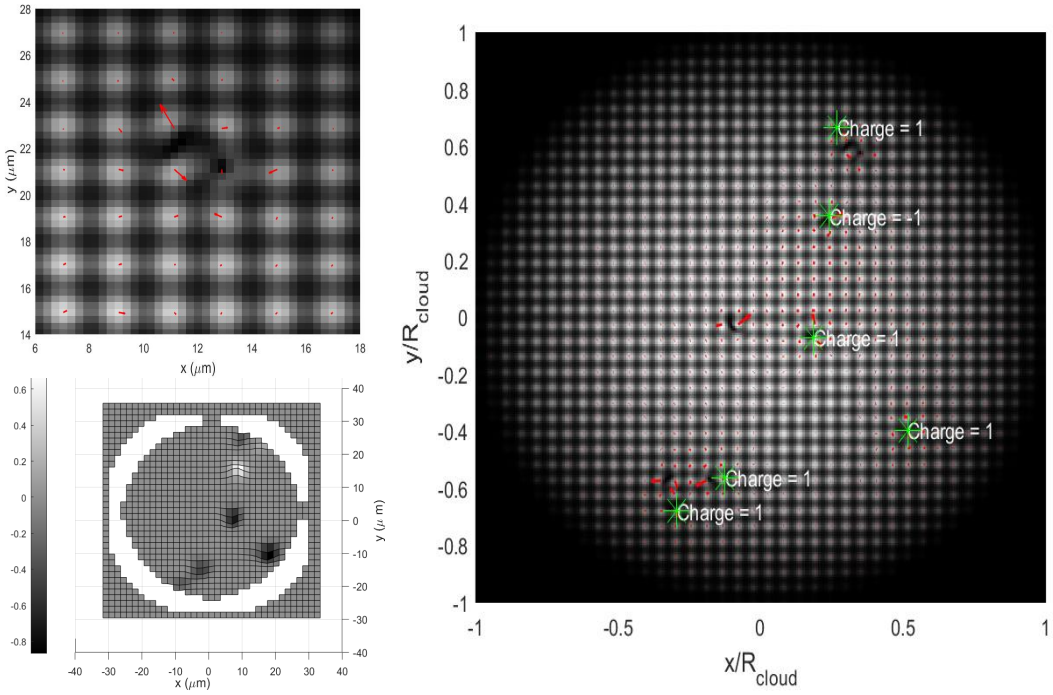

FIGURE 6.9. Initial vortex distribution expanded $t_{exp_1} = 0$ ms sampled at $\lambda_{lat} = 2\ \mu$m. **Right:**Full post-measurement density with velocity vectors mapped to unperturbed density peak locations and vortex location and charge information tag. **Top Left:** Magnified detail of upper right vortex dipole with velocity vectors mapped to unperturbed density peak locations. **Bottom Left**: $(\Gamma_1)^3$ function evaluated for every point in measurement domain. Fixed settings: $t_{lat} = 500\ \mu$s, $U_{lat} = 1\mu$, $t_{exp_2} = t_{Focus}$.

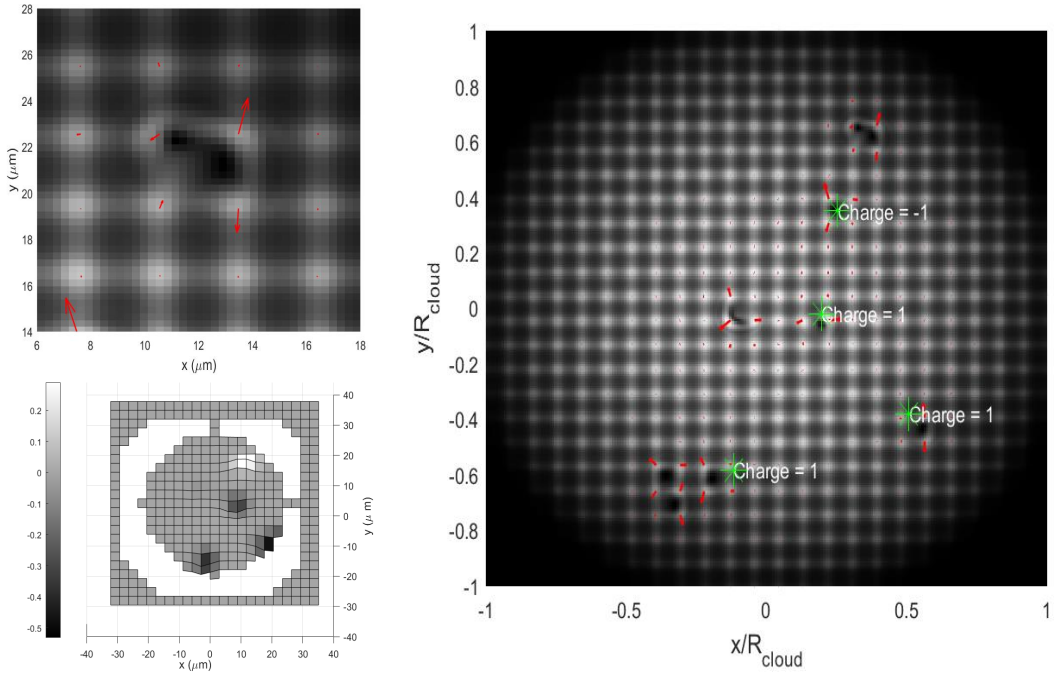

FIGURE 6.10. Initial vortex distribution expanded $t_{exp_1} = 0$ ms sampled at $\lambda_{lat} = 3$ μm. **Right:**Full post-measurement density with velocity vectors mapped to unperturbed density peak locations and vortex location and charge information tag. **Top Left:** Magnified detail of upper right vortex dipole with velocity vectors mapped to unperturbed density peak locations. **Bottom Left**: $(\Gamma_1)^3$ function evaluated for every point in measurement domain. Fixed settings: $t_{lat} = 500$ μs, $U_{lat} = 1\mu$, $t_{exp_2} = t_{Focus}$.

The plots in Figures 6.11, 6.12 and 6.13 show results for an initial expansion time of 10ms. We were able to correctly identify all present vortices for sampling periods in the range $\lambda_{lat} = 1.6 - 1.7$ μm However, we could visually identify vortex location and charge from the velocity field over a much larger range.

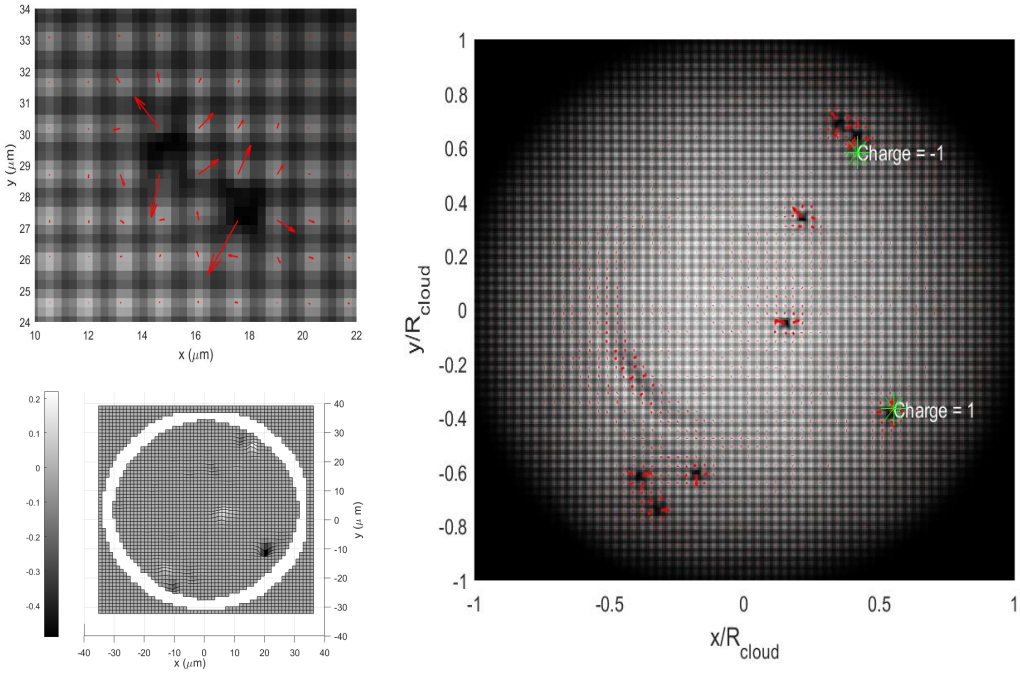

FIGURE 6.11. Initial vortex distribution expanded $t_{exp_1} = 10$ ms sampled at $\lambda_{lat} = 1.4$ μm. **Right:**Full post-measurement density with velocity vectors mapped to unperturbed density peak locations and vortex location and charge information tag. **Top Left:** Magnified detail of upper right vortex dipole with velocity vectors mapped to unperturbed density peak locations. **Bottom Left**: $(\Gamma_1)^3$ function evaluated for every point in measurement domain. Fixed settings: $t_{lat} = 500$ μs, $U_{lat} = 1\mu$, $t_{exp_2} = t_{Focus}$.

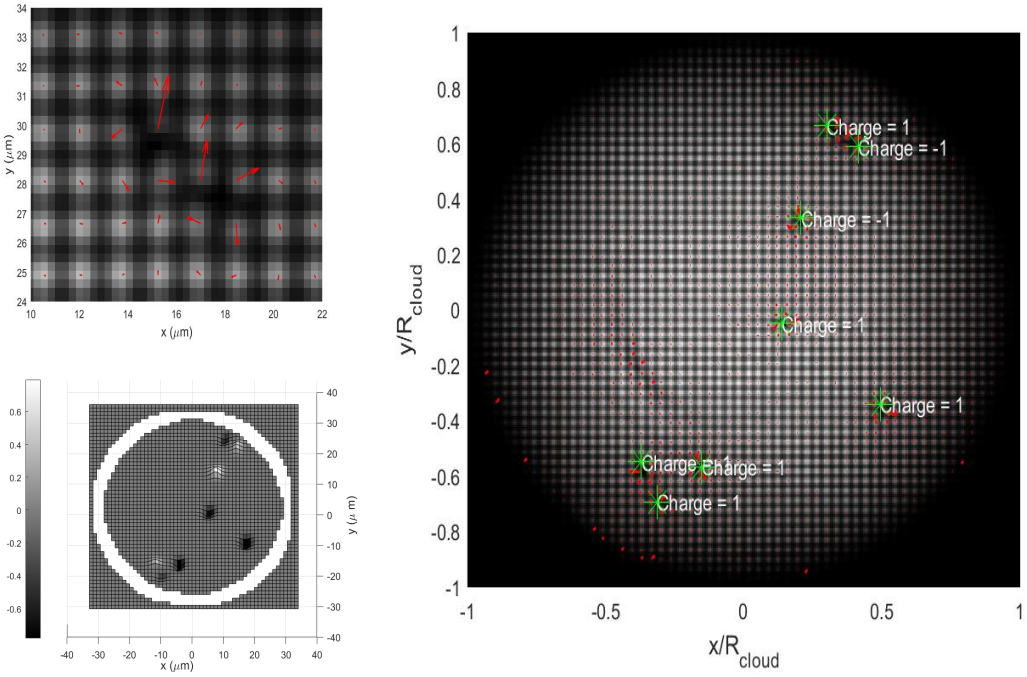

FIGURE 6.12. Initial vortex distribution expanded $t_{exp_1} = 10$ ms sampled at $\lambda_{lat} = 1.6$ μm. **Right:**Full post-measurement density with velocity vectors mapped to unperturbed density peak locations and vortex location and charge information tag. **Top Left:** Magnified detail of upper right vortex dipole with velocity vectors mapped to unperturbed density peak locations. **Bottom Left**: $(\Gamma_1)^3$ function evaluated for every point in measurement domain. Fixed settings: $t_{lat} = 500$ μs, $U_{lat} = 1\mu$, $t_{exp_2} = t_{Focus}$.

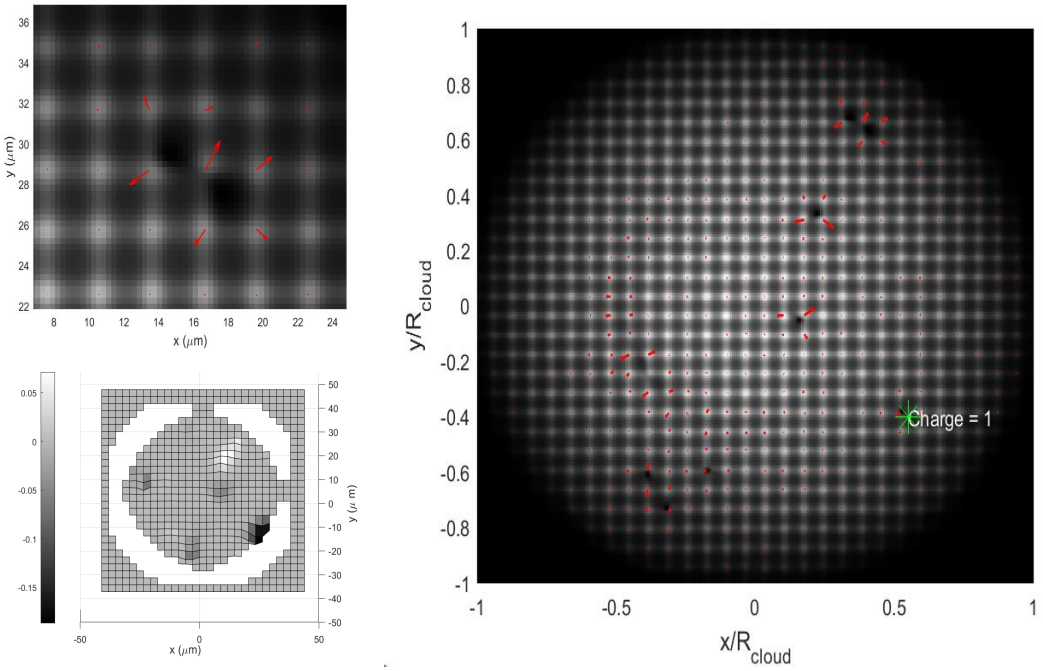

FIGURE 6.13. Initial vortex distribution expanded $t_{exp_1} = 10$ ms sampled at $\lambda_{lat} = 3$ μm. **Right:**Full post-measurement density with velocity vectors mapped to unperturbed density peak locations and vortex location and charge information tag. **Top Left:** Magnified detail of upper right vortex dipole with velocity vectors mapped to unperturbed density peak locations. **Bottom Left**: $(\Gamma_1)^3$ function evaluated for every point in measurement domain. Fixed settings: $t_{lat} = 500$ μs, $U_{lat} = 1\mu$, $t_{exp_2} = t_{Focus}$.

For an initial expansion time of 20 ms we found all vortices were correctly identified for sampling periods in the range $\lambda_{lat} = 1.5 - 2.3$ μm and from the corresponding Figures 6.14, 6.15 and 6.16 we can see that qualitative identification is possible over almost the full range of tested sampling frequencies.

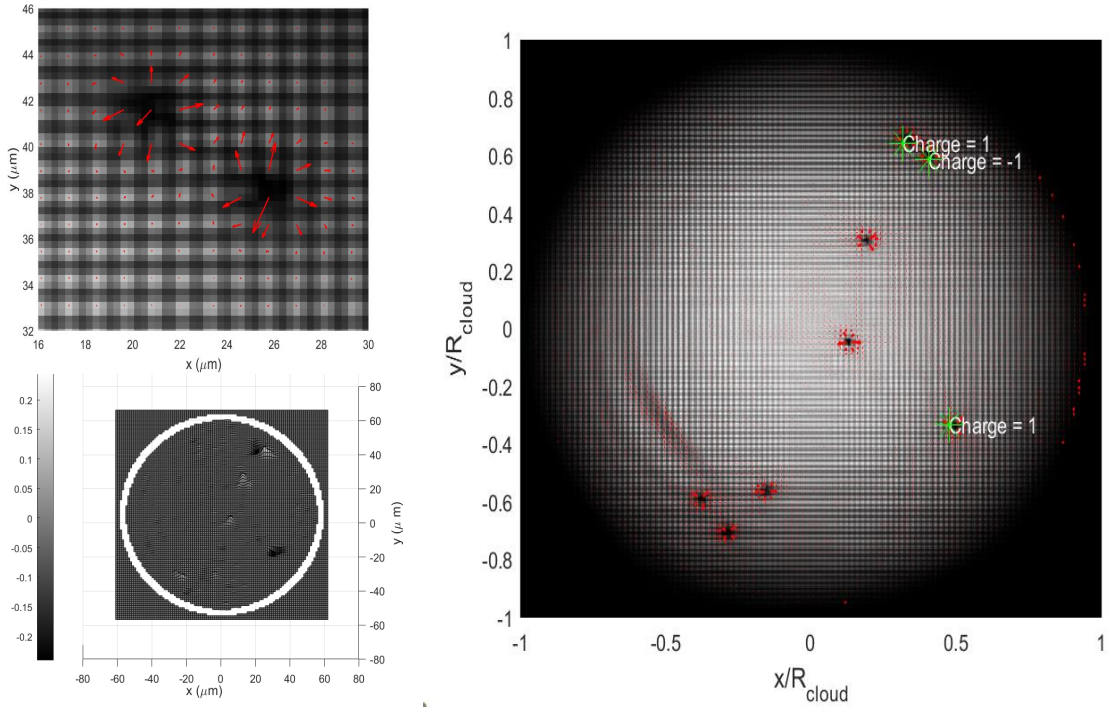

FIGURE 6.14. Initial vortex distribution expanded $t_{exp_1} = 20$ ms sampled at $\lambda_{lat} = 1.2$ μm. **Right:** Full post-measurement density with velocity vectors mapped to unperturbed density peak locations and vortex location and charge information tag. **Top Left:** Magnified detail of upper right vortex dipole with velocity vectors mapped to unperturbed density peak locations. **Bottom Left**: $(\Gamma_1)^3$ function evaluated for every point in measurement domain. Fixed settings: $t_{lat} = 500$ μs, $U_{lat} = 1\mu$, $t_{exp_2} = t_{Focus}$.

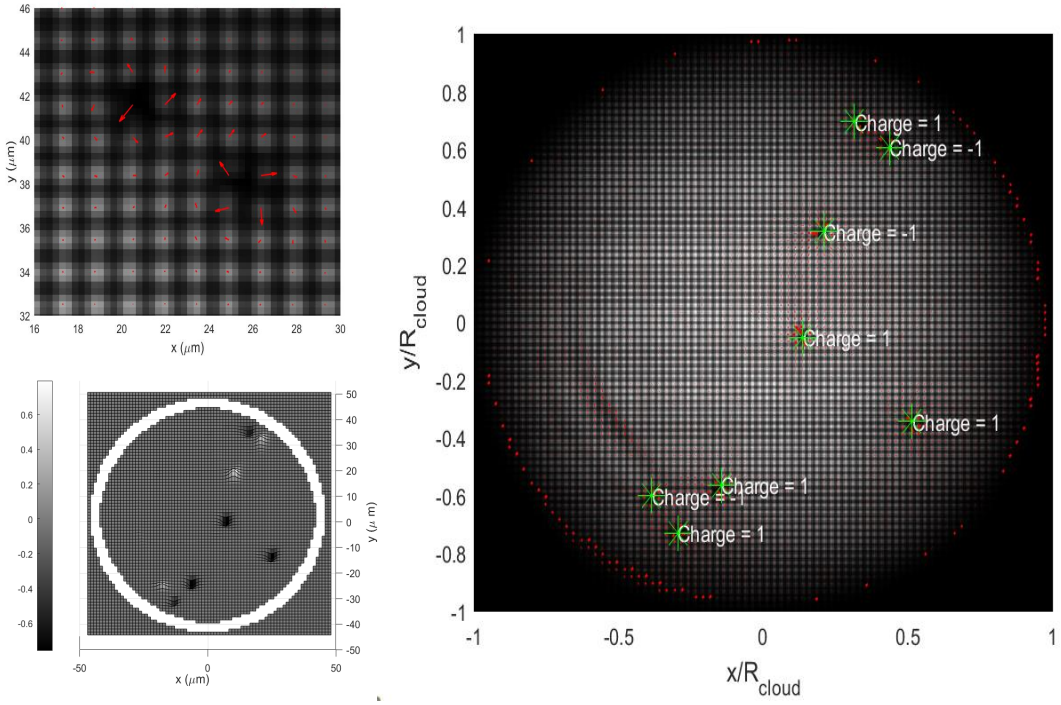

FIGURE 6.15. Initial vortex distribution expanded $t_{exp_1} = 20$ ms sampled at $\lambda_{lat} = 1.5$ μm. **Right:** Full post-measurement density with velocity vectors mapped to unperturbed density peak locations and vortex location and charge information tag. **Top Left:** Magnified detail of upper right vortex dipole with velocity vectors mapped to unperturbed density peak locations. **Bottom Left**: $(\Gamma_1)^3$ function evaluated for every point in measurement domain. Fixed settings: $t_{lat} = 500$ μs, $U_{lat} = 1\mu$, $t_{exp_2} = t_{Focus}$.

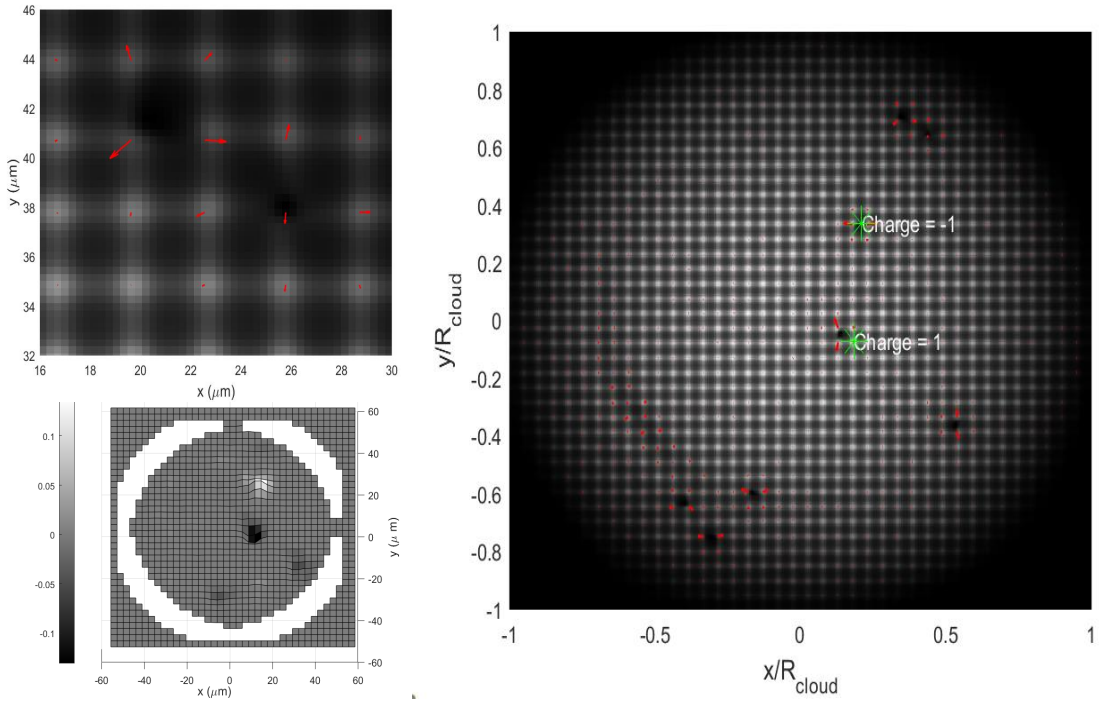

FIGURE 6.16. Initial vortex distribution expanded $t_{exp_1} = 20$ ms sampled at $\lambda_{lat} = 3$ μm. **Right:** Full post-measurement density with velocity vectors mapped to unperturbed density peak locations and vortex location and charge information tag. **Top Left:** Magnified detail of upper right vortex dipole with velocity vectors mapped to unperturbed density peak locations. **Bottom Left**: $(\Gamma_1)^3$ function evaluated for every point in measurement domain. Fixed settings: $t_{lat} = 500$ μs, $U_{lat} = 1\mu$, $t_{exp_2} = t_{Focus}$.

Increased range of the ideal sampling period with expansion time is an expected result. We found that for each expansion time we were able to measure faithful velocity fields for a large range of lattice periods above $\lambda_{lat} = 1$ μm even if vortices were not identified by the algorithm. Below this value velocity fields were nonsensical over most of the condensate due to numerical sampling limits stemming from the grid size. Figure 6.17 plots the percentage of vortices correctly identified in the initial distribution for each sampling condition. In the case of $t_{exp_1} = 0$ ms we neglected the annihilating pair so each case considers eight singly charged vortices. To calculate the success percentage we counted the number of properly located vortices ($N_{Located}$)

and the number of properly assigned charges ($N_{Charged}$) for each condition. We then compared this to a perfect score (in this case: 8^2) as in Equation 6.6.1:

$$\%Success = 100 \times \left[1 - \frac{N_{Vortices}^2 - N_{Located} \times N_{Charged}}{N_{Vortices}^2}\right]. \tag{6.6.1}$$

Figure 6.17 clearly shows that performance in the ideal sampling region improves with initial expansion time. However, in the under-sampled region $t_{exp_1} = 0$ ms outperforms the other expansion times.

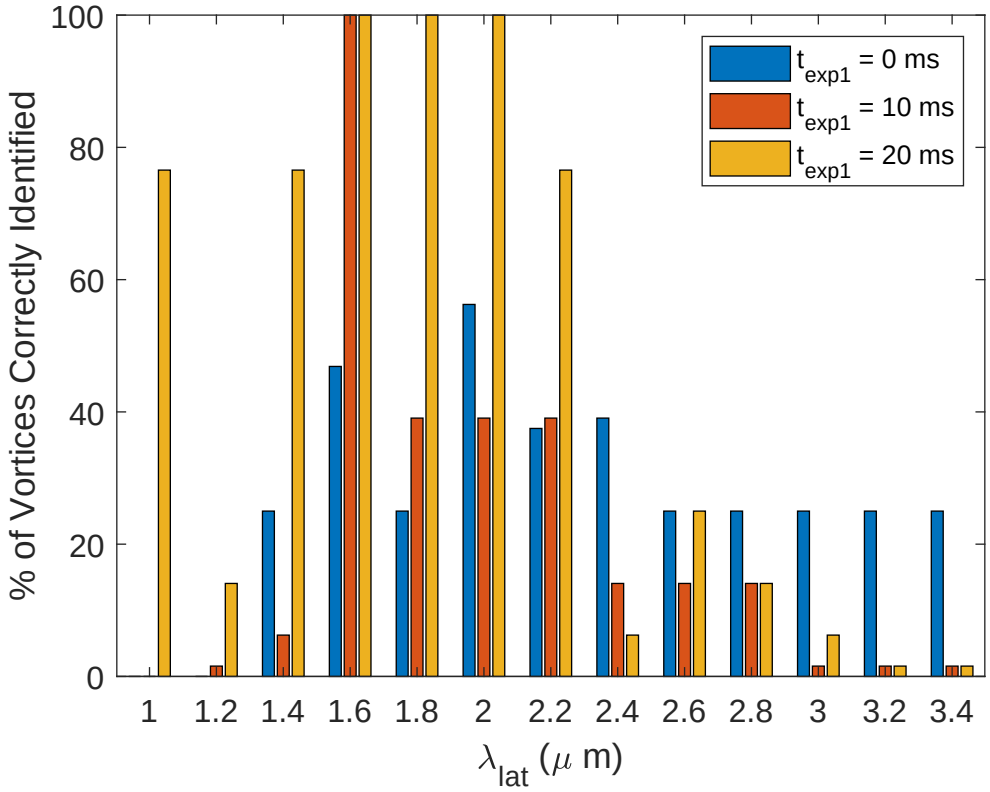

FIGURE 6.17. Percent of vortices in sample distribution correctly identified for each λ_{lat} and t_{exp_1} considered. Simulations were carried out on a 512x512 grid of spatial extent 150 μm x 150 μm with fixed settings $t_{lat} = 500$ μs, $U_{lat} = 1\mu$, $t_{exp_2} = t_{Focus}$, $\Gamma_1^{Threshold} = 0.5$, $\Gamma_2^{Threshold} = 0.35$.

To try to distinguish between physical and numerical limitations in the system as well as explore smaller lattice periods we performed a similar set of measurements

on a 1024x1024 grid. We used a different initial vortex distribution that contained similar sub-structures shown in Figure 6.18.

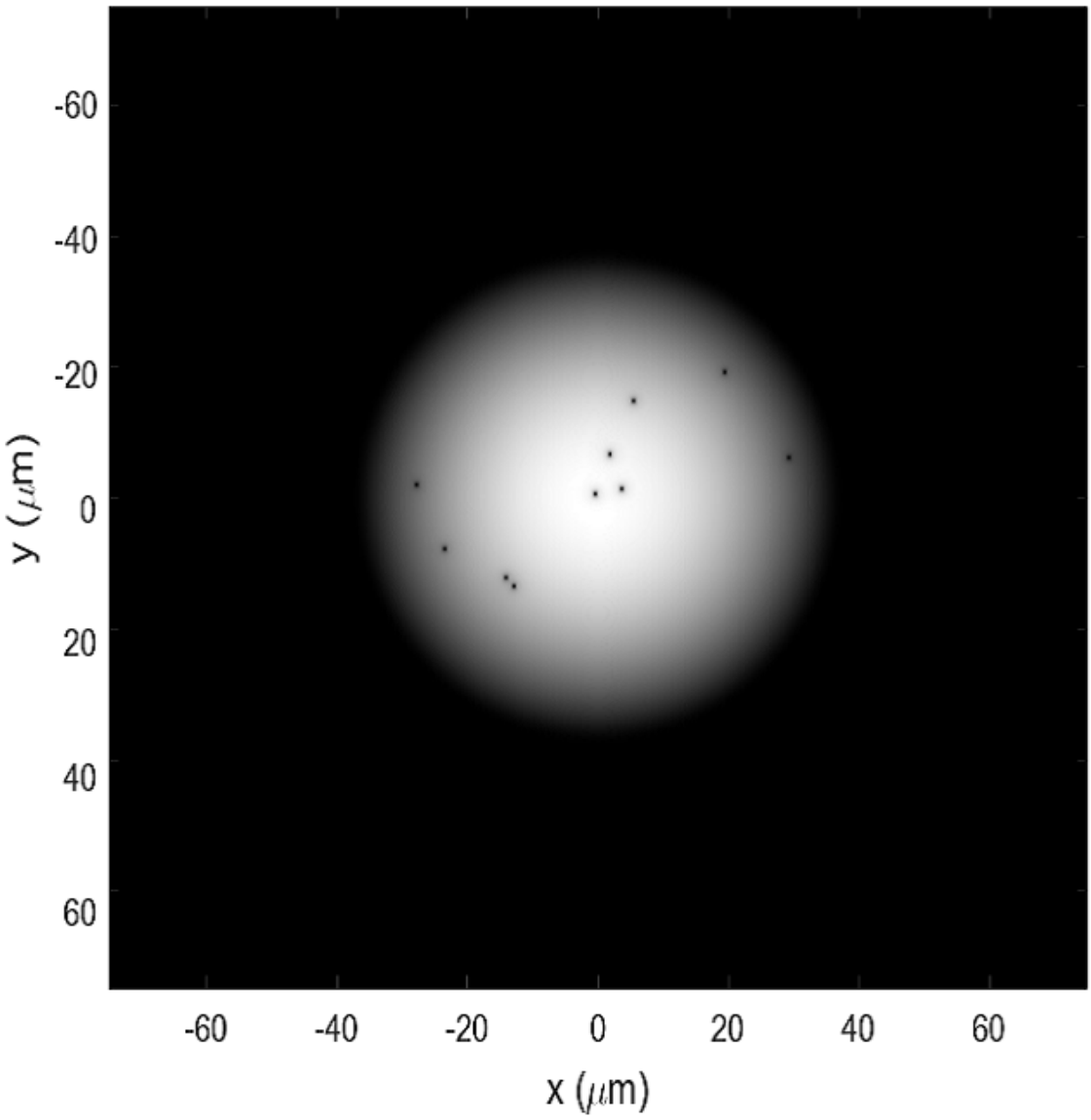

FIGURE 6.18. Initial vortex distribution used for AOSHWS analysis on a 1024x1024 of spatial extent 150 μm x 150 μm grid.

With the larger grid we found that the average success percentage of vortex detection increased while the optimal range of lattice periods did not shift appreciably.

The exception to this is for $t_{exp_1} = 0$ ms though considering the behaviour at the other initial expansion times this is likely due to the vortex distribution rather than the grid size or underlying physics. The larger grid did allow us to resolve Hartmanngram peak displacements for lattice periods less than or equal to 1 μm. However, the vortex detection algorithm was not very successful at these higher sampling frequencies.

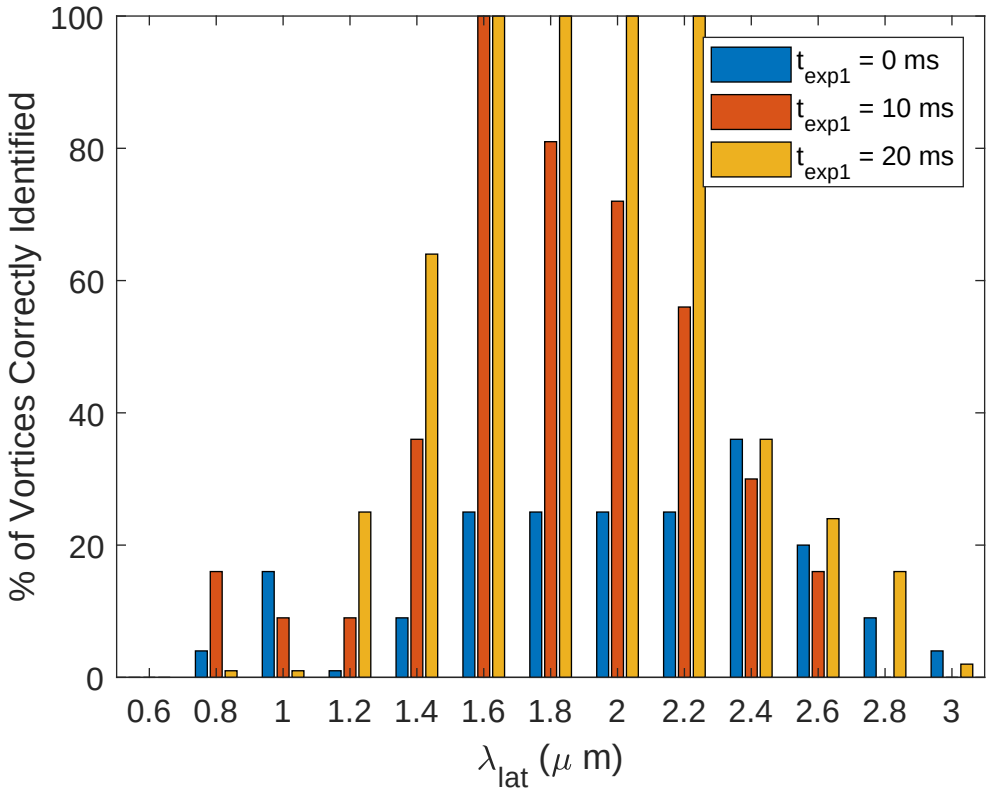

FIGURE 6.19. Percent of vortices in sample distribution correctly identified for each λ_{lat} and t_{exp_1} considered. Simulations were carried out on a 1024x1024 grid of spatial extent 150 μm x 150 μm with fixed settings $t_{lat} = 500$ μs, $U_{lat} = 1\mu$, $t_{exp_2} = t_{Focus}$, $\Gamma_1^{Threshold} = 0.5$, $\Gamma_2^{Threshold} = 0.35$.

To improve performance at these sampling frequencies we varied U_{lat} and t_{exp_2} for a test lattice period of 1 μm. The vortex identification success rate was not improved varying the lattice amplitude over the range $U_{lat} = 0.5\mu - 1.5\mu$. Varying the secondary

expansion time for fixed $\lambda_{lat} = 1$ μm and $t_{exp_1} = 0$ ms we found an increase in vortex identification success rate of 100 percent over the range $t_{exp_2} = 8t_{Focus} - 10t_{Focus}$ as shown in Figure 6.20. There was no improvement for initial expansion times $t_{exp_1} = 10, 20$ ms. This points to an important relation between the non-linearity of the condensate and the focusing parameters of the lattice wherein the quadratic approximation to the induced phase-curvature breaks down for higher BEC densities. However, we must be careful when drawing conclusions about the physical properties of the system from the performance of the vortex algorithm as it presents its own variables for optimization. A detailed numerical study of the relation between the optical focal time of the lattice and the initial expansion time is not presented here but should be part of any further investigation into the AOSHWS.

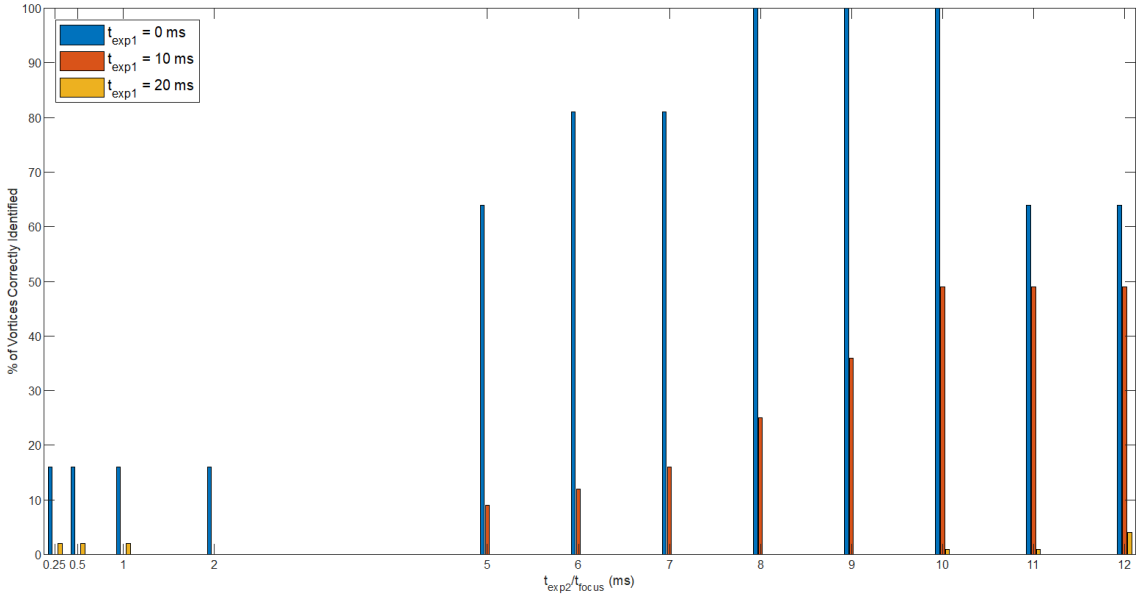

FIGURE 6.20. Percent of vortices in sample distribution correctly identified for each t_{exp_2} and t_{exp_1} considered. Simulations were carried out on a 1024x1024 grid of spatial extent 150 μm x 150 μm with fixed settings $t_{lat} = 500$ μs, $U_{lat} = 1\mu$, $\lambda_{lat} = 1$ μm, $\Gamma_1^{Threshold} = 0.5$, $\Gamma_2^{Threshold} = 0.35$.

To summarize our findings: using the AOSHWS we are able to measure velocity

fields that qualitatively match what we would expect for a known vortex distribution over a range of parameter settings. This range depends on the initial expansion time. Though the fields seem to faithfully represent the system dynamics, the range over which our vortex identification algorithm is successful is much narrower. This leads us to believe that the vortex identification algorithm we have chosen is largely at fault as it is not optimized for the specifics of quantum vortices. We were not able to find such an algorithm in the literature, however, as a proof-of-principle we deem it a success. Future work to improve the AOSHWS method should start with a study of how the focal properties of the lattice are effected by the initial expansion time as well as an investigation into optimization of the vortex identification algorithm for quantum vortices. The latter seems a natural application for machine learning techniques.

CHAPTER 7
Conclusions

We experimentally explored the behaviour of a BEC in an out-of-equilibrium state in a rotating TOP trap. This technique involved loading a BEC into a TOP trap rotating off-resonance from surface wave modes and perturbing the condensate with a 660 nm laser pulse. The condensate was then held in the rotating trap for a thermalization time on the order of 5 s before being imaged without expansion using an absorption modality. A variety of different vortex distributions were generated depending on the experimental conditions as the condensate sought a rotating, vortex lattice ground state. Through various experimental checks we verified that the vorticity was not being generated by fluid flow around a repulsive barrier. We also found no evidence of a resonance with respect to the trap rotational frequency introduced by the presence of a central barrier. However a strong upward trend in the number of generated vortices was evident as the peak irradiance of the perturbing pulse was increased. We hypothesize that this is because a more powerful perturbation adds more energy to the BEC and puts it into a broader superposition over energy states increasing the likelihood that we will find it in a many-vortex state. By imaging the cloud at various stages during the process we found that the initially uniform BEC distorted upon being perturbed. After several seconds of thermalization, vortices began to enter the condensate from the edges. We expect the data gathered will shed light on the relaxation dynamics of non-equilibrium BECs and interactions with the thermal fraction and aid development of stochastic GPE models. These models are essential to the understanding of finite temperature BEC physics as well as a broader class of problems in non-equilibrium physics.

We provided proof-of-principle simulations and analysis of two novel and related

methods to detect and characterize vorticity in a BEC using optical lattices. In the first method we allow the condensate to expand for an initial period and subsequently apply a 1D lattice to break up the condensate density into fringes with the same periodicity. In the presence of vortices, the opposing velocity vectors on opposite sides of the cores create dislocations in the fringes. By analyzing the orientation of the fringes at the dislocation we can determine the handedness. In doing so we can determine the Onsager point vortex Hamiltonian for simple, singly charged vortex distributions. We found that our ability to resolve the lattice fringes depended on the initial expansion time of the condensate. Further work may measure the displacement of the fringes at the dislocation to determine the magnitude of the vortex charge.

The process of the second method is identical except that the condensate is broken up with a 2D lattice. This acts as a measurement of the velocity spectrum in a manner directly analogous to a Shack-Hartmann Wavefront by using Raman-Nath scattering to imprint a sinusoidal phase curvature on the condensate. We refer to this method as the Atom-Optical Shack-Hartmann Wavefront Sensor. Once the velocity spectrum is measured we make use of an identification algorithm that determines the location and charge of vortex singularities. Though we have shown that the AOSHWS method is sound in principle, there are quite a number of variables for optimization. The ability to resolve vortices depends strongly on the periodicity of the lattice which corresponds directly to the spatial frequency at which we sample the velocity field. When we use a quadratic approximation to the focal time after the lattice pulse the range of sampling frequencies which yield 100 percent success increases with initial expansion time. Longer initial expansion times present experimental difficulty for the AOSHWS since releasing BECs from traps commonly yields random momentum kicks. Since this effectively creates a random shift in the lattice location, longer initial expansion times have the potential to introduce error into peak displacement measurements. As such, it is experimentally favorable to use zero initial expansion time. We found that at smaller initial expansion times the optimal focal time deviated significantly from

the quadratic approximation. This is likely due to a stronger contribution from the non-linearity in the denser, non-expanded cloud. Investigations into the relationship between the initial expansion time and the optimal focal time for a given lattice will be essential for future development of this method. As we are able to measure faithful velocity fields over a broad range of lattice periods we believe our system is currently limited by the vortex detection algorithm. Thus we expect great improvements will be made through detailed optimization of the lattice parameters as well as the machine vision problem of quantum vortex detection.

The work presented in the dissertation provides the first proof-of-principle stages following the introduction of this method. The simple set of variables that define the measurement show a rich interplay of trade-offs which require careful analysis. In this dissertation we have focused on its use for vortex detection but the AOSHWS has broad applications. Once the measurement is properly characterized we believe it to be an experimental method capable of determining the kinetic energy spectrum of a BEC directly from the measured velocity field. Since both vortex identification and a velocity field measurement give us access to the kinetic energy spectrum the AOSHWS might allow us to compare results to test the accuracy and validity of the Onsager point vortex model. In addition, the AOSHWS provides varying degrees of angular and position information simultaneously depending on the lattice period. This capability makes it of use to studies of quantum coherence in matter waves. Finally we note that the method does not depend on the properties of any specific atomic species and is therefore fully adaptable to any atomic gas BEC laboratory. Though there is still much work to be done to optimize the method we believe the Atom-Optical Shack-Hartmann Wavefront Sensor will prove to be a valuable tool for BEC physics.

References

[1] S. N. Bose. Plancks Gesetz und Lichtquantenhypothese. *Zetischrift fur Physik*, 26:178–181, 1924.

[2] A. Einstein. Quantum Theory of the Monatomic Ideal Gas. *Sitzungberichte der Preussischen Akademie der Wissenschaften, Pysikalisch-mathematische Klasse*, pages 261–267, 1925.

[3] M. H. Anderson, J. R. Ensher, M. R. Matthews, C. E. Wieman, and E. A. Cornell. Observation of Bose-Einstein Condensation in a Dilute Atomic Vapor. *Science*, 269(5221):198–201, 1995.

[4] J. F. Allen and A. D. Misener. Flow of Liquid Helium II. *Nature*, 141(3558):75–75, Jan 1938.

[5] P. Kapitza. Viscosity of liquid helium below the λ-point. *Nature*, 141(3558):74–74, Jan 1938.

[6] L. Onsager. Statistical hydrodynamics. *Il Nuovo Cimento*, 6, Supplement 2:279, Mar 1949.

[7] T. W. Neely, E. C. Samson, A. S. Bradley, M. J. Davis, and B. P. Anderson. Observation of vortex dipoles in an oblate Bose-Einstein condensate. *Phys. Rev. Lett.*, 104(16):160401, Apr 2010.

[8] Tyler W. Neely. *Formation, Dynamics and Decay of Quantized Vortices in Bose-Einstein Condensates: Elements of Quantum Turbulence*. PhD thesis, University of Arizona, 2010.

[9] K. E. Wilson, Z. L. Newman, J. D. Lowney, and B. P. Anderson. *In Situ* Imaging of Vortices in Bose-Einstein Condensates. *Phys. Rev. A*, 91:023621, 2015.

[10] Kali Wilson. *Developing a Toolkit for Experimental Studies of Two-Dimensional Quantum Turbulence in Bose-Einstein Condensates*. PhD thesis, University of Arizona, 2015.

[11] E. Hodby, G. Hechenblaikner, S. A. Hopkins, O. M. Maragò, and C. J. Foot. Vortex nucleation in Bose-Einstein condensates in an oblate, purely magnetic potential. *Phys. Rev. Lett.*, 88(1):010405, Dec 2001.

[12] Guillaume Gauthier, Matthew T. Reeves, Xiaoquan Yu, Ashton S. Bradley, Mark A. Baker, Thomas A. Bell, Halina Rubinsztein-Dunlop, Matthew J. Davis, and Tyler W. Neely. Giant vortex clusters in a two-dimensional quantum fluid. *Science*, 364(6447):1264–1267, 2019.

[13] David R. Scherer. *Vortex Formation by Merging and Interference of Multiple Trapped Bose-Einstein Condensates*. PhD thesis, University of Arizona, 2007.

[14] J. R. Abo-Shareer, C. Raman, J. M. Vogels, and W. Ketterle. Observation of vortex lattices in Bose-Einstein condensates. *Science*, 292(5516):476, Apr 2001.

[15] A. E. Leanhardt, A. Görlitz, A. P. Chikkatur, D. Kielpinski, Y. Shin, D. E. Pritchard, and W. Ketterle. Imprinting vortices in a Bose-Einstein condensate using topological phases. *Phys. Rev. Lett.*, 89(19):190403, Oct 2002.

[16] M. R. Matthews, B. P. Anderson, P. C. Haljan, D. S. Hall, C. E. Wieman, and E. A. Cornell. Vortices in a Bose-Einstein condensate. *Phys. Rev. Lett.*, 83(13):2498, Sep 1999.

[17] J. E. Williams and M. J. Holland. Preparing topological states of a Bose–Einstein condensate. *Nature*, 401(6753):568–572, Oct 1999.

[18] R. A. Williams, S. Al-Assam, and C. J. Foot. Observation of vortex nucleation in a rotating two-dimensional lattice of Bose-Einstein condensates. *Phys. Rev. Lett.*, 104(5):050404, Feb 2010.

[19] S. W. Seo, B. Ko, J. H. Kim, and Y. Shin. Observation of vortex-antivortex pairing in decaying 2d turbulence of a superfluid gas. *Scientific Reports*, 7(1):4587, Jul 2017.

[20] S. Donadello, S. Serafini, M. Tylutki, L. P. Pitaevskii, F. Dalfovo, G. Lamporesi, and G. Ferrari. Observation of solitonic vortices in Bose-Einstein condensates. *Phys. Rev. Lett.*, 113:065302, Aug 2014.

[21] F. Chevy, K. W. Madison, V. Bretin, and J. Dalibard. Interferometric detection of a single vortex in a dilute Bose-Einstein condensate. *Phys. Rev. A*, 64(3):031601, Aug 2001.

[22] S. Inouye, S. Gupta, T. Rosenband, A. P. Chikkatur, A. Görlitz, T. L. Gustavson, A. E. Leanhardt, D. E. Pritchard, and W. Ketterle. Observation of vortex phase singularities in Bose-Einstein condensates. *Phys. Rev. Lett.*, 87(8):080402, Aug 2001.

[23] A. S. Bradley and B. P. Anderson. Energy Spectra of Vortex Distributions in Two-Dimensional Quantum Turbulence. *Phys. Rev. X*, 2(4):041001, 2012.

[24] C. Pethick and H. Smith. *Bose-Einstein Condensation in Dilute Gases*. Cambridge University Press, Cambridge, 2nd edn., 2008.

[25] R. G. Lane and M. Tallon. Wave-front reconstruction using a Shack-Hartmann sensor. *Appl. Opt.*, 31(32):6902–6908, Nov 1992.

[26] W.H. Southwell. Wave-front estimation from wave-front slope measurements. *J. Opt. Soc. Am.*, 70(8):998–1006, Aug 1980.

[27] Zachary Newman. *A New Apparatus for Studies of Quantized Vortex Dynamics in Dilute-Gas Bose-Einstein Condensates*. PhD thesis, University of Arizona, 2015.

[28] M. Inguscio, S. Stringari, and C. Wieman. *Bose-Einstein Condensation in Atomic Gases*. International School of Physics "Enrico Fermi". IOS Press, 1999.

[29] A. Einstein. Quantum Theory of the Monatomic Ideal Gas, Part II. *Sitzungberichte der Preussischen Akademie der Wissenschaften, Pysikalisch-mathematische Klasse*, pages 3–14, 1925.

[30] A. Minguzzi, S. Succi, F. Toschi, M. P. Tosi, and P. Vignolo. Numerical methods for atomic quantum gases with applications to Bose-Einstein condensates and to ultracold fermions. *Physics Reports*, 395(4-5):223–355, June 2004.

[31] G. K. Batchelor. *An Introduction to Fluid Dynamics*. Cambridge Mathematical Library. Cambridge University Press, 2000.

[32] A.N. Kolmogorov. The local structure of turbulence in incompressible viscous fluid for very large Reynolds numbers. *Cr Acad. Sci. URSS*, 30:301–305, 1941.

[33] A.N. Kolmogorov. The local structure of isotropic turbulence in an incompressible viscous fluid. *Dokl. Akad. Nauk SSSR*, 30:301–305, 1941.

[34] Lewis Fry Richardson and Peter Lynch. *Weather Prediction by Numerical Process*. Cambridge Mathematical Library. Cambridge University Press, 2 edition, 2007.

[35] Robert H. Kraichnan. Inertial Ranges in Two-Dimensional Turbulence. *Physics of Fluids*, 10(7):1417–1423, Jul 1967.

[36] Gregory L. Eyink and Katepalli R. Sreenivasan. Onsager and the theory of hydrodynamic turbulence. *Rev. Mod. Phys.*, 78:87–135, Jan 2006.

[37] Carlo F. Barenghi, Ladislav Skrbek, and Katepalli R. Sreenivasan. Introduction to quantum turbulence. *Proceedings of the National Academy of Sciences*, 111(Supplement 1):4647–4652, 2014.

[38] T. W. Neely, A. S. Bradley, E. C. Samson, S. J. Rooney, E. M. Wright, K. J. H. Law, R. Carretero-González, P. G. Kevrekidis, M. J. Davis, and B. P. Anderson. Characteristics of two-dimensional quantum turbulence in a compressible superfluid. *Phys. Rev. Lett.*, 111:235301, Dec 2013.

[39] Shaun P. Johnstone, Andrew J. Groszek, Philip T. Starkey, Christopher J. Billington, Tapio P. Simula, and Kristian Helmerson. Evolution of large-scale flow from turbulence in a two-dimensional superfluid. *Science*, 364(6447):1267–1271, 2019.

[40] V.K. Tkachenko. On vortex lattices. *J. Exptl. Theoret. Phys. (U.S.S.R.)*, 22(6):1875–1883, June 1966.

[41] K. W. Madison, F. Chevy, W. Wohlleben, and J. Dalibard. Vortex formation in a stirred Bose-Einstein condensate. *Phys. Rev. Lett.*, 84:806–809, Jan 2000.

[42] Wolfgang Petrich, Michael H. Anderson, Jason R. Ensher, and Eric A. Cornell. Stable, tightly confining magnetic trap for evaporative cooling of neutral atoms. *Phys. Rev. Lett.*, 74:3352–3355, Apr 1995.

[43] Jason Remington Ensher. *The First Experiments with Bose-Einstein Condensation of* ^{87}*Rb*. PhD thesis, University of Colorado at Boulder, 1998.

[44] R.V. Shack. Production and use of a lenticular Hartmann screen. *J. Opt. Soc. Am.*, 61(5):648–697, May 1971.

[45] Platt B.C. Shack, R.V. History and principles of Shack-Hartmann wavefront sensing. *J. Refract. Surg.*, Sept-Oct 2001.

[46] J.E. Greivenkamp. *Field Guide to Geometrical Optics*. SPIE Field Guides. SPIE Press, 2004.

[47] R. K. Tyson. *Principles of Adaptive Optics*. Series in Optics and Optoelectronics. Taylor and Francis, third edition, 2011.

[48] Jérôme Primot. Theoretical description of Shack–Hartmann wave-front sensor. *Optics Communications*, 222(1):81 – 92, 2003.

[49] Kevin Murphy and Chris Dainty. Comparison of optical vortex detection methods for use with a Shack-Hartmann wavefront sensor. *Opt. Express*, 20(5):4988–5002, Feb 2012.

[50] Eric-Olivier Le Bigot and Walter J. Wild. Theory of branch-point detection and its implementation. *J. Opt. Soc. Am. A*, 16(7):1724–1729, Jul 1999.

[51] Walter J. Wild and Eric O. Le Bigot. Rapid and robust detection of branch points from wave-front gradients. *Opt. Lett.*, 24(4):190–192, Feb 1999.

[52] J. E. Bjorkholm, R. R. Freeman, A. Ashkin, and D. B. Pearson. Observation of focusing of neutral atoms by the dipole forces of resonance-radiation pressure. *Phys. Rev. Lett.*, 41:1361–1364, Nov 1978.

[53] J. E. Bjorkholm, R. R. Freeman, A. Ashkin, and D. B. Pearson. Experimental observation of the influence of the quantum fluctuations of resonance-radiation pressure. *Opt. Lett.*, 5(3):111–113, Mar 1980.

[54] V.I. Balykin and V.S. Letokhov. Deep focusing of an atomic beam in the angstrom region by laser radiation. *Zh. Eksp. Teor. Fiz.*, 94:140–150, Jan 1988.

[55] Gregg M. Gallatin and Phillip L. Gould. Laser focusing of atomic beams. *J. Opt. Soc. Am. B*, 8(3):502–508, Mar 1991.

[56] T. Sleator, T. Pfau, V. Balykin, and J. Mlynek. Imaging and focusing of an atomic beam with a large period standing light wave. *Applied Physics B*, 54:375–379, May 1992.

[57] G. Timp, R. E. Behringer, D. M. Tennant, J. E. Cunningham, M. Prentiss, and K. K. Berggren. Using light as a lens for submicron, neutral-atom lithography. *Phys. Rev. Lett.*, 69:1636–1639, Sep 1992.

[58] J. J. McClelland, R. E. Scholten, E. C. Palm, and R. J. Celotta. Laser-focused atomic deposition. *Science*, 262(5135):877–880, 1993.

[59] J. J. McClelland. Atom-optical properties of a standing-wave light field. *J. Opt. Soc. Am. B*, 12(10):1761–1768, Oct 1995.

[60] J. L. Cohen, B. Dubetsky, and P. R. Berman. Atom focusing by far-detuned and resonant standing wave fields: Thin-lens regime. *Phys. Rev. A*, 60:4886–4901, Dec 1999.

[61] Laurent Graftieaux, Marc Michard, and Nathalie Grosjean. Combining PIV, POD and vortex identification algorithms for the study of unsteady turbulent swirling flows. *Measurement Science and Technology*, 12(9):1422–1429, aug 2001.

[62] Sebastian Endrikat. *Find vortices in velocity fields.* MATLAB Central File Exchange, 1.3.0.0 edition, 2020.

[63] E.M. Wright. *Lecture Notes in Quantum Matter Waves.* OPTI 550, The University of Arizona, 2015.